

**Development and Demonstration of A Hybrid 100 kW  
Passive-Controller**

**Wind Turbine Smart Rotor Toward Mega-Watt Turbines**

**Revision 1**

**Design Optimization study of the 100 kW Rotor**

Taeseong Kim, Frederik Zahle, Michael McWilliam, David Verelst,  
Antariksh Dicholkar, Peter Bearing

November 21, 2017

## Contents

<b>1 Conceptual Design of the 100 kW Blade using HawtOpt2</b>	<b>3</b>
1.1 Introduction . . . . .	3
1.2 Aerostructural Design Tool . . . . .	3
1.3 Blade Parametrization . . . . .	3
1.4 Baseline Design . . . . .	4
1.4.1 Airfoil series . . . . .	5
1.4.2 Reference Materials . . . . .	8
1.4.3 Structural Layout . . . . .	9
1.5 Design Studies . . . . .	11
1.5.1 Design Assumptions . . . . .	11
1.5.2 Overview of the designs . . . . .	13
1.5.3 Structural Design . . . . .	24
1.6 Selected blade design - KB5 swept blade . . . . .	25
1.6.1 Multidisciplinary optimization . . . . .	26
1.6.2 Planform . . . . .	26
1.6.3 Structure . . . . .	28
1.6.4 Steady-state performance . . . . .	35
1.7 Conclusion . . . . .	45
<b>2 Static analysis</b>	<b>46</b>
2.1 Load test . . . . .	46
2.2 Eigen analysis . . . . .	46
<b>3 Analysis of the Design Load Basis</b>	<b>47</b>
3.1 Introduction . . . . .	47
3.2 Stiff Tower . . . . .	48
3.3 Controller Tuning . . . . .	48
3.4 Discussion and Conclusion . . . . .	48
3.5 Future Work . . . . .	48
<b>4 Design Load Basis Statistic Tables</b>	<b>49</b>
4.1 Reference vs KB5 . . . . .	49
<b>5 Design Load Basis Statistic Plots</b>	<b>52</b>
5.1 Reference vs KB5 . . . . .	52
5.1.1 No turbulence with wind step . . . . .	52
5.1.2 DLC12 . . . . .	59
5.1.3 DLC24 . . . . .	65
5.1.4 DLC31 . . . . .	71
5.1.5 DLC41 . . . . .	77
5.1.6 DLC64 . . . . .	83

# 1 Conceptual Design of the 100 kW Blade using HawtOpt2

## 1.1 Introduction

A baseline blade is re-constituted from the data supplied for the 100 kW turbine by making certain assumptions for the missing data. The baseline blade is then optimized according to the multidisciplinary optimization framework defined by the HawtOpt2 tool. The aim is to obtain a final blade design that is maximized for the annual energy production and includes bend-twist coupling techniques for passive load alleviation. Three initial optimized designs are obtained including a non-coupled straight blade, a materially coupled blade and a geometrically coupled backward swept blade. These designs are meant to establish the potential of the different aeroelastic tailoring techniques in load reduction and in improvement of the annual energy production. Based on their performances the best aeroelastic tailoring technique is selected. The baseline blade is then optimized by applying the chosen bend-twist coupling technique and taking into account manufacturing concerns in the design.

## 1.2 Aerostructural Design Tool

HawtOpt2 uses OpenMDAO v1.x [?] to handle the definition of the optimization problem, workflow, dataflow and parallelization of simulation cases. This allows us to efficiently make use of high performance computing clusters, with MPI parallelization of both cases within the objective function (e.g. design load cases), as well as the evaluation of finite difference gradients. OpenMDAO provides an interface to PyOptSparse [?] which has wrappers for several optimization algorithms. In this work, the open source gradient-based interior point optimizer IPOPT [?] is used. HawtOpt2 has interfaces to the finite element cross sectional tool BECAS [? ?] and to the aeroelastic tools HAWC2 [?] and HAWCStab2 [?]. BECAS allows for the evaluation of the cross sectional structural and mass properties of the blade, as well as calculation of material failure both with respect to ultimate and fatigue loads. HAWCStab2 uses an unsteady blade element momentum (BEM) model of the rotor and a geometrically non-linear finite beam element model to compute steady-state aerodynamic states, structural deflections and linearized models of the wind turbine. HAWCStab2 has an analytical linearization of the high-order aeroservoelastic model, which can be used for frequency analysis, controller tuning and evaluation of fatigue damage equivalent load rates using a frequency domain based approach [?]. Ultimate loads simulations within the optimization loop are carried out using the aero-hydro-servo-elastic software package HAWC2 on a reduced set of design load cases as per IEC 61400-1 Ed3, while the final designs are evaluated using the full design load basis described in ref. [?].

Figure 1.1 shows a so-called extended design structure matrix diagram (XDSM) [?] of the workflow in HawtOpt2. Overlaid boxes indicate components that are executed in parallel for each cross-section/load case. At the upper level, the entire workflow is parallelized to enable parallel gradient evaluation. All of these parallelizations are embarrassingly parallel and thus this scales linearly with the number of CPUs available. A typical optimization will use 20 cores per objective function evaluation, and be parallelized according to the available resource with  $n$  number of concurrent FD gradient evaluations. For the present study 30 concurrent FD evaluations were used. A single objective evaluation required approximately 4 minutes, and therefore approximately 12 minutes per major iteration for 60 design variables, using a total of 600 cores.<sup>1</sup>

## 1.3 Blade Parametrization

The blade planform is described in terms of distributions of chord, twist, relative thickness and pitch axis aft leading edge, the latter being the distance between the leading edge and the blade axis. The

<sup>1</sup>Parts of the text above describing the tools used and the overall optimization framework are excerpts from Zahle et al [?]. Refer to this article for a full description of the tools and most recent results.

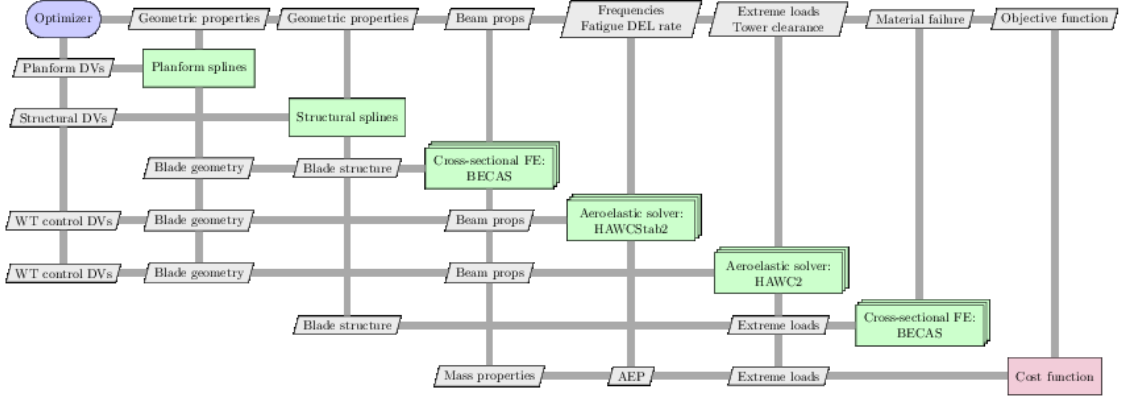


Figure 1.1: Extended Design Structure Matrix diagram of the workflow of HawtOpt2.

lofted shape of the blade is generated based on interpolation of a family of airfoils with different relative thicknesses.

The internal structure is defined from a number of regions that each cover a fraction of the cross-sections along the blade. Each region consists of a number of materials that are placed according to a certain stacking sequence. Figure 1.2 shows a cross section in which the region division points (DPs) are indicated along with the parameterized quantities used to construct the structural geometry. The composite layup is described by a series of smooth splines describing the thicknesses of individual layers. For more details on the parametrization see [? ].

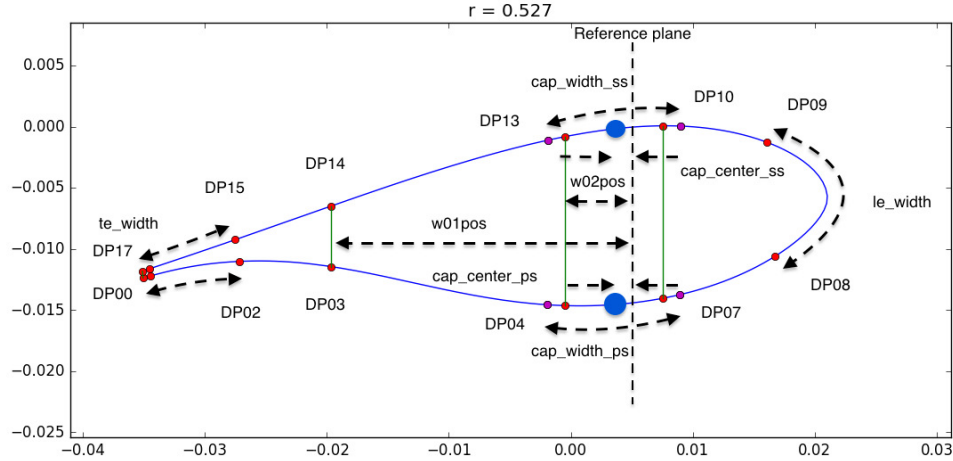


Figure 1.2: Region division points (DP) definition: red points indicate division points between regions; their positions are defined as curve fraction from pressure side TE ( $s=-1$ ) to LE ( $s=0$ ) to suction side TE ( $s=1$ ).

## 1.4 Baseline Design

The initial data supplied to the project regarding the 100 kW blade consisted of stiffness data as well as blade planform, and overall operational characteristics, and component masses. Data on the airfoils used

on the blades or their performance were not supplied. Neither were details on the internal structure and the materials used.

Several choices had to be made during the initial phases. In the bullet list below the main choices are listed:

- Airfoils: The main airfoil series used is the FFA-W3 series along with a NACA-63-418 tip airfoil.
- Airfoil data: Airfoil data was computed using the 2D incompressible CFD solver EllipSys2D [? ? ?], as a 70/30 blend of clean and tripped flow conditions computed at  $Re = 1 \times 10^6$ .
- Materials: The blade consists of glass fibre only. Materials used are the same as on the DTU 10MW RWT [? ].
- Structural layout: Conventional box structure with linearly tapered main laminates connected with two shear webs.
- Blade planform: Based on the externally supplied planform.

The following sub-sections describe the steps taken to design the fully described aerostructural blade design for the 100 kW rotor.

#### 1.4.1 Airfoil series

The main airfoil series used is the FFA-W3 series along with a NACA-63-418 tip airfoil. Figure 1.3 shows the 2D cross-sectional shapes of these airfoils. Figures 1.4 to 1.6 show the lift, drag and lift-to-drag polars of the airfoils computed at a Reynolds number of  $Re = 1 \times 10^6$  using EllipSys2D with a mesh consisting of 512 cells in the chordwise direction and 192 cells in the normal direction. To account for effects of roughness, the polars used were generated from a blend of clean surface, free transition flow and fully turbulent flow, with a blend factor of 0.7/0.3. 360 degree extrapolation of the airfoil data was done using the Viterna method.<sup>2</sup> No 3D correction of the airfoil data was done since the position of the airfoils are changed during optimization, making the 3D correction invalid since it depends on the spanwise position.

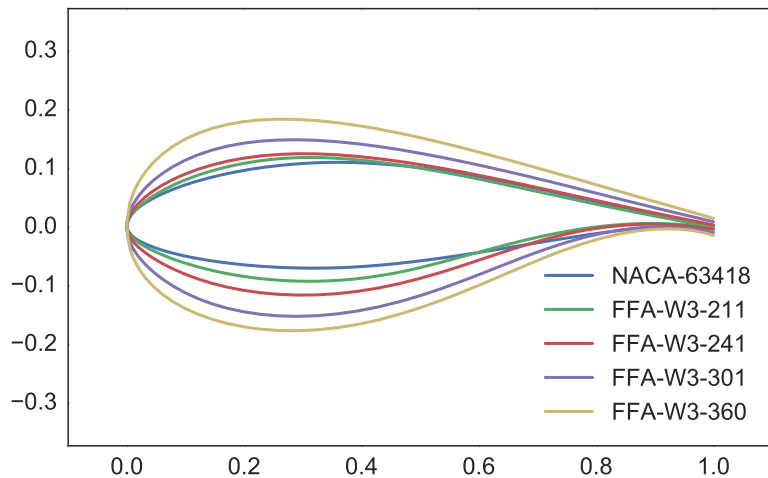


Figure 1.3: Airfoils used on the 100kW baseline blade.

---

<sup>2</sup><http://wisdem.github.io/AirfoilPreppy/>

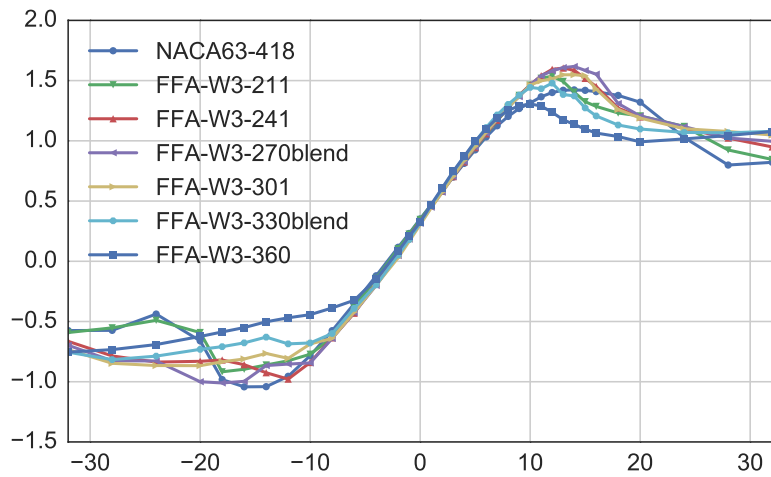


Figure 1.4: Airfoil lift coefficients as function of AOA computed at  $Re = 1e6$ .

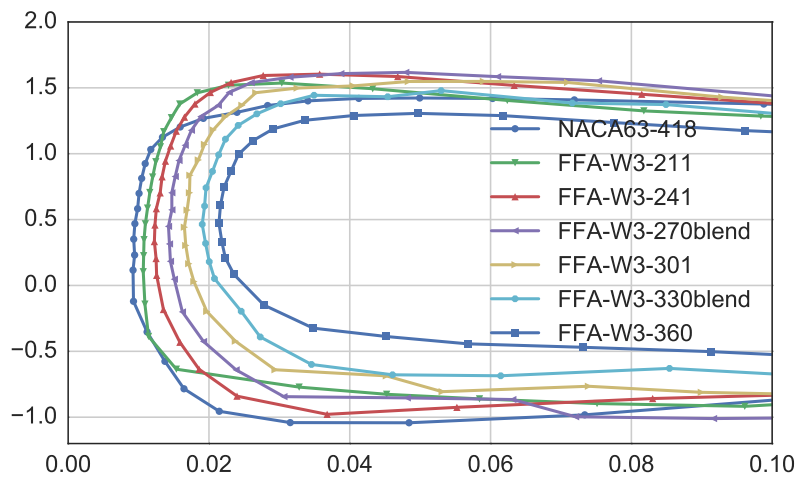


Figure 1.5: Airfoil drag coefficients as function of AOA computed at  $Re = 1e6$ .

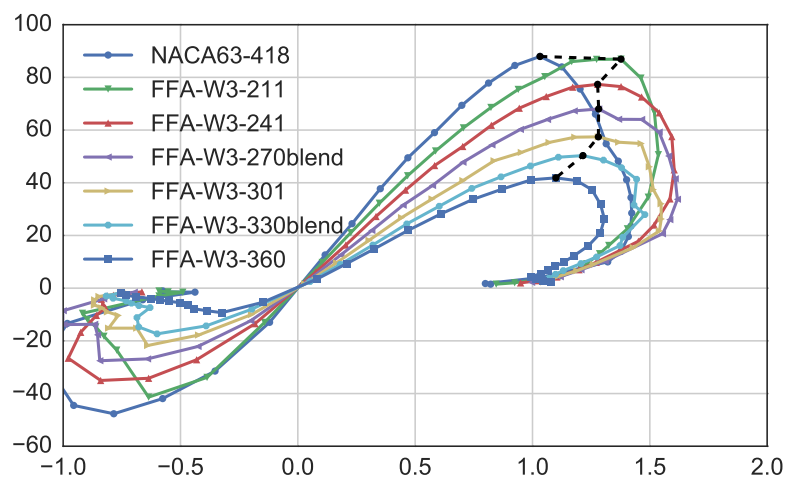


Figure 1.6: Airfoil lift to drag ratio as function of  $C_l$  computed at  $Re = 1e6$ .

### 1.4.2 Reference Materials

The material properties used for the blade were those defined for the DTU 10 MW RWT (for more details, see [? ]). Table 1.1 lists the apparent mechanical properties of the multidirectional plies used.

Table 1.1: Fiber orientation and apparent mechanical properties of the multidirectional plies.

Multidirectional Ply	Uniax	Biax	Triax	
Fiber volume fraction $V_f$	0.55	0.5	0.5	-
Unidirectional lamina	Lamina 2	Lamina 1	Lamina 1	
0° fibers	95	0	30	%
90° fibers	5	0	0	%
+45° fibers	0	50	35	%
-45° fibers	0	50	35	%
Young's modulus $E_1$	41.63	13.92	21.79	GPa
Young's modulus $E_2$	14.93	13.92	14.67	GPa
Shear modulus $G_{12}$	5.047	11.50	9.413	GPa
Poisson's ratio $\nu_{12}$	0.241	0.533	0.478	-
Shear modulus $G_{13} = G_{23}^{(a)}$	5.04698	4.53864	4.53864	GPa
Mass density $\rho$	1915.5	1845.0	1845.0	$kg/m^3$

Design strength properties are also defined for these materials<sup>3</sup> and are listed in Table 1.2 and Table 1.3.

Table 1.2: Design strength properties of the multidirectional plies.

	$\sigma_{11}^t$	$\sigma_{22}^t$	$\sigma_{33}^t$	$\sigma_{11}^c$	$\sigma_{22}^c$	$\sigma_{33}^c$	$\tau_{12}$	$\tau_{13}$	$\tau_{23}$
Biax	69.3	69.3	69.3	64.9	64.9	64.9	55.9	55.9	55.9
Uniax	360.0	24.8	24.8	257.0	63.5	63.5	16.6	16.6	16.6
Balsa	1.0	1.0	1.0	1.0	1.0	1.0	1.0	1.0	1.0
Triax	186.0	30.5	30.5	152.0	51.5	51.5	42.3	42.3	42.3

Table 1.3: Design strength properties of the multidirectional plies.

	$\epsilon_{11}^t$	$\epsilon_{22}^t$	$\epsilon_{33}^t$	$\epsilon_{11}^c$	$\epsilon_{22}^c$	$\epsilon_{33}^t$	$\gamma_{12}$	$\gamma_{13}$	$\gamma_{23}$
Biax	6.802e-3	1.0e6	1.0e6	7.255e-3	1.0e6	1.0e6	1.0e11	1.0e+11	1.0e+11
Uniax	6.802e-3	1.0e6	1.0e6	9.523e-3	1.0e6	1.0e6	1.0e11	1.0e+11	1.0e+11
Balsa	1.000e+6	1.0e6	1.0e6	1.000e+6	1.0e6	1.0e6	1.0e11	1.0e+11	1.0e+11
Triax	8.162e-3	1.0e6	1.0e6	9.976e-3	1.0e6	1.0e6	1.0e11	1.0e+11	1.0e+11

<sup>3</sup>Internal communication, provided by Peter Berring

### 1.4.3 Structural Layout

An approximate sizing of the internal structure was carried out in order to match the stiffness properties supplied from the external partners. This was done using the BECAS interface in HawtOpt2, where material thickness distributions in 19 cross-sections along the span were sized to match flapwise stiffness,  $EI_x$ , edgewise stiffness,  $EI_y$ , and torsional stiffness,  $GJ$ . Following this optimization, the material thicknesses were adjusted manually to obtain a reasonably smooth material distribution along the blade.

Table 1.4 shows the overall properties of the structural geometry. The spar cap was tapered from a width of 0.2 m at the root to 0.1 m at the tip, and the trailing edge and leading edge reinforcements had a width of 0.08 and 0.12 m, respectively. The structural geometry for the blade is plotted in Figure 1.7.

Table 1.4: Overall properties of internal structure.

Spar cap widths	Linear taper 0.2 m (root) to 0.1 m (tip)
Trailing edge panel width upper	0.08 m
Trailing edge panel width lower	0.08 m
Leading edge panel width (upper+lower)	0.12 m
Shear web angle relative to rotor plane	90 deg

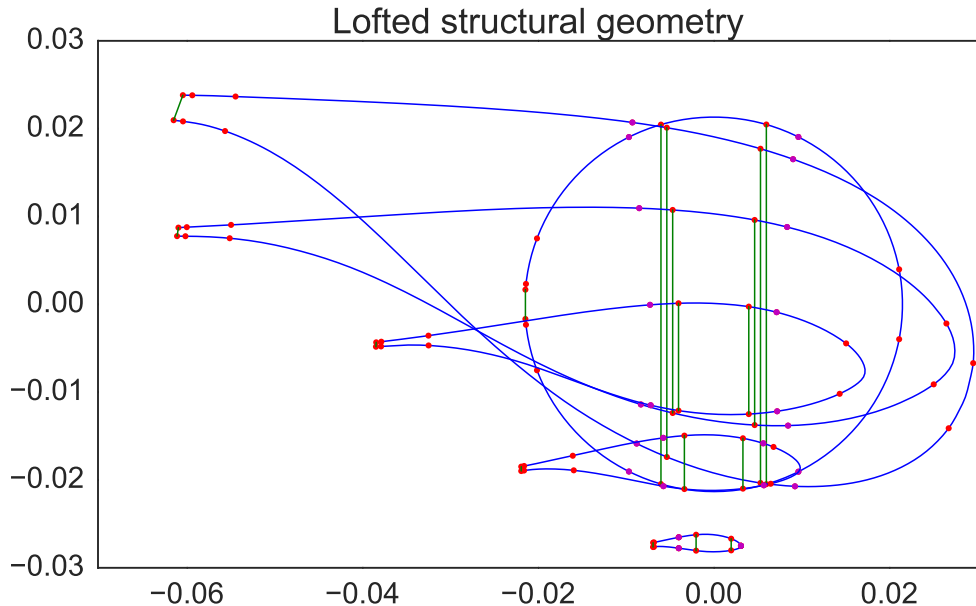


Figure 1.7: Lofted blade showing internal structural geometry.

Figure 1.8 shows a 3D plot of the lofted blade structure with material distributions. The total mass of the blade resulting from the sizing process was approximately 230 kg. This does not include adhesives, surface finishing, and a complete root design.

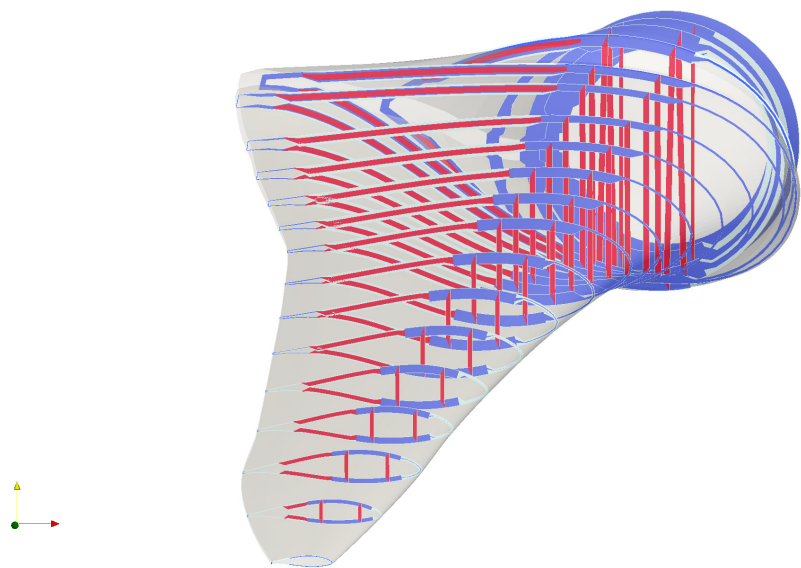


Figure 1.8: Lofted blade showing internal structural geometry.

## 1.5 Design Studies

In this section five design studies are presented:

- **KB1:** Optimized straight blade. This blade is optimized with constraints on blade torsion to be less than 1 degree at the tip, and no design freedom is given to introduce sweep or material couplings.
- **KB2:** Optimized swept blade. This blade is optimized without constraints on blade torsion and given design freedom to introduce sweep, but not material couplings.
- **KB3:** Optimized material coupled blade. This blade is optimized without constraints on blade torsion and given design freedom to introduce material couplings in the spar cap, but not sweep.
- **KB4:** Optimized swept blade with fixed rotor speed schedule. This blade is optimized without constraints on blade torsion and given design freedom to introduce sweep, but not material couplings. Compared to KB2, additional constraints have been placed on the sweep and prebend. The sweep is constrained to achieve only backward sweep with a maximum limit on its value not exceeding 5% of the reference blade length. The sweep is only allowed from 60% blade span and onwards. The prebend too has been constrained to only bend away from the tower with a maximum limit on its value not exceeding 10% of the reference blade length. An outer layer of triax is added, which is maintained at a fixed thickness through the optimization. The spar cap width is disallowed design freedom. These design decisions have been taken to address manufacturing and structural concerns. Importantly, this design has a fixed rotor speed schedule calculated based on the design tip-speed ratio of the reference blade.
- **KB5:** Optimized swept blade. This blade is optimized without constraints on blade torsion and given design freedom to introduce sweep, but not material couplings. It incorporates the same design decisions as applied to KB4. However, unlike KB4 the rotor speed schedule is allowed design freedom to vary through the optimization.

All five designs are made with identical optimization problem definitions, that is, same objective and constraints, as well as identical design variables, except for the above mentioned differences. The problem definition is summarized below.

The cost function is defined as

$$f(\{\mathbf{x}_p, \mathbf{x}_s, \mathbf{x}_{oper}\}, \mathbf{p}) = -\frac{AEP(\{\mathbf{x}_p, \mathbf{x}_s, \mathbf{x}_{oper}\}, \mathbf{p})}{AEP(\{\mathbf{0}, \mathbf{0}, \mathbf{0}\}, \mathbf{p})} \quad (1.1)$$

$AEP$  is the annual energy production and  $AEP(\{\mathbf{0}, \mathbf{0}, \mathbf{0}\}, \mathbf{p})$  is the annual energy production of the baseline design. Three different types of constraints are defined depending on the variables they depend on. Constraints  $\mathbf{g}$  depend only on planform parameters. They include bounds on the chord and relative thickness. Constraints  $\mathbf{h}_g$  depends only on structural parameters. These constraints include bounds on the material thicknesses and on the position and widths of the spar caps. Constraints  $\mathbf{h}_s$  denote the limits on the maximum allowable stresses in the structure. The constraints  $\mathbf{k}$  depend on both the planform and structural variables, such as blade tip deflection and loads.

Tables 1.5 and 1.6 provides a summary of design variables and constraints used in this study.

### 1.5.1 Design Assumptions

This section is here so the user understands the risks in using these designs. The section warns the user, outlines the missing information, the assumptions and the potential risk.

It is important that the user of this design understand that insufficient information was given to complete a proper and complete design. The missing information was identified and presented to the project partners. To overcome this problem, the consortium agreed that we should make all the necessary assumptions to carry out the design. Accordingly we have made several assumptions to complete this task. These assumptions were made with the best judgement based on experience and the information that had been provided to us. However, these assumptions are a major source of error and represent a risk to using this design.

The user should be aware that there are risks to using these designs. We carried out the design with the understanding that these designs would be used under the following conditions:

Table 1.5: Free form deformation spline (FFD) design variables used in the optimizations.

Parameter	# of DVs	Comment
Chord	6	-
Twist	5	Root twist fixed
Relative thickness	4	Root and tip relative thickness fixed
Out of plane prebend	3	-
In-plane sweep	4	Active for KB2, KB4 and KB5 design
Pitch axis aft LE	4	-
Blade length	1	-
Tip-speed ratio	1	Inactive in KB4 to ensure fixed RPM schedule.
Trailing edge uniax	4	Symmetric pressure/suction side
Spar cap uniax	4	Symmetric pressure/suction side
Leading edge uniax	4	Symmetric pressure/suction side
Leading panels triax	4	Symmetric pressure/suction side
Trailing panels triax	4	Symmetric pressure/suction side
Spar cap width	2	Linearly tapered spar cap. Inactive in KB4 and KB5.
Suction side spar cap fibre angle	4	Only active for KB3 design
Pressure side spar cap fibre angle	4	Only active for KB3 design
<b>KB1 Total</b>	44	
<b>KB2 Total</b>	48	
<b>KB3 Total</b>	52	
<b>KB4 Total</b>	48	
<b>KB5 Total</b>	49	

Table 1.6: Non-linear constraints used in the design process.

Constraint	Value	Comment
max(chord)	< 0.9 m	Maximum chord limited for transport.
max(prebend)	< 0.9 m (for KB1,KB2, KB3)	Maximum prebend limited for transport.
max(sweep)	< 1 m (for KB4 and KB5) < 0.9 m (for KB2)	Maximum sweep limited for ease in manufacturing.
	< 0.5 m (for KB4 and KB5)	
min(relative thickness)	> 0.18	Fixed airfoil series.
min(material thickness)	> 0.0 m	Allow maximum freedom to reduce thickness - although unrealistic.
max(Blade deflection)	< 1.0 m	Allow blade tip to deflect 1 m.
Blade root flapwise moments (MxBR_steady)	< ref value	Steady state loads cannot exceed starting point.
Rotor thrust (T_steady)	< ref value	Steady state loads cannot exceed starting point.
Blade root flapwise moments (MxBR)	< ref value	Reduced DLB loads cannot exceed starting point.
Blade root edgewise moments (MyBR)	< ref value	Reduced DLB loads cannot exceed starting point.
Blade root pitch moments (MzBR)	< ref value	Reduced DLB loads cannot exceed starting point.
Tower top thrust (FyTT)	< ref value	Reduced DLB loads cannot exceed starting point.
Tower bottom fore-aft moment (MxTB)	< ref value	Reduced DLB loads cannot exceed starting point.
Rotor torque	< ref value	Ensure that the rotational speed is high enough below rated to not exceed generator maximum torque.
Blade mass	< 1.01 * ref value	Limit increase in blade mass to maintain equivalent production costs.
Blade mass moment	< 1.01 * ref value	Limit increase in blade mass moment to minimise edgewise fatigue.
Lift coefficient @ $r/R = [0.5 - 1.]$	< 1.4-1.1	Limit operational lift coefficient to avoid stall for turbulent inflow conditions.

1. The users understand that insufficient information was given and that actual performance and loads may not reflect the performance and loads predicted here.
2. The user will take the necessary precautions to avoid serious problems.
3. The rotors as they are designed here will only be operated in a supervised setting without posing any risk of damages to people or property if a failure occurs.
4. The rotors as they are designed here will only be used for research purposes
5. The rotors as they are designed here will not be used by the public
6. The rotors as they are designed here will not be used for any commercial purposes until it is verified that the rotor can operate with the platform and controller safely according to the relevant international design standards for wind turbines.

The first source of errors was in the information for the initial design and the platform. First, there were no load limits provided for the platform. One way to estimate these limits is to simulate the original design. However, the design information for that design was also incomplete. The airfoils were not given and only stiffness properties were given for the structure. To overcome this missing information, we selected a set of airfoils that are typically used in wind energy and assumed similar airfoils would have been used in the original design. For the structure, we assumed a standard spar-cap with 2 shear webs for the internal design. A structural design was developed through an optimization process where the design was varied to match the structural properties given to us. The risk of making these assumptions is that the estimated load envelope could exceed that of the platform causing a catastrophic failure of any of the platform components.

A tower vibration problem was identified when simulating the original design with the properties that were given to us. This indicates that the original design as given to us is unstable. Since it is unlikely that the original design would be successful with the instability problems we must assume the actual tower properties are different and that there is no stability problem. Thus, we assumed there were errors in the tower problems that we should ignore in our analysis. Accordingly we do not have full confidence in the true tower frequencies and we do not have sufficient information to ensure that the rotor does not excite tower modes. The risk is that this design may not be perfectly matched with the actual tower and may cause serious vibration problems with the current tower.

The other source of error was that no information was given about the controller. The controller dictates the rotational rate of the turbine and how pitch control is activated. These are crucial parameters in the loads and performance of the design. Typically, the controller is redesigned or tuned according to the rotor design. Without this information, we cannot simulate the actual operating points of this turbine. Instead, we used the DTU Wind Energy Controller in all our simulations. This controller has been developed purely for research purposes and is not representative of a true industrial controller. It is impossible for us to estimate the constants used in the actual controller, so it made no sense to develop a design based on fixed controller constants. Instead we allowed the optimization to vary these parameters assuming that the actual parameters were similar. We performed some sensitivity analysis to assess the effect of some controller constants. Furthermore, we believe that the controller should be tuned specifically for this design, so it is the responsibility of the user to correct any errors due to the controller tuning. The risks of these assumptions is that the design may not operate as intended. This could increase the loads or degrade the performance. The increased loads could cause failure to the blades and the platform.

### **1.5.2 Overview of the designs**

The overall properties of the five optimized blades and the reference design are listed in Table 1.7, along with their relative changes with respect to the reference blade. Both KB2 and KB3 produce higher AEP than the non-coupled KB1 blade, and we also see that swept KB2 blade performs better than the material coupled design KB3. The increased performance of KB2 is also reflected in the slightly longer blade length of 11.35 m, compared to 11.064 and 11.231 of KB1 and KB3.

As mentioned at the beginning of Section 1.5, the KB4 and KB5 designs have additional constraints placed on the magnitude of sweep and prebend, along with reduced freedom provided to the optimizer in changing the material thicknesses in the laminae. These factors influence the design resulting in lower AEP compared to the non-coupled blade KB1. For instance, a lower limit on backward sweep prevents additional load

reduction benefits through the phenomenon of geometric bend-twist coupling. A lower load reduction potential in turn limits the achievable blade length, which is a major driver of aerodynamic loads. This is seen in the lower blade length values obtained by KB4 and KB5 compared to the three remaining designs. Additionally, KB4 follows a fixed rotor speed schedule based on the tip speed ratio of the reference blade. As a result the KB4, rotor operates at the same rotor speeds as the reference rotor for given wind speeds. This limits the achievable AEP increase as the blade fails to operate at its optimal aerodynamic design points. The influence of the design freedom assigned to rotor speed is seen in the superior AEP of KB5 over that of KB4. This is achieved inspite of only a slight increase of blade length in KB5, pointing to the influential role of rotor speed to facilitate optimal operation of the rotor in the variable speed region.

All blades operate at high tip speed ratio, compared to the starting point of the design optimizations of 7.5. Since the blade mass was a constraint in the optimizations, all five blades have similar mass with KB5 being the heaviest.

Table 1.7: Summary of overall properties of the five optimized blades.

Quantity	Reference	KB1		KB2		KB3		KB4		KB5	
	Value	Value	Change	Value	Change	Value	Change	Value	Change	Value	Change
AEP[MWhr] (A=6, k=2)	212.38	243.82	+14.80%	252.18	+18.74%	249.08	+17.28%	224.67	+5.79%	236.77	+11.48%
Blade length [m]	10	11.06	+10.6%	11.41	+14.1%	11.22	+12.2%	10.48	+4.8%	10.55	+5.5%
Blade mass [kg]	273.16	256.87	-5.96%	257.71	-5.66%	256.65	-6.04%	254.53	-6.82%	260.46	-4.65%
TSR [-]	7.50	10.08	+34.4%	10.62	+41.67%	9.78	+30.39%	7.68	+2.4%	9.77	+30.27%

The differences in the AEP of the five optimized designs and the reference rotor is represented visually in Figure 1.9. The AEPs have been calculated for a Weibull wind climate with average wind speed of 6 m/s. Figures 1.10 to 1.16 show the rotor steady state performance as function of wind speed. The mechanical power generated by the optimized designs is shown in Figure 1.10. It is seen that the only KB4 and the reference blade achieve rated power at a wind speed of 11 m/s whereas the rest of the designs produce rated power at a wind speed of 10 m/s. This due to a shorter variable speed region in KB1, KB2, KB3 and KB5 as a result of the rotor speed being granted design freedom during the optimization. In general, KB4 and reference produce similar power for a given wind speed and is lower than the rest of the designs. This is due to the higher rotor speeds adopted in these designs than compared to KB4, which follows the same rotor speed schedule as the reference. A higher optimal rotor speed results in a higher optimal tip-speed ratio. The rotor speed curves can be seen in Figure 1.16. All the designs except for KB4 and the reference attain the rated rotor speed of 70 rpm between 8 and 9 m/s, whereas KB4 and the reference rotor attain the maximum rotor speed between a wind speed of 10 and 11 m/s.

The power coefficient curves shown in Figure 1.13 are seen to decrease in the bend-twist coupled designs with increasing loading due to increase in wind speeds. This is especially true in the KB2 swept blade, where the high magnitude of sweep causes a high value of torsion towards feather decreasing the angle of attack from the design point resulting in a decreased lift coefficient and hence a reduced power coefficient. Due to additional constraints on the maximum attainable sweep placed in the KB5 swept blade design, the decrease in the effective angle of attack caused by increasing magnitudes of torsion with rising wind speeds is not large enough to cause the blade sections to operate outside the optimal aerodynamic region. Thus, the power coefficient remains constant until the rated rotor speed is achieved, beyond which a decrease in the tip-speed ratio causes the observed decrease in the power coefficient. The same trend in the power coefficient is also observed in the KB1 non-coupled blade where there is no bend-twist coupling phenomenon affecting the performance. However, the bend-twist coupled blades show a reduction in the thrust coefficient with increasing wind speeds due to the corresponding rise in magnitudes of torsion towards feather. This can be observed in the thrust coefficient curves shown in Figure 1.14. It is noted that the rate of decrease in the power coefficient of the coupled designs is lower than the corresponding rates of decrease in the thrust coefficient, highlighting the effectiveness of bend-twist coupling towards feather as a load reduction method. Beyond the attainment of the rated rotor speed a decrease in thrust coefficient is also observed in the non-coupled KB1 blade along with the coupled designs. The high tip speed ratio (TSR) operation causes the constant TSR region to end between 8 and 9 m/s, as they attain the rated rotor speed. Beyond this point the decreasing TSR with rising wind speed results in a reduction in  $C_T$ , which has a beneficial effect on also tip deflection resulting in an unloaded blade tip region. This is a common feature in all the optimized blades apart from KB4, where the decrease in the thrust coefficient is primarily due to bend-twist coupling.

The thrust curves of the five designs are shown in Figure 1.12. Here too the designs operating at higher rotor speeds and corresponding high tip-speed ratios have a greater magnitude of thrust than KB4 and

reference blades for the same wind speeds. They attain peak thrust corresponding to maximum rotor speed at a wind speed between 8 and 9 m/s, lower than that of KB4. Furthermore, the peak thrusts for the swept blade designs of KB2, KB4 and KB5 are seen to not exceed the peak thrust in the reference case. The peak thrust in KB1 and KB3 are marginally higher than the reference case but within the acceptable deviation of 7%.

Finally, the pitch curve of the optimized designs is shown in Figure 1.15. The blade is not pitched until it reaches the rated rotor speed, beyond which the blades are pitched to curtail loads and power.

Figure 1.11 depicts the ratio of the power produced in the optimized rotors to that of the reference rotor. It is seen that the KB2 swept blade significantly outperforms the rest of the design with regards to this metric. The KB3 blade is seen to produce more than the rated power for the region above the rated wind speed. It should be noted that the extra power being produced in the KB3 design stems from the difference in the tool used for its aeroelastic evaluation compared to the rest of the blades. KB3, being a material coupled design, had to be evaluated using the time domain aero-servo-elastic tool HAWC2, whereas the rest of the designs were evaluated with the HAWCStab2 aeroelastic solver. This was required as HAWCStab2 currently lacks the functionality to evaluate material coupled designs. Being a time domain tool, HAWC2 requires a tuned controller to curtail the power output to rated, for the region above the rated wind speed. The need to tune the controller arises with a change in the rotor design. The optimization framework provided by HawtOpt2 currently lacks the capability to tune the controller for the constant speed region above the rated wind speed. Thus, KB3 operates with the tuning parameters from the reference blade. The influence of the performance of the turbine in the region above the rated wind speed is minimal on the optimization and the resulting final design. Since this region is pitch controlled, the loads will not exceed those experienced in the variable speed region. The load reduction in the variable speed is one of the main design drivers in the aeroelastically tailored blade for a pitch regulated variable speed turbine. Additionally, the high wind speeds encountered above rated have a low chance of occurrence for the given wind climate. Finally, it was decided to proceed with a swept blade design and hence additional resources were not spent in the tuning of the controller and reevaluation of the KB3 design with the tuned controller, especially since it is not expected to result in a significant difference over the current design.

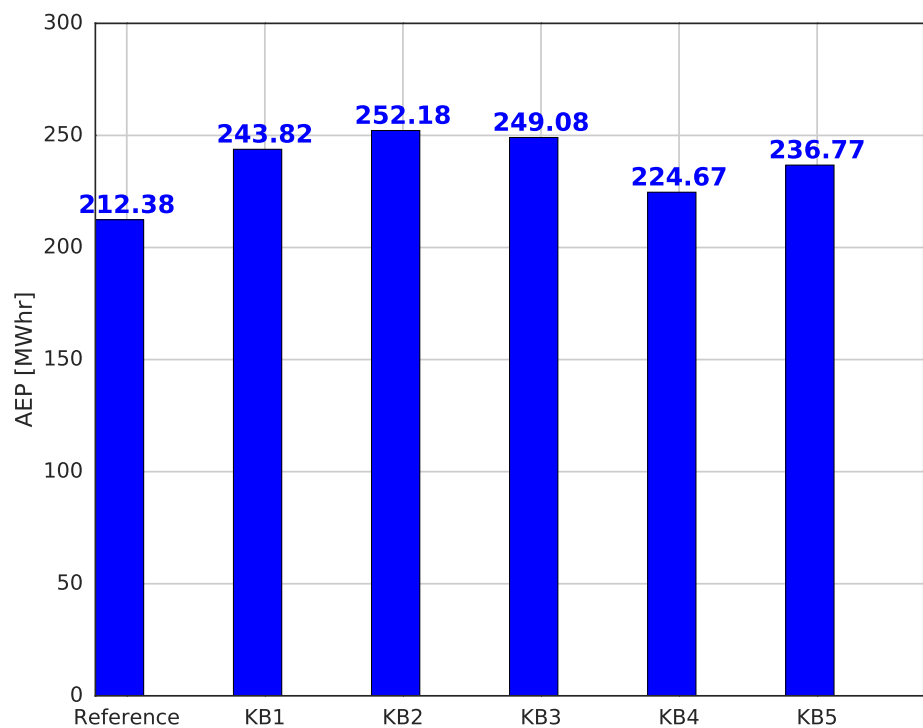


Figure 1.9: Annual energy production of the five optimized blades for a Weibull wind distribution with scale factor  $A=6.0$  m/s and shape factor  $k= 2.0$  [-].

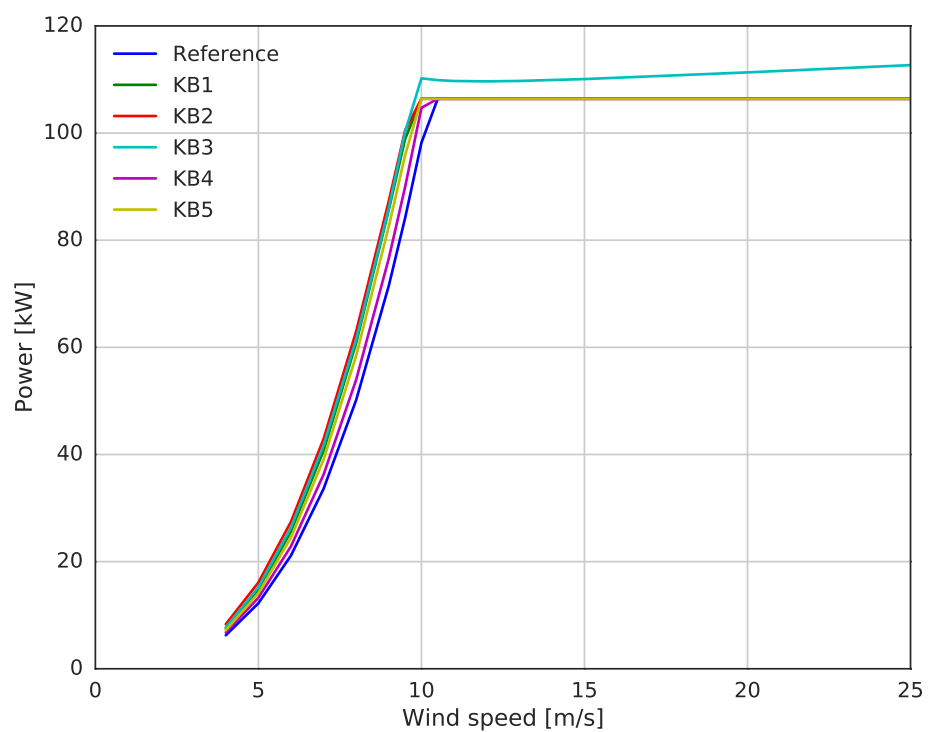


Figure 1.10: Mechanical power as function of wind speed for the five optimized blades.

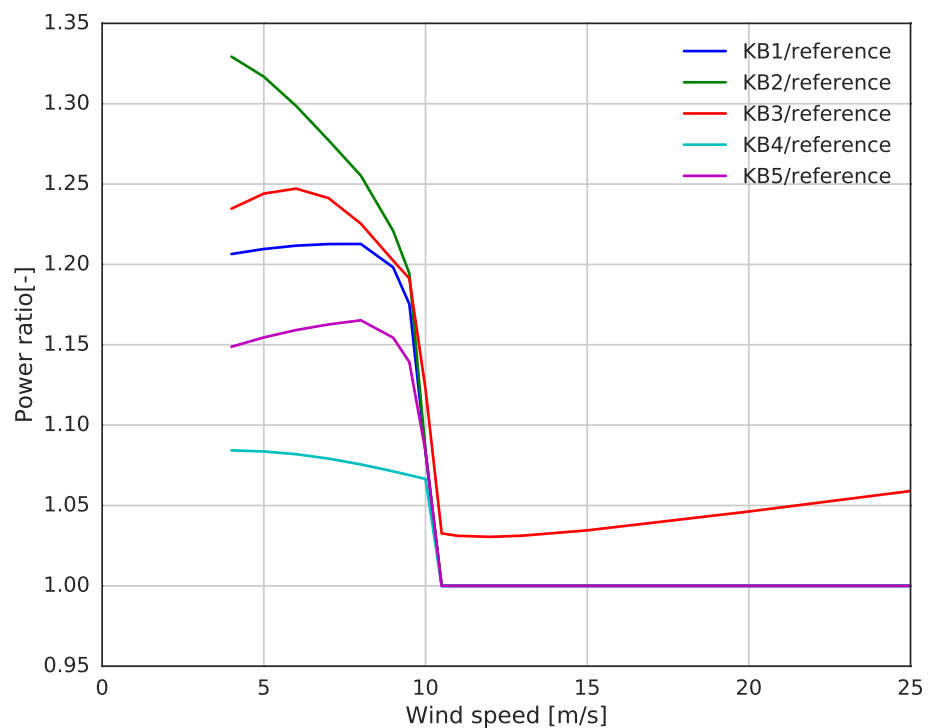


Figure 1.11: Ratio of mechanical power as function of wind speed for the optimized blades relative to the reference.

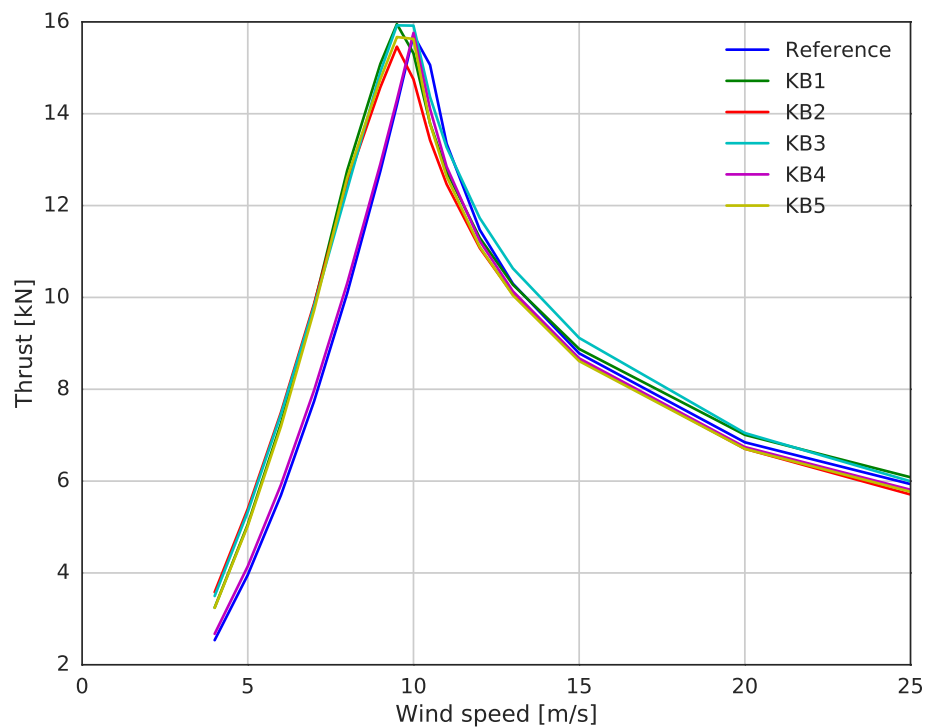


Figure 1.12: Rotor thrust as function of wind speed for the five optimized blades.

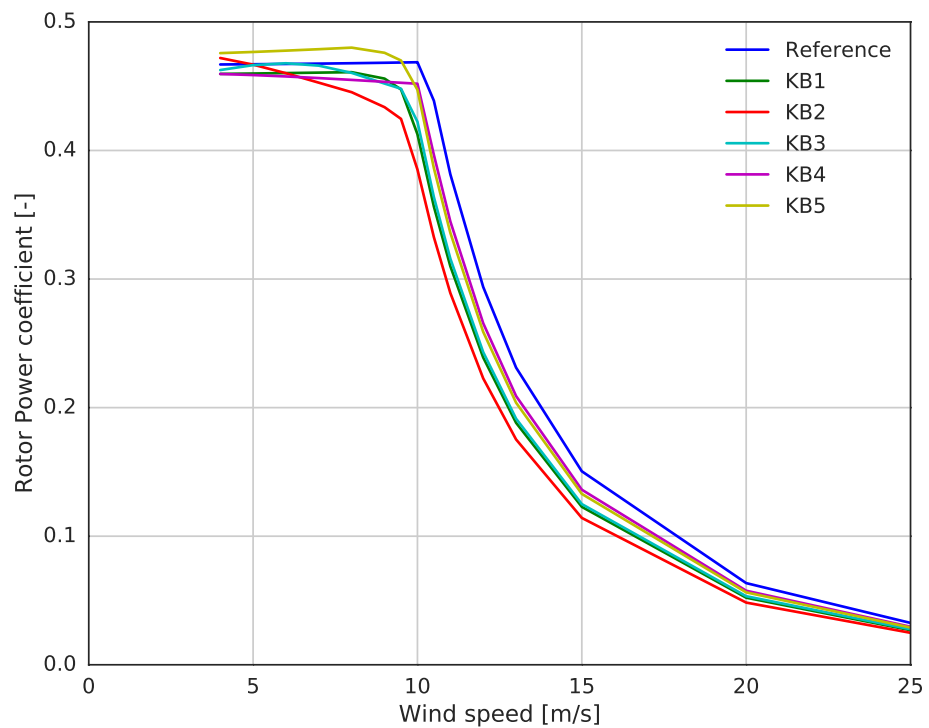


Figure 1.13: Mechanical power coefficient as function of wind speed for the five optimized blades.

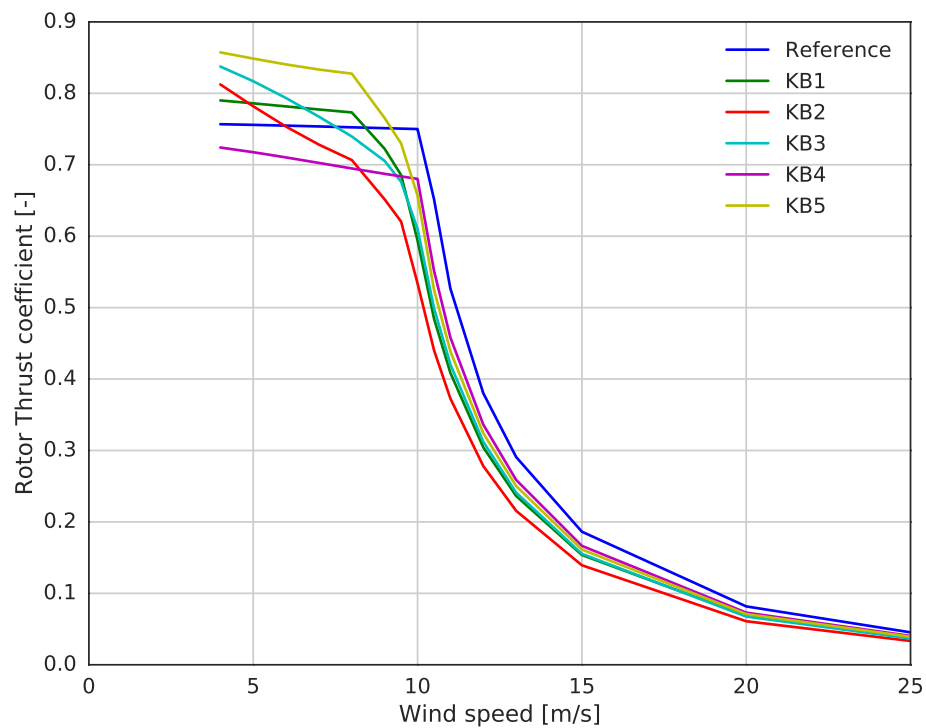


Figure 1.14: Rotor thrust coefficient as function of wind speed for the five optimized blades.

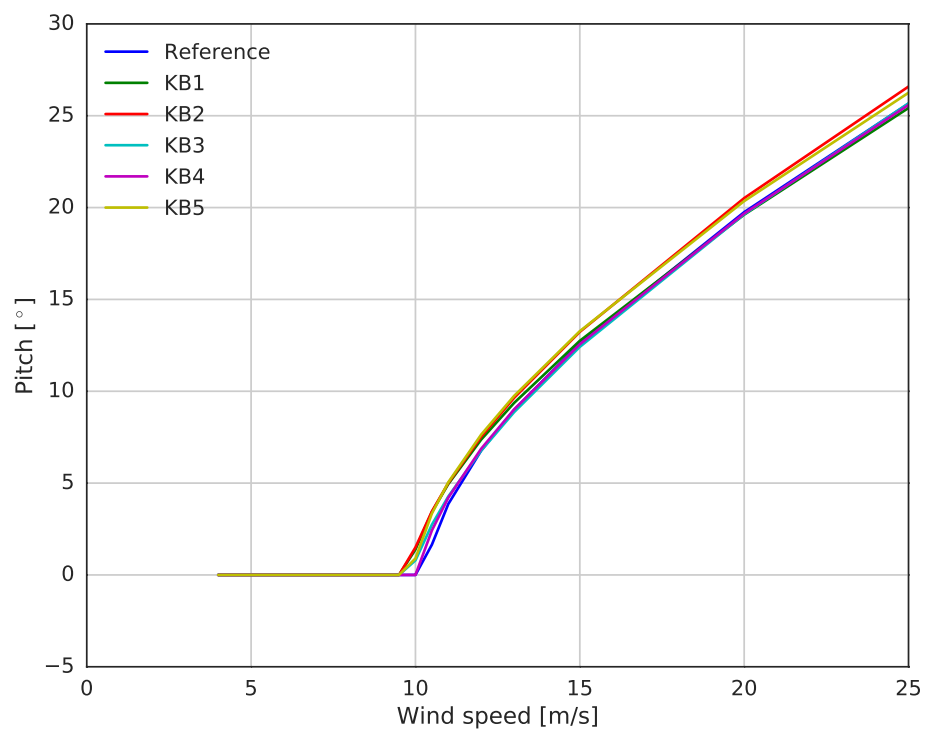


Figure 1.15: Blade pitch as function of wind speed for the five optimized blades.

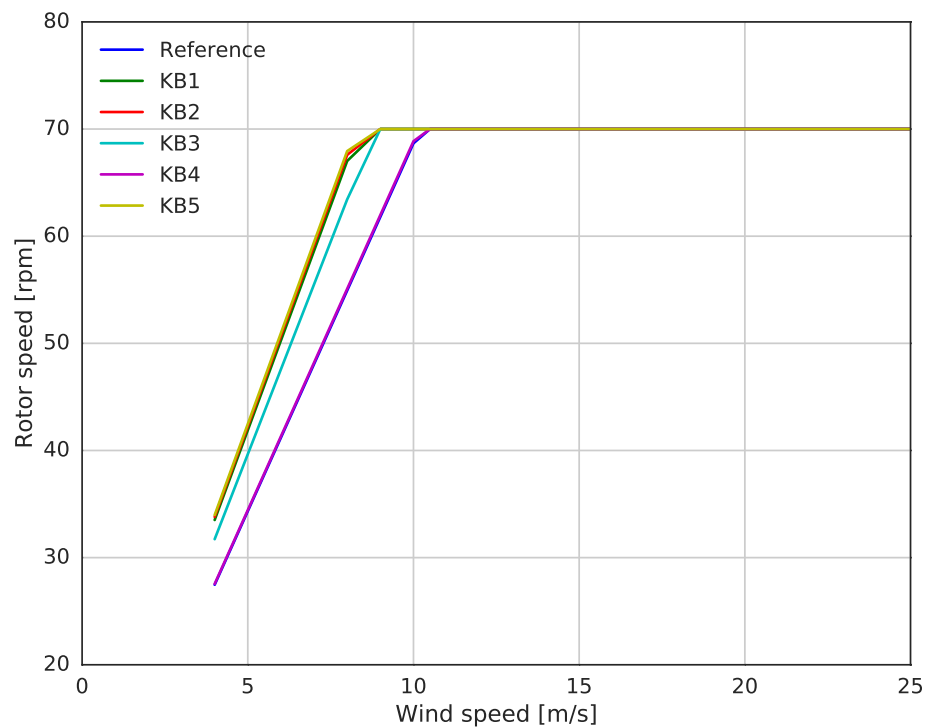


Figure 1.16: Rotor speed as function of wind speed for the five optimized blades.

Figures 1.17 to 1.22 show the blade planform for the five blades compared to the reference. All five blades have a more slender planform than the reference resulting from the high TSR, which enables driving down blade mass. The material coupled blades have higher twist distributions than the non-coupled blades towards the blade tip due to the torsional coupling, as seen in Figure 1.18. The optimized blades generally have higher airfoil relative thicknesses, particularly near mid-span, where there are the highest demands for stiffness and strength, as seen in Figure 1.19. Towards the root the relative thicknesses decrease due to the high chord which provides sufficient blade thickness and therefore stiffness. The optimizer can also alter the position of the cross-section relative to the blade axis, referred to as pitch axis aft leading edge. This is shown in Figure 1.20. This affects the positioning of the spar cap within the cross-section as well as the aerodynamic pitch moment. For all blades, the cross-section is moved forward towards the tip but is somewhat less pronounced for the KB3 and KB4 blades.

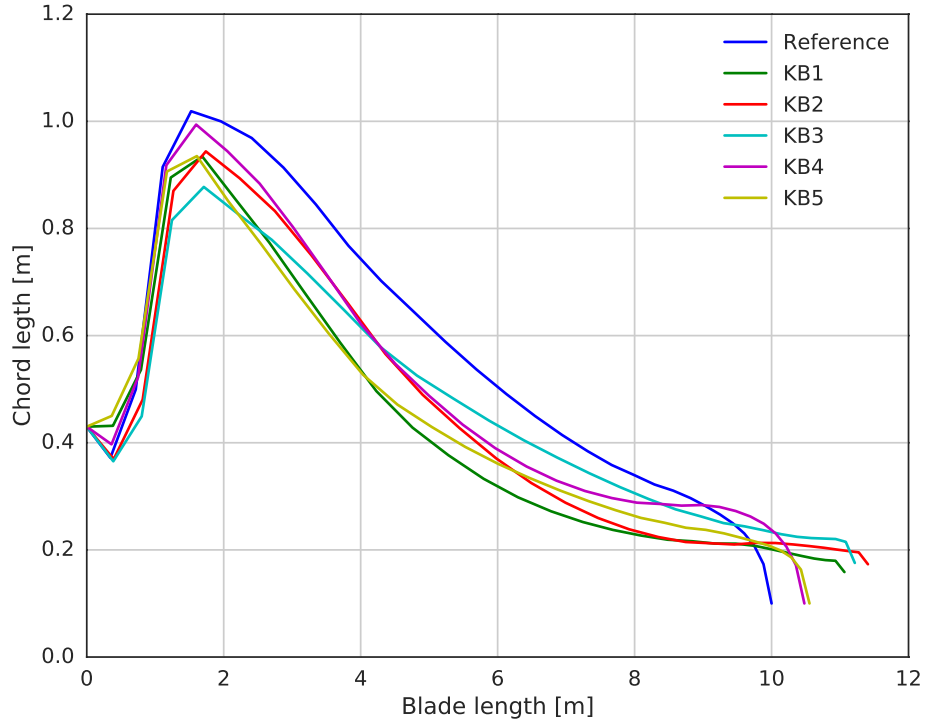


Figure 1.17: Blade chord distributions for the five optimized blades.

### 1.5.3 Structural Design

The overall structural topology is the same for all five blades, shown in Figure 1.7. As summarized in the optimization setup, Table 1.5, the spar cap width was allowed to change linearly from root to tip for KB1, KB2 and KB3 optimizations. Figure 1.23 shows the resulting spar cap widths for the five blade designs compared to the reference design. The two blades without sweep, KB1 and KB3, result in an increased cap width in the blade root, whereas the swept design of KB2 ends up with a more slender spar cap. Changing cap width did, however, not change the distance between the two main shear webs, see Figure 1.2 for a schematic of the cross-section parametrization.

The spar cap width is not afforded design freedom for the KB4 and KB5 swept blades and hence follow the same trend as the reference case, albeit with higher magnitudes. The increased magnitudes are attributed to the greater lengths seen in the two blades compared to the reference, as it is scaled with length. KB5 has a slightly greater blade length than KB4 as seen in Table 1.7. This is reflected in the spar cap width for KB5 being marginally higher than that of KB4 as seen in Figure 1.23. Not affording design freedom in these two blades limits the influence of the spar cap width in affecting the structural stiffnesses in the

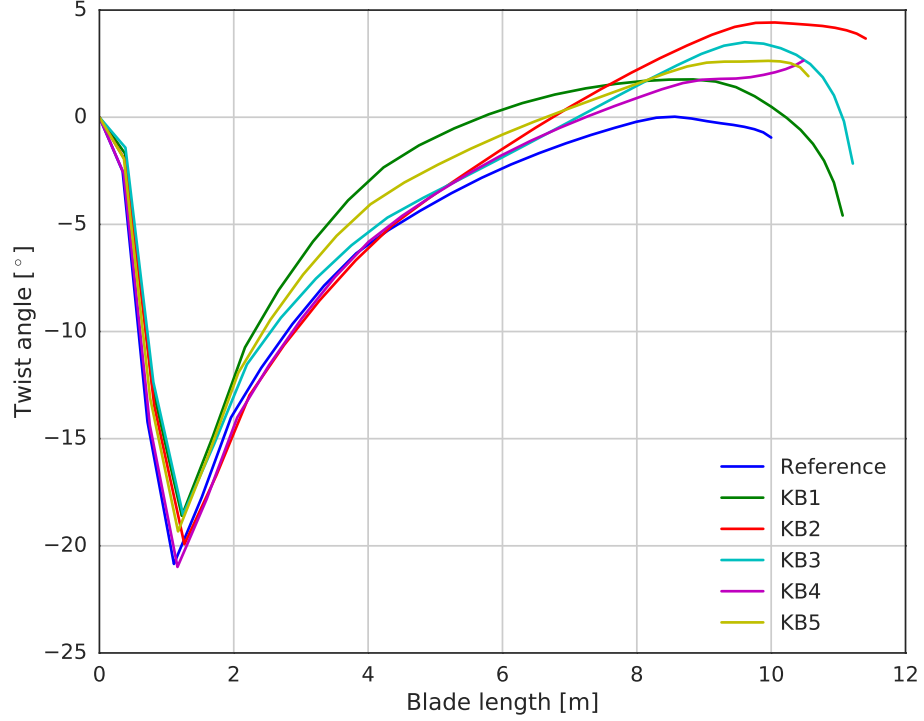


Figure 1.18: Blade twist distributions for the five optimized blades.

swept region of the blade. In contrast, the KB2 blade has a decreased spar cap width in the backward swept region contributing to reducing the stiffnesses and thus aiding in bend-twist coupling by facilitating greater torsion towards feather.

Figures 1.24 and 1.25 show the lofted blade shape seen from the tip and top indicating the locations of region division points, spar cap, and shear webs.

## 1.6 Selected blade design - KB5 swept blade

This section focuses on the evaluation of the selected optimized design that is the KB5 swept blade. Based on the results of the initial optimizations performed in KB1, KB2 and KB3 it was decided to select geometric sweep as the only source of bend-twist coupling. Even though the two coupled designs namely KB2 and KB3, provide similar steady state performance the AEP and power produced by the swept blade design in KB2 is superior to that of the material coupled design in KB3. This can be seen from Figure 1.9 and Figure 1.11. Hence, a swept design was selected for the final blade. Furthermore, in order to facilitate ease of manufacturing of the blades only backward sweep is allowed in the design with a maximum value limited to almost half the value of that chosen for the KB2 swept blade design. Additionally, an extra layer of triax material is added throughout the blade that is not allowed any design freedom. These restrictions limit the extent to which the optimization could leverage the load reductions caused by the geometric coupling to increase the blade length and hence produce greater AEP than possible with the current constraints in place. Thus, as a result of the additional constraints the optimized KB5 design produces less power than the KB2 design.

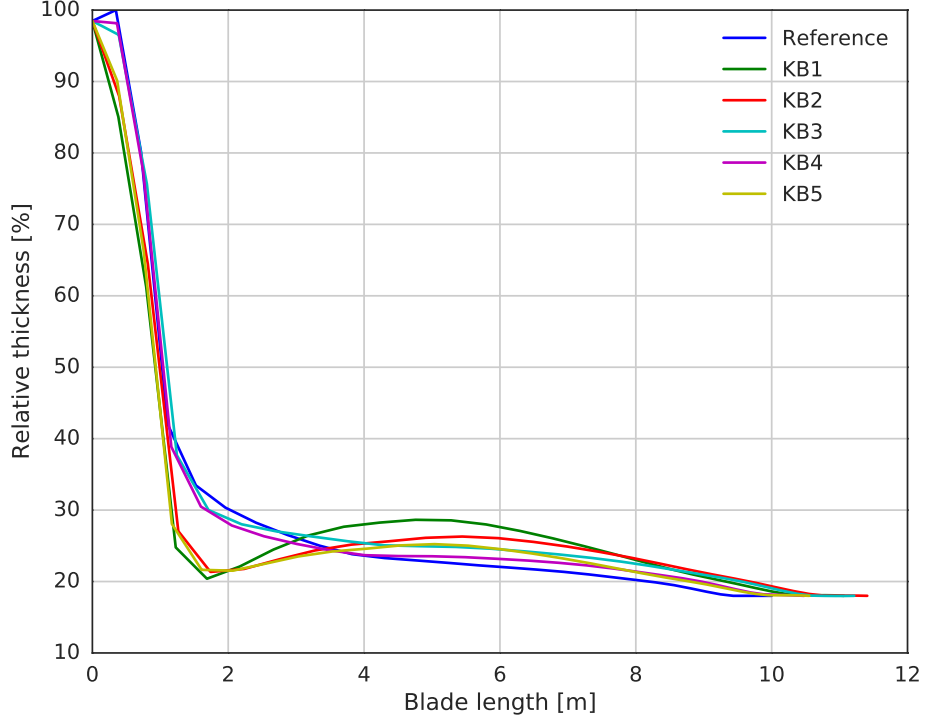


Figure 1.19: Blade relative thickness distributions for the five optimized blades.

### 1.6.1 Multidisciplinary optimization

The value of the objective function for every iteration of the optimizer is shown in Figure 1.26. The objective function has been defined in Equation 1.1 and it starts with a value of  $-1$  which represents the reference blade. As the optimizer evaluates the design space and leverages the design variables, objective and constrains the changes in the design with each iteration alters the value of the objective function. The aim is to minimize the objective function that is to obtain the highest attainable magnitude of the objective function which corresponds to the maximization of the AEP. It is seen in Figure 1.26 that the objective function represented in blue, decreases with increasing optimizer iterations indicating a successful progression of the problem. As the optimizer solves for the optimal design it inadvertently attains designs from the possible design space which exhibit violations of the constraints imposed on the problem. The constraint violations are shown in red on a log scale. The green dots on the objective function curve represent the attained designs which adhere to the bounds set by the various constraints. The chosen design is the minimum value of the objective function for which no constraint violation has been recorded.

The constraints imposed on the problem have been introduced in Table 1.6. Figure 1.27 represents the absolute values of the constraints normalised by their corresponding maximum limits. These constraints have been recorded at the chosen optimal solution of the design. The constraint that has a value which is more than 90% of its maximum limit is considered to be active and is responsible for affecting the obtained solution. The active constraints from Figure 1.27 are shown in Table 1.8.

### 1.6.2 Planform

The planform of the KB5 swept blade is compared to the reference blade in Figure 1.28 and Figure 1.29. The chord length is seen to have decreased from the reference, as seen in Figure 1.28a. The reduction is greatest in the mid-span region of the blade. Additionally, the relative thickness of the blade sections have increased from the reference in the mid-span region. The decreased chord and increased relative thickness

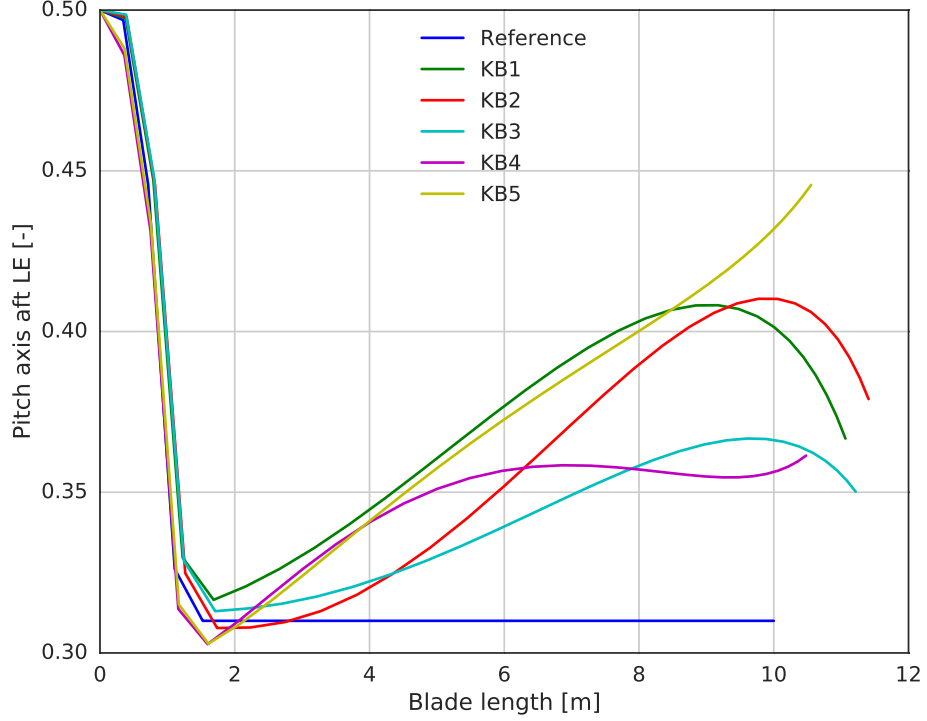


Figure 1.20: Non-dimensionalized blade axis leading edge offset distributions for the five optimized blades.

Table 1.8: Active constraints for KB5

Quantity [-]	Description
Q_con	Steady state thrust
Mx_con	Steady state flapwise root bending moment
tip_pos_b2	Blade tip deflection from reduced DLB for blade 2
pb_con	Prebend
sw_con	Sweep
tip_pos_b3	Blade tip deflection from reduced DLB for blade 3
blade_failure_index_ks	Blade failure index or strain index
MzBR3_max	Maximum blade root torsion for blade 3 from reduced DLB
FyTT_min	Tower top flapwise force from reduced DLB
MzBR1_max	Maximum blade root torsion for blade 1 from reduced DLB
tip_pos_b1	Blade tip deflection from reduced DLB for blade 1
T_con	Steady state rotor thrust force
MxTB_con	Tower bottom fore-aft bending moment from reduced DLB
mass_con	Blade mass

indicate a much slender blade profile than the reference. The twist angle is seen to increase in Figure 1.28b. It should be noted that the twist plotted in this figure, follows the right hand thumb rule convention for a z-coordinate axis that starts at the root and ends at the tip. Accordingly, it is regarded negative towards feather and positive towards stall. The twist in the KB5 blade has decreased compared to the reference case and is twisting less towards feather. This is to accommodate an increased tip-speed ratio of operation and the consequences of a slender blade design which has altered the angle of attack for which the airfoils can operate optimally. It is also observed from Figure 1.28b that difference between the twist angles of KB5 and the reference increase further in the last 20-25% of the blade. This is due to the additional effect of torsion arising as a consequence of the geometric bend-twist coupling, to reduce the angle of attack by

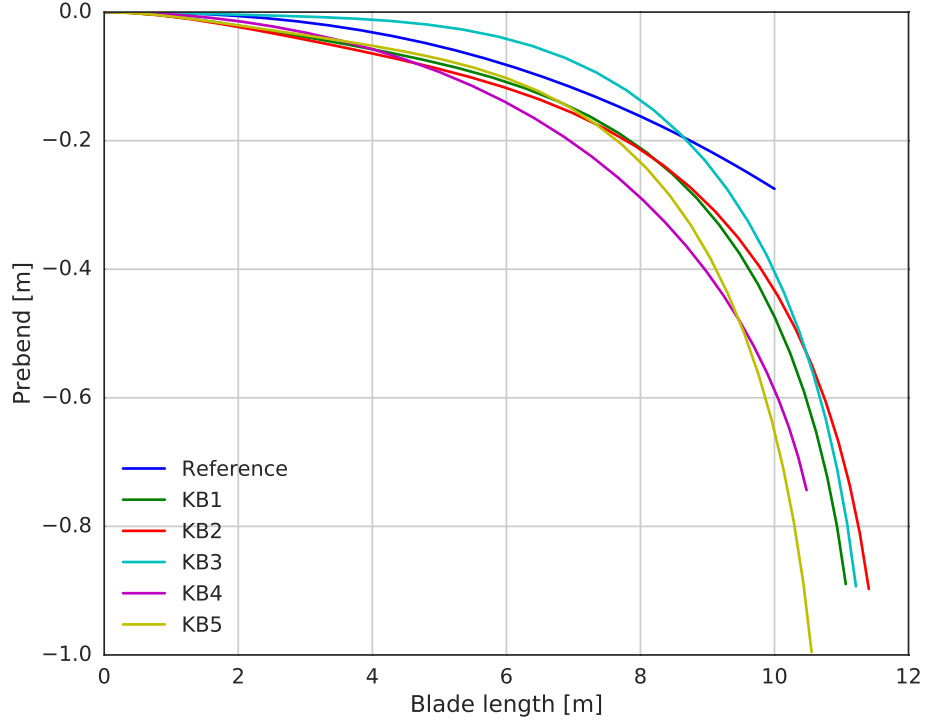


Figure 1.21: Blade pre-bend distributions for the five optimized blades.

twisting towards feather. As such the pre-twist attains less negative values to compensate for this effect and to allow the airfoils in the affected region to operate optimally.

### 1.6.3 Structure

#### Composite layup

The material layup in the various regions of the blade sections along with the corresponding laminate thicknesses are shown in Figures 1.30 to 1.34. The two outer triax layers remain unchanged while the rest of the internal layers are afforded design freedom during the optimization and vary according to the solution.

Figure 1.30 shows the material information in the trailing edge reinforcement of the blade. Referring to the blade cross-section shown in Figure 1.2, this region is between the points DP00 and DP02 on the pressure side and between DP15 and DP17 on the suction side. It is seen that compared to the reference the KB5 blade has a greater thickness in this region especially near the root. This has been carried out by adding more uniax material.

Figure 1.31 depicts the material layup in the main panel of the blade which is situated between the spar cap and trailing edge reinforcement. In Figure 1.2 showing the cross-section information, this region lies between the points DP02 and DP04 on the pressure side and between DP13 and DP15 on the suction side. In this region the laminate thicknesses are mostly similar to the reference blade. Except near the root it is less thicker. This has been done by reducing the uniax material. Similarly the thickness is greater from 20% to 40% blade length. This has been facilitated by increasing the triax material in the layup.

Figure 1.32 presents the material layup in the spar cap of the blade. From Figure 1.2 it is seen that this region lies between the points DP04 and DP07 on the pressure side and between DP10 and DP13 on the suction side. The thickness of the laminate from 40% span to 90% span has been reduced considerably, by

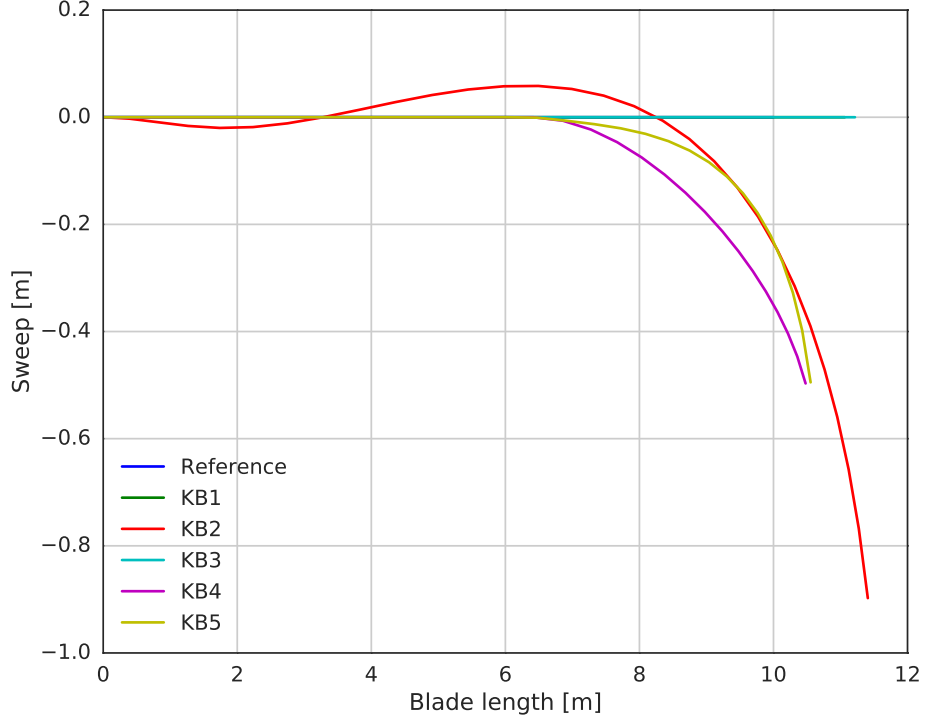


Figure 1.22: Blade sweep distributions for the five optimized blades.

a factor of two on average. At the same time, the thickness between the root and around 30% span has increased compared to the reference. This has been mainly done by altering the uniax material. Two thin layers of triax have also been added.

Figure 1.33 shows the material distribution and laminate thickness in the leading region of the blade situated between the leading edge and the spar cap. On referring to Figure 1.2 it is seen that this region lies between the points DP07 and DP08 on the pressure side and between the points DP09 and DP10 on the suction side of the blade section. The laminate thickness has been reduced in the KB5 blade in the near root region, while it has been slightly increased from 20% to 40% span. The reduction in the laminate thickness is due to the removal of the uniax layer near the root. Whereas a layer of triax has been added throughout the early span and is responsible for the increase in thickness from 20% to 40% span.

Figure 1.34 shows the material information in the leading edge reinforcement of the blade. From the cross-section shown in Figure 1.2 it is seen that this region lies between the division points DP08 and DP09 and includes the leading edge. The laminate thickness has increased from the near root region until 50% span. This increase is primarily due to the addition of two triax layers. The thickness has also increased from around 70% span until the tip. The increase here is attributed to the addition of uniax material in the layup.

The material in the shear webs are not provided design freedom during the optimization and remain unchanged in thickness and material composition.

### Blade stiffnesses

Figure 1.35 presents the flapwise, edgewise and torsional stiffnesses of the KB5 blade compared to the reference over a normalized span. All three stiffnesses are seen to have decreased for majority of the blade span except at the root and tip, which show a slight increase. This is a result of the reduction in the chord length in the KB5 blade compared to the reference as seen in Figure 1.28a. Cross-sectional stiffnesses in a thin composite laminate section scale to the cube of the local chord and scale directly with the laminate

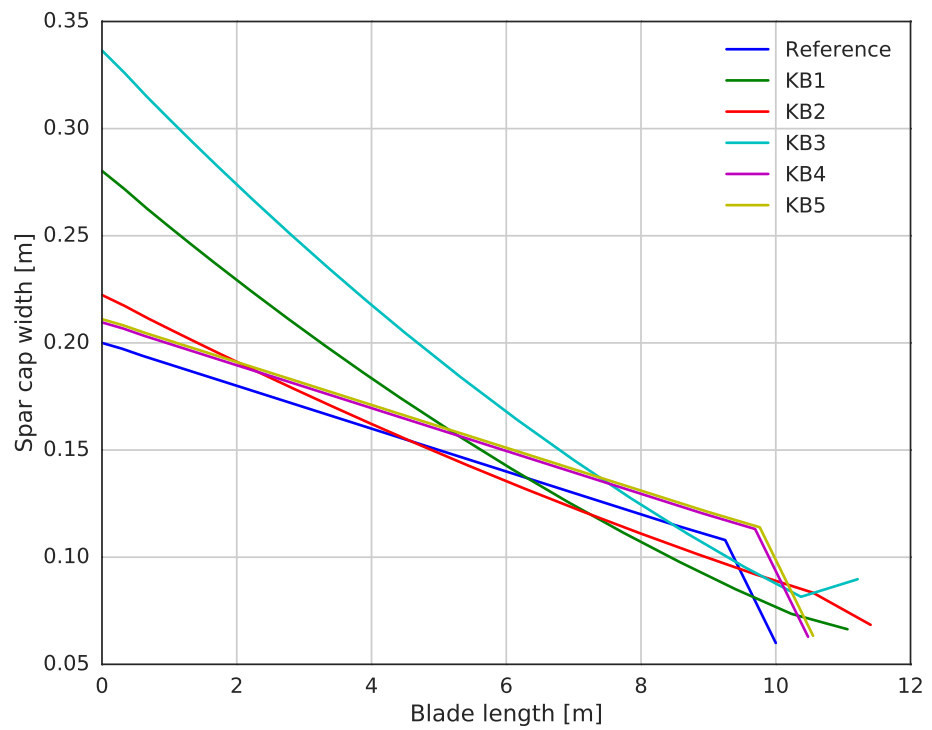


Figure 1.23: Blade spar cap width distributions for the five optimized blades.

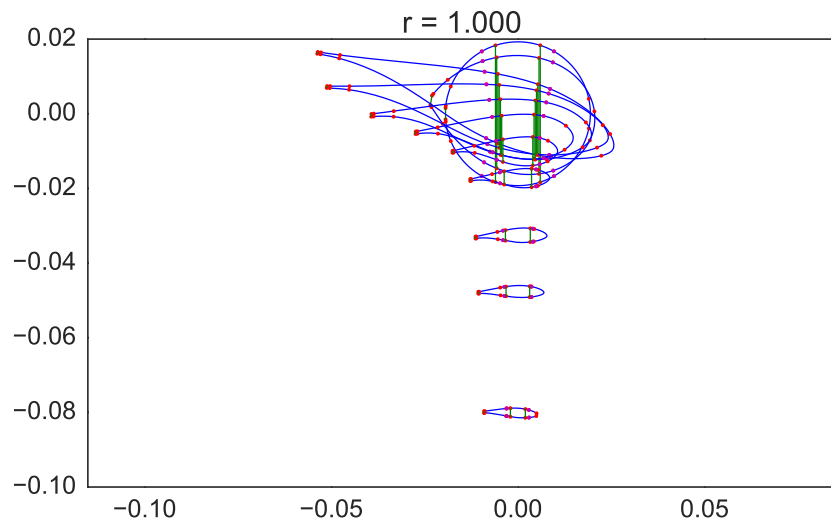


Figure 1.24: Tipview schematic of the KB1 blade structure.

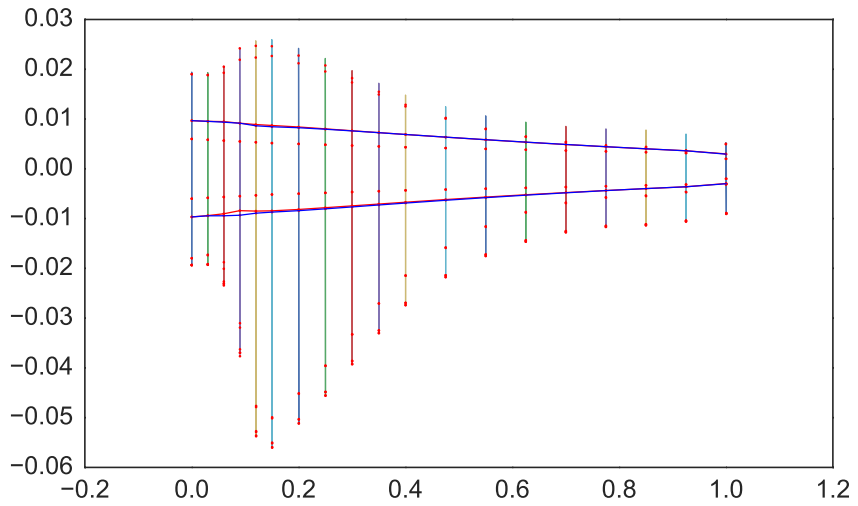


Figure 1.25: Topview schematic of the KB1 blade structure.

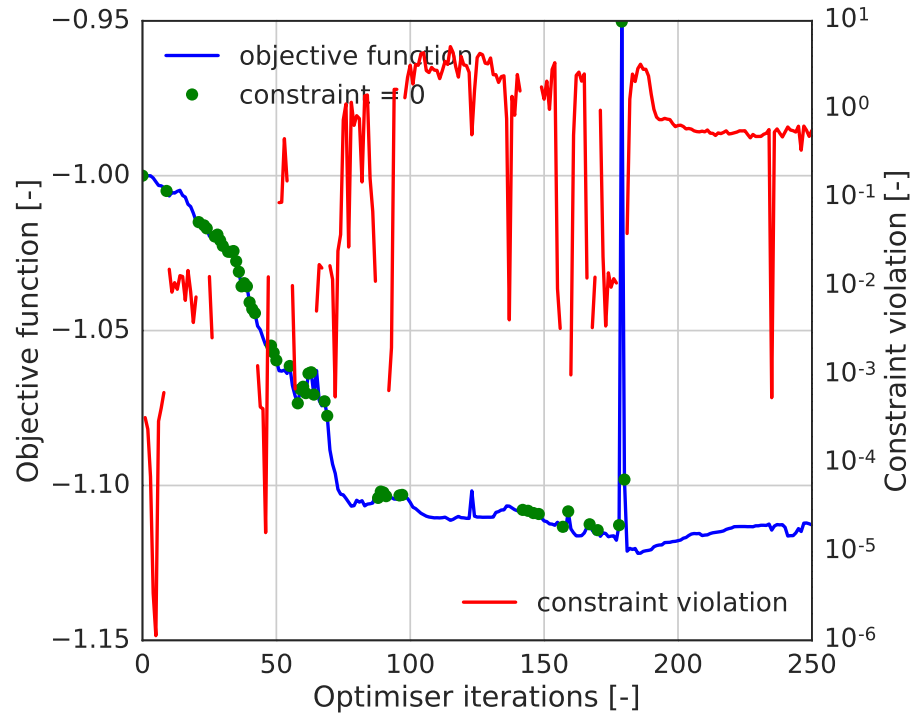


Figure 1.26: Evolution of objective function and constraint violation for increasing iterations of the optimizer.

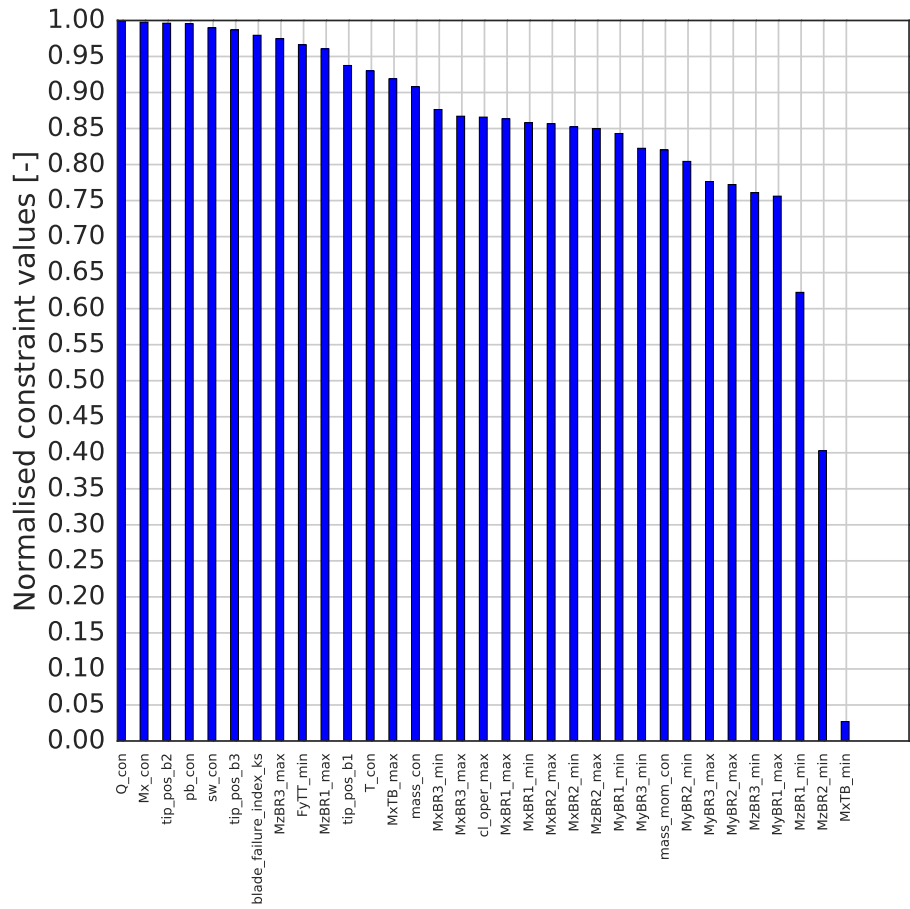


Figure 1.27: Normalised values of constraints depicting the main design drivers.

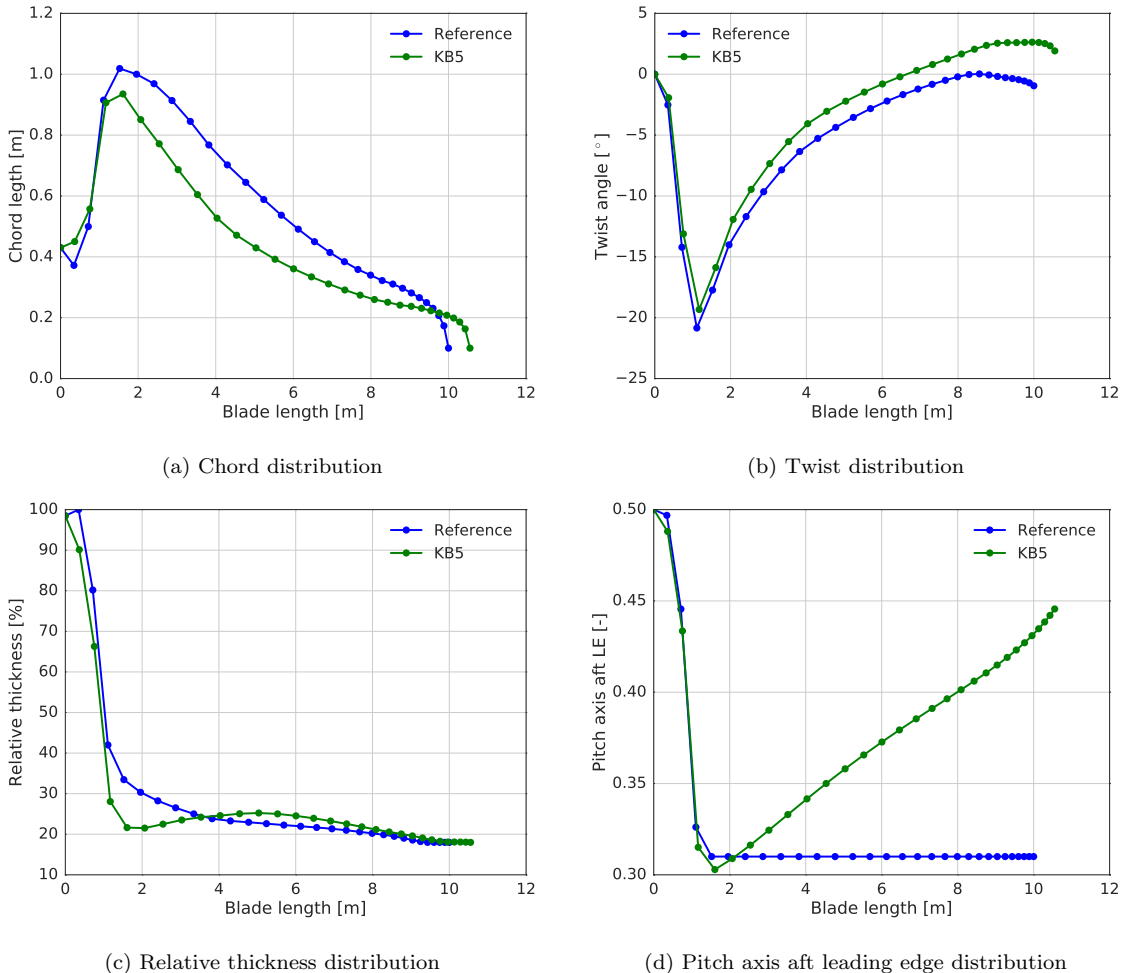


Figure 1.28: Blade planform properties

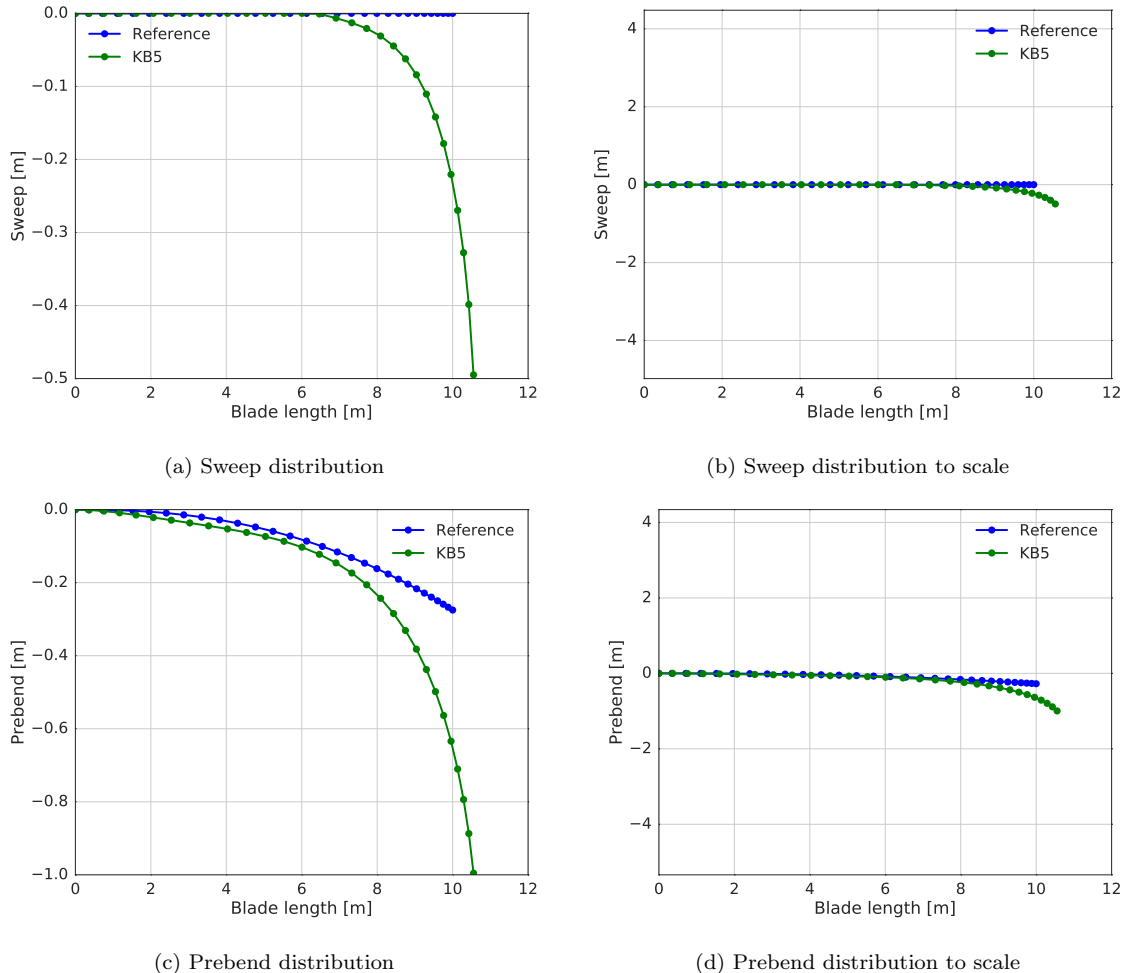


Figure 1.29: Blade planform properties

thickness. This dependence can be derived by applying classical laminate theory to a thin cross-section. The reader is directed to the ECN report by Kooijman [?] for the actual derivation. From the previous section it is seen that the laminate thicknesses too have been reduced considerably in the spar cap region, which is the structural entity that contributes the most towards cross-sectional stiffness.

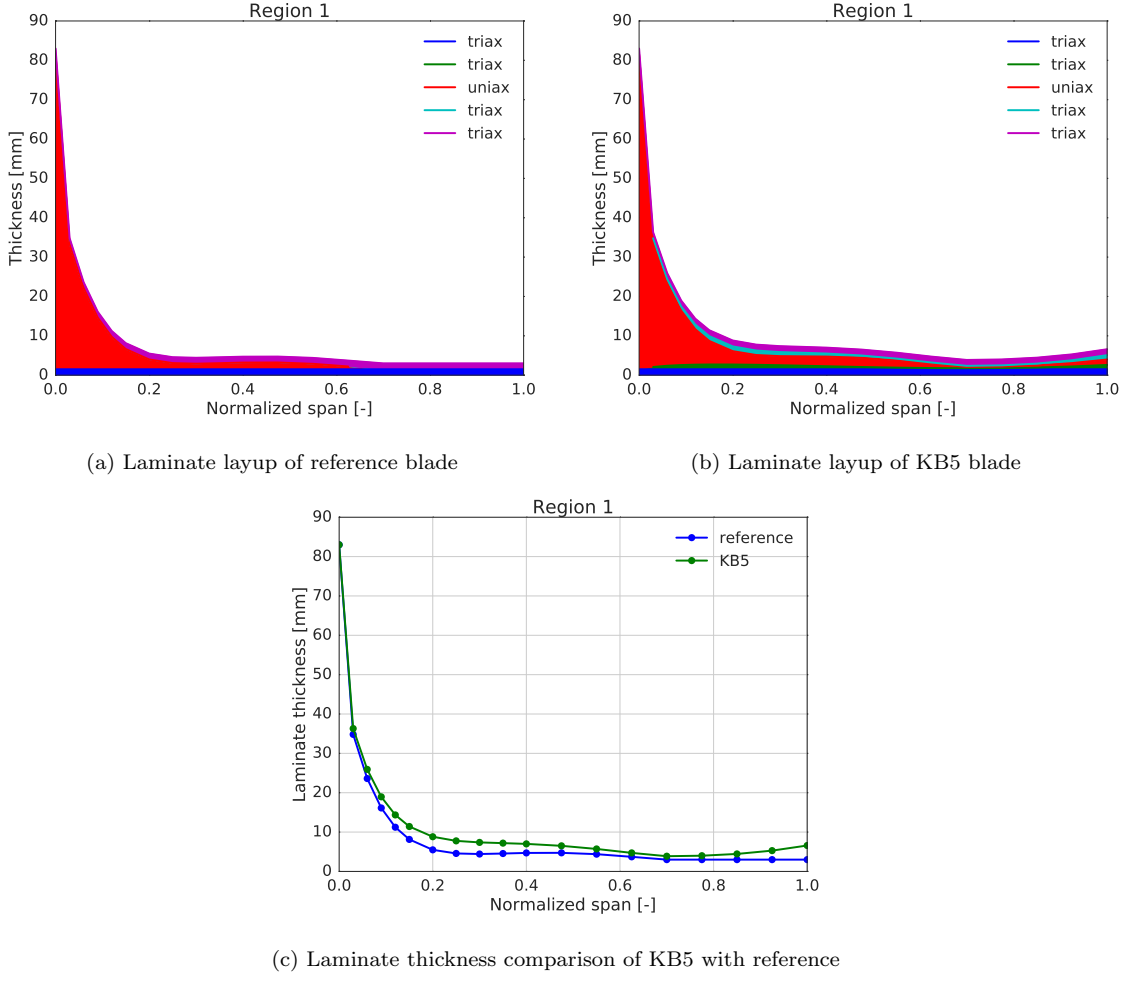


Figure 1.30: Material in the trailing edge reinforcement

#### 1.6.4 Steady-state performance

The steady state operational performance and load response are discussed. It is important to note that the results being discussed in this section pertain to the response of the blade design as recorded during the optimization. The calculations during the optimization are performed in the aeroelastic code HAWCStab2, wherein a nonlinear finite element beam model is coupled with an unsteady blade element momentum (BEM) aerodynamic model considering induction from the shed vorticity, dynamic stall and dynamic inflow [?].

The steady state power and thrust of the KB5 rotor is shown in Figure 1.36. The KB5 rotor generates rated power at a wind speed of 10 m/s whereas the reference rotor produces the same at 11 m/s, as seen in Figure 1.36a. The power produced by KB5 is higher in the variable speed region with the greatest difference of 11.4 kW observed at a wind speed of 9.5 m/s. From Figure 1.36b presenting the thrust curve, it is seen that the thrust too is greater in KB5 in the variable speed region. However, the peak thrust produced at a wind speed of 9.5m/s is 0.5% lower than the reference turbine. The optimal power coefficient for the KB5 rotor is 0.476 and is held constant in the variable speed region until the wind speed

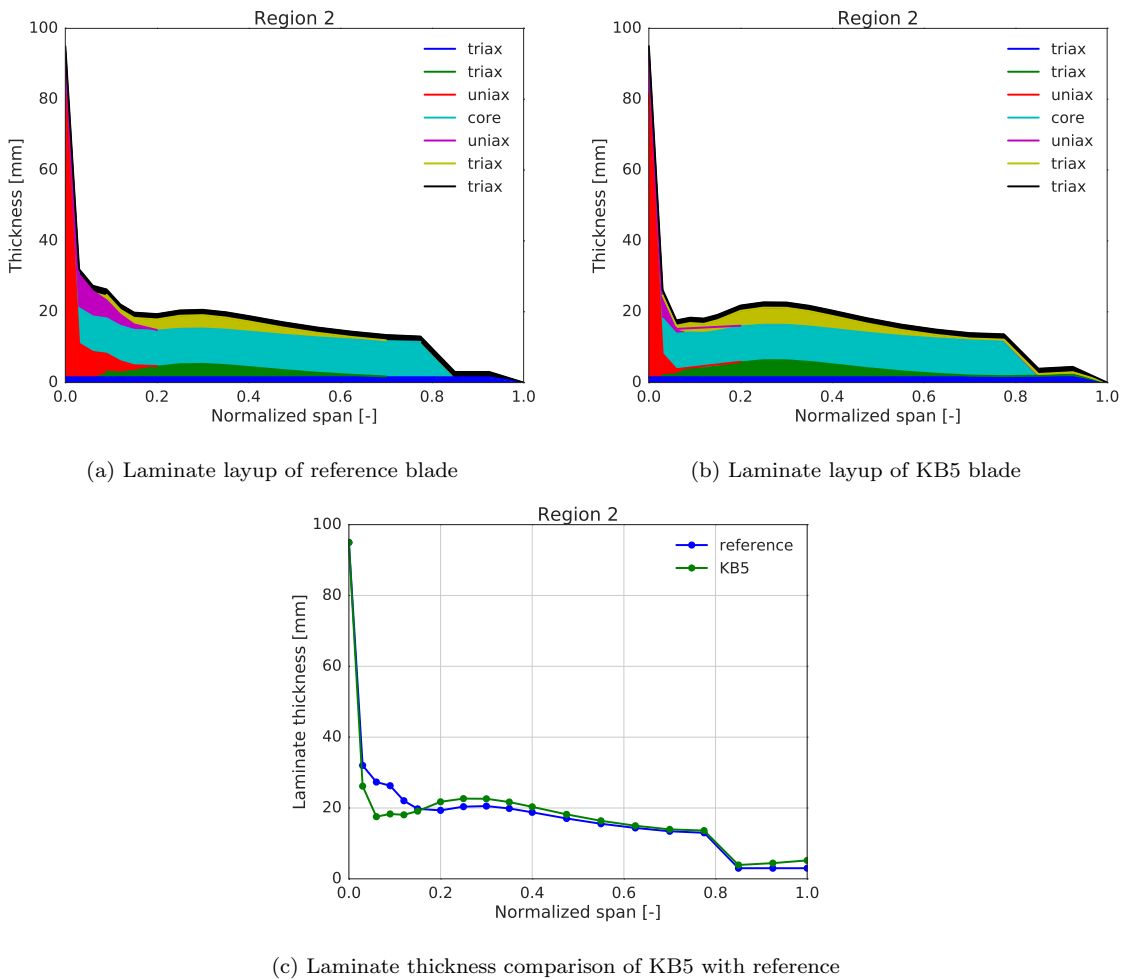


Figure 1.31: Material in the main panel (immediately behind the spar cap)

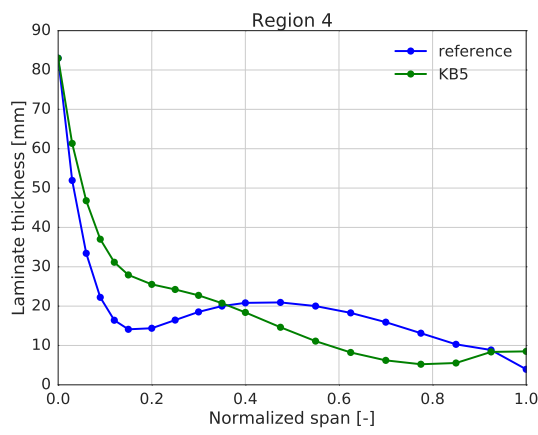
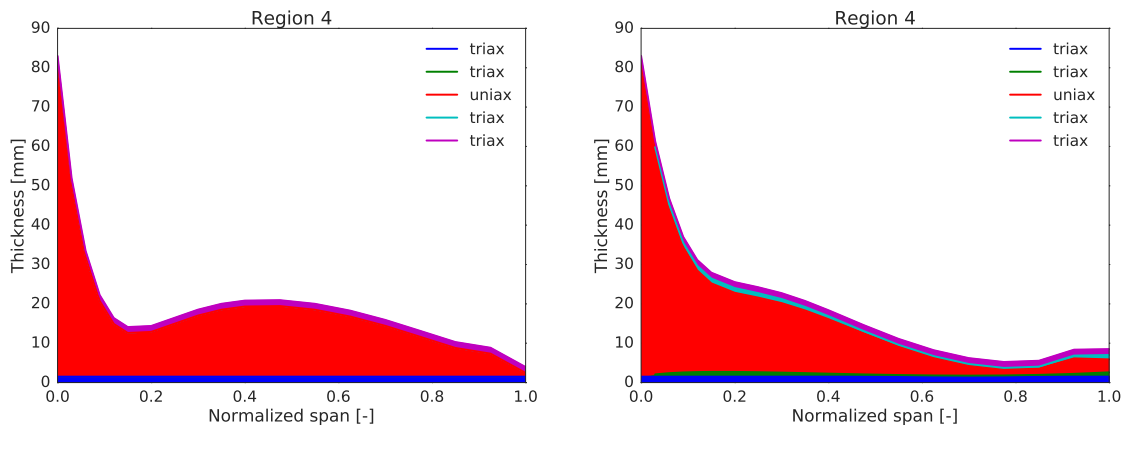


Figure 1.32: Material in the spar cap

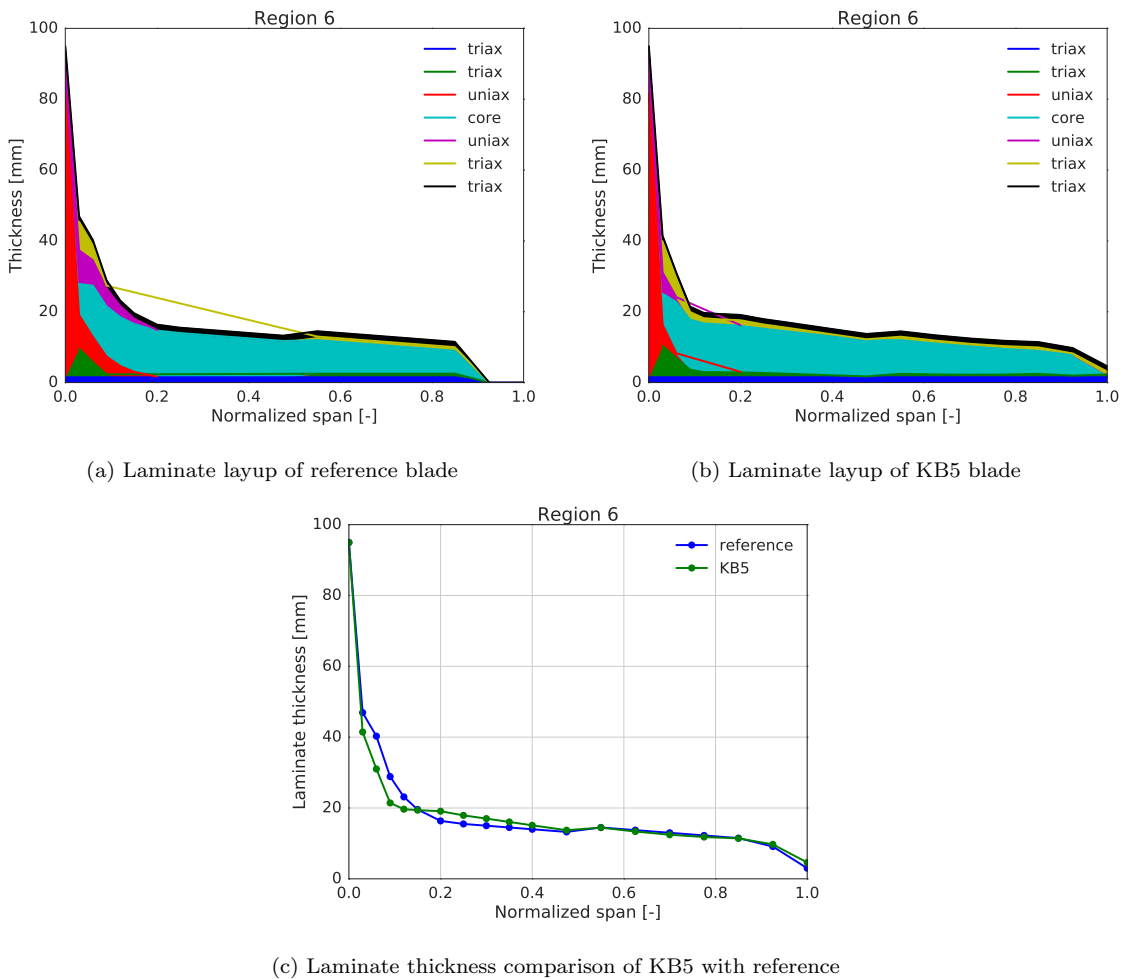


Figure 1.33: Material in the leading region (immediately in front of the spar cap)

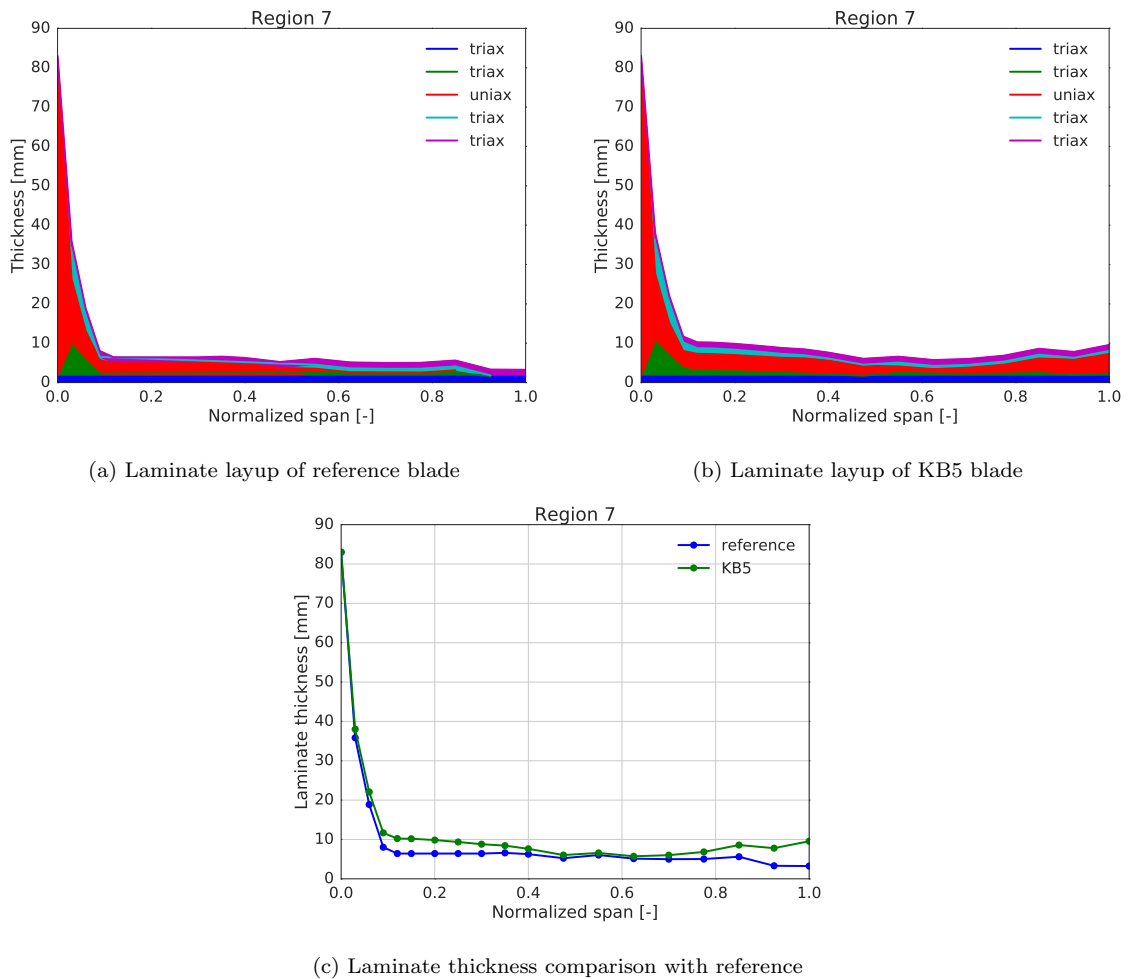


Figure 1.34: Material in the leading edge reinforcement

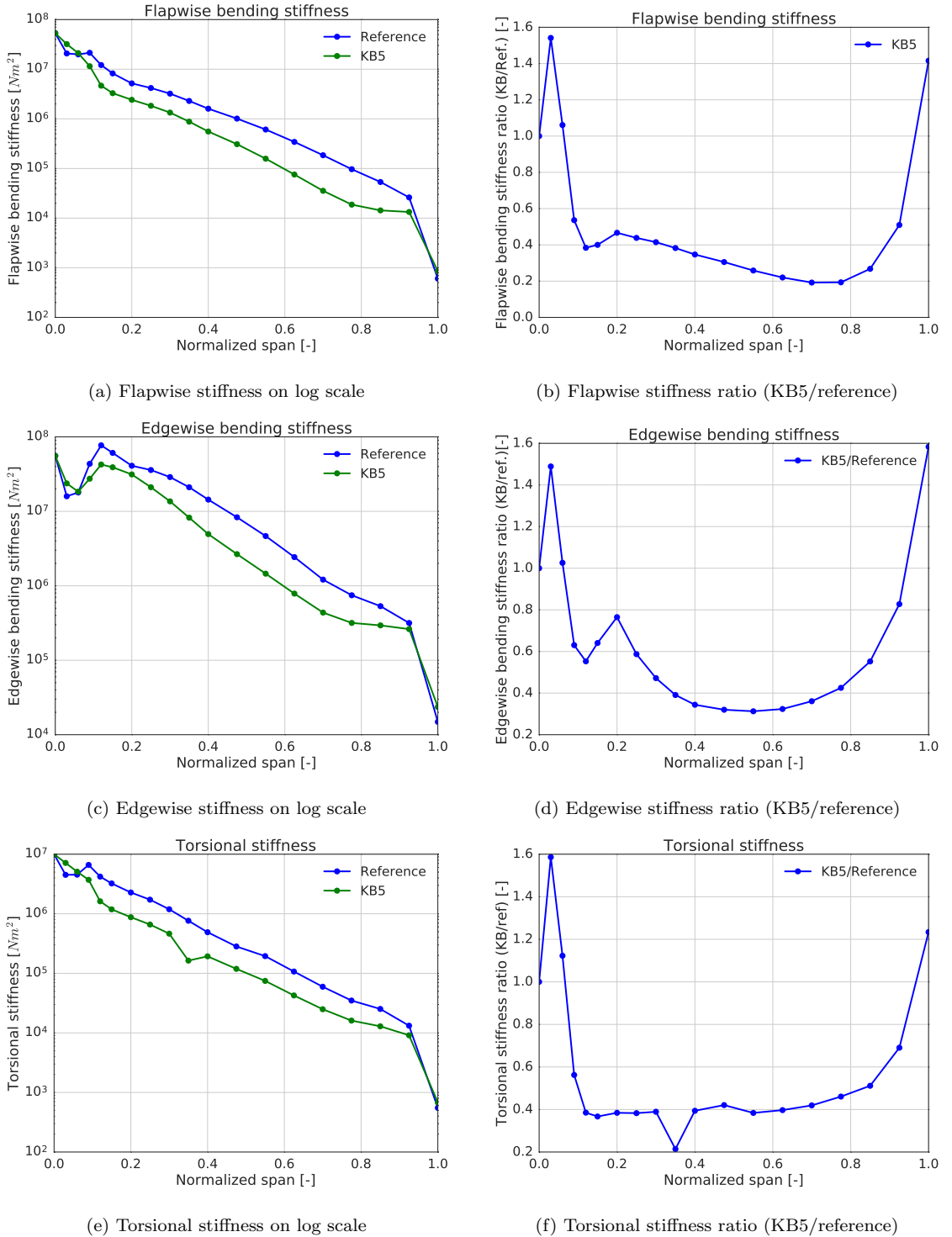


Figure 1.35: Stiffness comparisons with reference.

between 8 and 9 m/s where the rated rotor speed of 70 rpm is attained. This is shown in Figure 1.36c. Beyond this point and until it attains the rated power at a wind speed of 10 m/s, the power coefficient decreases as a result of decreasing tip-speed ratio with rising wind speed. Whereas the reference rotor has an optimal constant power coefficient of 0.46 which is maintained until it attains the rated rotor speed of 70 rpm at a wind speed of 10 m/s. Figure 1.36d shows the thrust coefficient over the operational wind speed range of the turbine. The thrust coefficient for KB5 is higher than that for the reference rotor, and it decreases with rising wind speed in the variable speed region. This is a result of the blade increasingly twisting towards the feather with rising wind speed due to the bend-twist coupling effect as a consequence of the backward sweep in the blade. Due to the backward sweep, a larger flapwise force will generate greater torsional moments resulting in increased torsion towards feather. The decrease in the thrust coefficient is even greater beyond the 8 - 9 m/s wind speed range, during which the KB5 rotor attains rated rotor speed. This decrease is due to the reduction in loading as a result of decreasing tip-speed ratio additionally contributing to the load reduction being offered by the geometric bend-twist coupling. Such passive load alleviation mechanisms allow for a larger rotor that can produce more power for a considerably low increase of the aerodynamic loads over those produced by the reference rotor. Furthermore, the peak loading is similar to that of the reference rotor.

The steady state load response of the KB5 and reference rotors are shown in Figure 1.37. The flapwise blade root bending moment is increased in KB5 compared to the reference rotor, primarily due to the 5.5% increase in the blade length. This can be observed in Figure 1.37a. The edgewise blade root bending moment is shown in Figure 1.37b. It is seen to be slightly lower than the reference rotor. Edgewise moments are mainly driven by the mass of the blade and the reductions can be attributed to the 4.65% lower blade mass of the KB5 rotor than the reference. The torsional moments shown in Figure 1.37c, are seen to increase in absolute magnitude, with rising wind speeds in the variable speed region of the KB5 rotor. This is due to the backward sweep of the blade that generates additional torsional moment due to the action of the flapwise forces, which increase with rising wind speeds. The negative sign of the torsional moments indicate that the moments are directed in twisting the blade towards the feather. Thus, for rising wind speeds, the increasing flapwise force makes the blade twist increasingly towards the feather. Beyond the point at which the rated rotor speed is attained for the KB5 rotor, the decreasing tip-speed ratio slightly reduces the flapwise forces thus relatively reducing the magnitude of the torsional moment until 10 m/s at which rated power is achieved. Beyond this point the same phenomenon is repeated, but is mainly driven by reduction in the tip-speed ratio caused by pitching of the blades.

The steady state physical response of the structure is shown in Figure 1.38. Figure 1.38a shows the steady state torsional response of the rotor at a wind speed of 9 m/s. The KB5 blade is seen to torsion towards the feather with the absolute magnitude increasing with the normalized span. The increase in torsion corresponds to the increase in the amount of backward sweep along the span, as seen in Figure 1.29a. The spanwise blade torsion with increasing wind speeds in the variable speed region is shown in Figure 1.38b. It is seen that the blade twists increasingly towards the feather for increasing wind speeds, until 85% blade span. For the last 15% of the KB5 blade span the blade twists increasingly towards stall with rising wind speeds. The flapwise positions of the blade sections are shown in Figure 1.38c at a wind speed of 9 m/s. The KB5 blade is seen to bend towards the tower with its magnitude increasing along the span until approximately 80% of the blade length. At this point the blade attains a position closest to the tower. Beyond this point the blade is seen to deflect away from the tower relative to its closest position, until the tip. Figure 1.38d shows the flapwise positions of the blade for different wind speeds in the variable speed region of the KB5 rotor. The blade increasingly deflects towards the tower with rising wind speeds, due to increasing flapwise bending moments as seen in Figure 1.37a. The flapwise bending moment moment is seen to attain its highest value at a wind speed of 9 m/s corresponding to the resulting flapwise blade positions.

The angles of attack along the span for different wind speeds in the variable speed region of the KB5 rotor is seen in Figure 1.39. The angles of attack are seen to decrease with rising wind speeds until the wind speed of 8 m/s. The KB5 rotor attains its rotor speed between a wind speed of 8 m/s and 9 m/s, marking the end of the variable speed region. At a wind speed of 9m/s the angles of attack are seen to attain a higher value than the rest of the wind speeds.

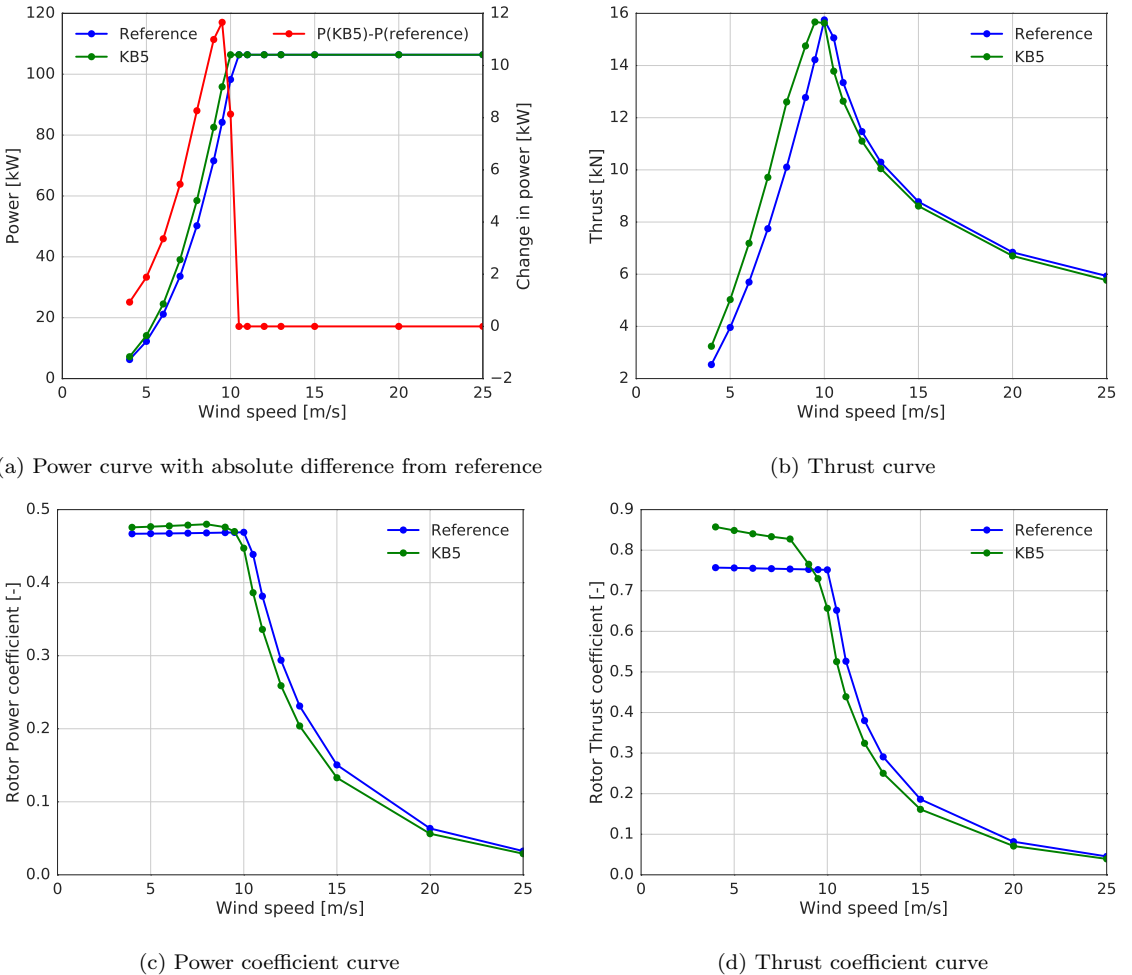


Figure 1.36: Steady state power and thrust curves

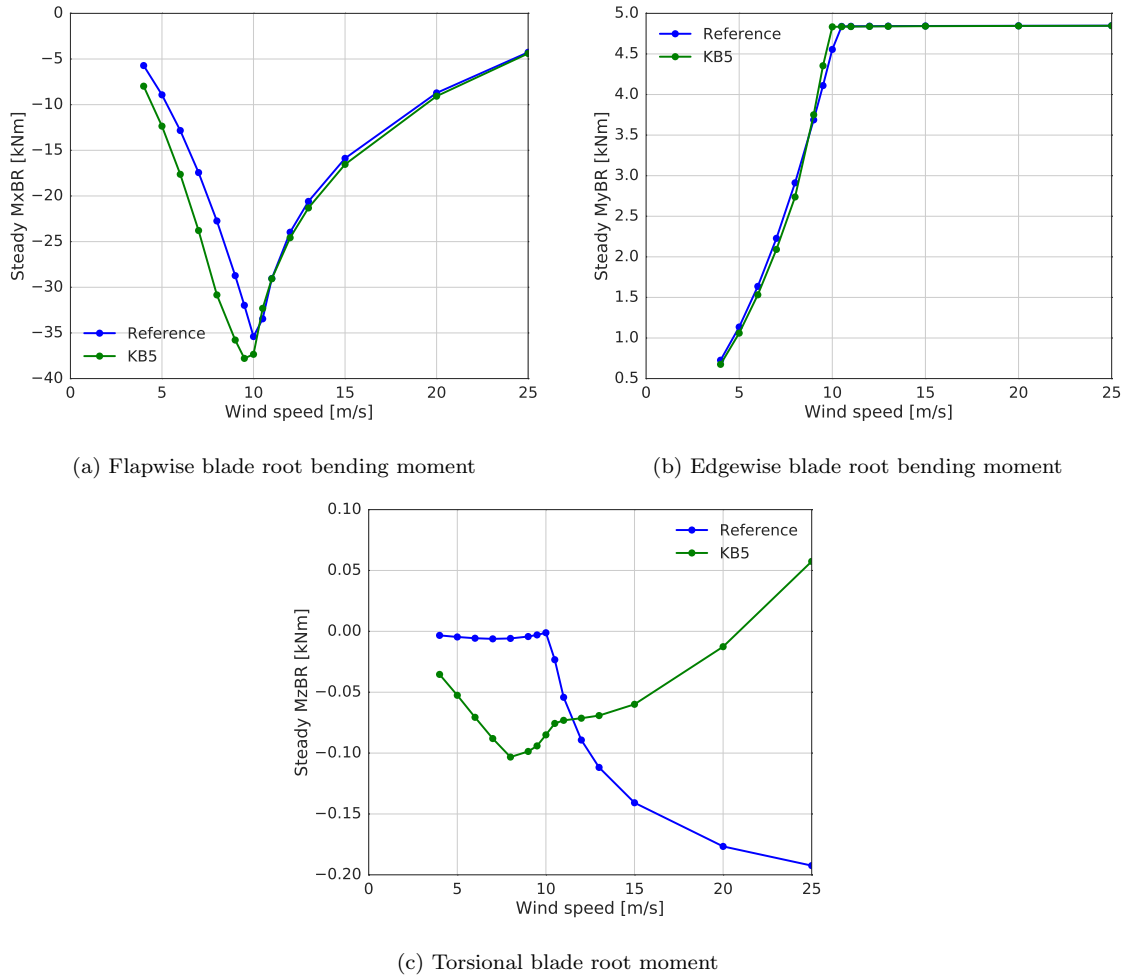


Figure 1.37: Steady state load response

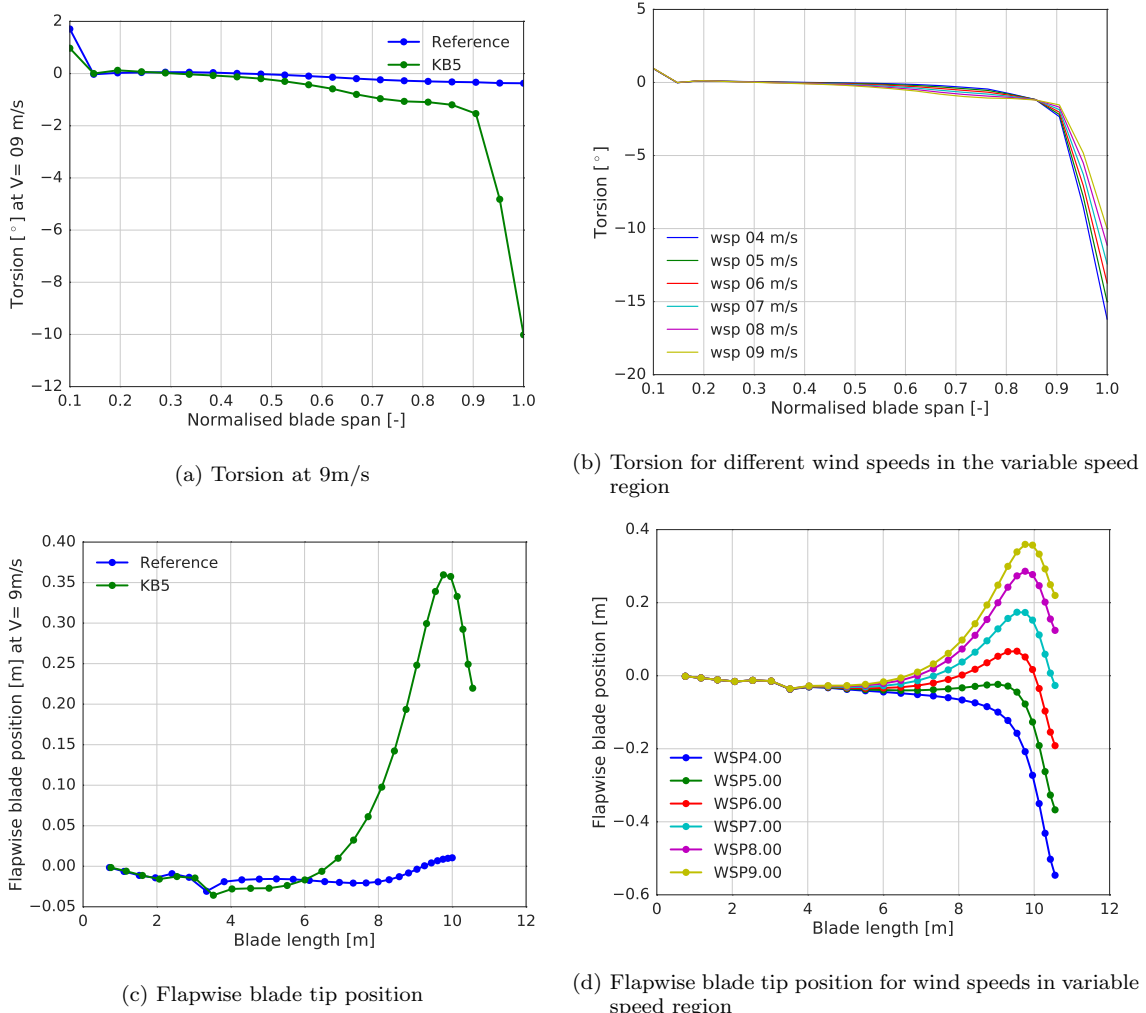


Figure 1.38: Steady state blade response

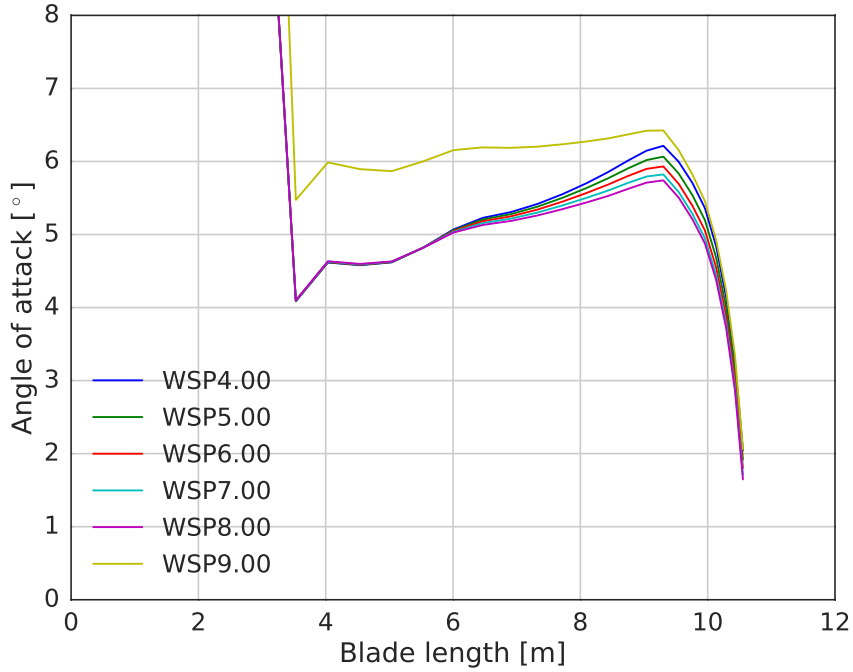


Figure 1.39: Steady state angles of attack along the blade span for wind speeds in variable speed region

## 1.7 Conclusion

The reference 100 kW rotor has been optimized using the multi-disciplinary optimization tool HawtOpt2. Five different optimized blades were obtained through placing varying constraints in the problem formulation. KB1 was optimized as a straight blade with no coupling. KB2 was optimized as a geometrically coupled blade through the introduction of backward sweep. KB3 was optimized as a material coupled blade through altering the fibre layup angles in the spar cap uniax laminates. Based on an analysis of the obtained optimized designs it was decided to select backward sweep as the means to introduce bend-twist coupling. This was influenced by the superior power output and annual energy production of the KB2 swept design over the KB3 material coupled design. Additional constraints on the maximum achievable backward sweep and prebend were placed on the design to facilitate manufacturability.

The optimized designs showed significant improvements in the annual energy production over the reference turbine. The coupled designs provided a greater improvement than the non-coupled design due to the passive load reduction afforded by bend-twist coupling. This allowed for the optimized blades to be more slender, flexible, longer and at the same time have a lower mass than the reference blade. The optimized rotor further curtailed peak loads by attaining the rated rotor speed at an earlier wind speed than the rated power. Providing design freedom to the tip-speed ratio and in extension to the rotor speed also aided in improving the annual energy production.

## 2 Static analysis

A static analysis of the KB5 optimized blade is carried out. In Section 2.1 the blade tip is loaded with a flapwise force and the structural deflections are recorded. This is repeated with an edgewise force of the same magnitude. Section ?? presents the natural frequencies of the first five modes of the KB5 optimized blade.

### 2.1 Load test

The structural response of the finalized blade design KB5 under the action of a static flapwise force at the blade tip is presented. The analysis is carried out in the time domain aero-servo-elastic tool HAWC2.

**Note on the coordinate system:** A coordinate system is fixed at the root of the blade with the negative z-axis running from root to tip, the x-axis (blade edgewise) is out of the plane and y-axis (blade flapwise) from right to left. In this coordinate system, the blade root can be considered as being fixed to an imaginary ground with the blade tip pointing skywards. Thus, a twist towards feather would be positive and towards stall would be negative.

A flapwise force of 10 kN is applied at the blade tip in the positive y-direction. This is followed by the application of an edgewise force of the same magnitude in the positive x-direction. The initial states, final states and resulting deflections for the reference rotor and the KB5 optimized blades are shown in Table 2.1 and Table 2.2 for the flapwise and edgewise loads respectively. The unloaded positional values of the tip in the y-direction and x- direction represents the prebend and the sweep respectively. While the unloaded twist value represents the pre-twist of the blade section at the tip. The KB5 blade is seen to deflect more than the reference blade both in the flapwise as well as the edgewise directions owing to a reduction in the stiffnesses, as shown in Section 1.6. The torsional deflection in KB5 is also much higher than in the reference blade with the blade twisting towards feather. The high deflection is attributed to the combined effect of reduced torsional deflection compared to the reference, and the presence of bend-twist coupling towards feather due to the backward sweep.

Table 2.1: Structural response of reference and KB5 blades under the action of a flapwise static tip load

Quantity	Reference			KB5		
	Unloaded	Loaded	Deflection	Unloaded	Loaded	Deflection
tip - y (flapwise) [m]	-0.27	2.50	+2.77	-0.98	5.41	+6.39
tip - x (edgewise) [m]	-0.01	0.17	+0.18	-0.50	-0.24	+0.26
Twist [deg]	-0.87	-4.67	-3.8	-9.60	23.88	+33.48

Table 2.2: Structural response of reference and KB5 blades under the action of a edgewise static tip load

Quantity	Reference			KB5		
	Unloaded	Loaded	Deflection	Unloaded	Loaded	Deflection
tip - y (flapwise) [m]	-0.27	2.50	+2.77	-0.98	5.41	+6.39
tip - x (edgewise) [m]	-0.01	0.17	+0.18	-0.50	-0.24	+0.26
Twist [deg]	-0.87	-4.67	-3.8	-9.60	23.88	+33.48

### 2.2 Eigen analysis

## 3 Analysis of the Design Load Basis

### 3.1 Introduction

The design load basis (DLB) considered for this report is based on the IEC 61400-1 standard. A more elaborate discussion and interpretation of that standard is given in [? ]. The aeroelastic code used for these investigations is HAWC2 [? ].

The following rotor configurations have been considered:

- reference (referred to as baseline or baseline100kw in the figures)
- KB5

The statistics are included in section 4.1 as tables, and as plots in section 5.1. The plots show the minima, mean, maxima and standard deviations for all of the simulations considered within the given design load case. The tables give the minima of the minima, and the maxima of the maxima for each DLC and channel. For a more elaborate description of the considered design load basis the reader is referred to [? ]. The considered design load cases (DLC's) for this report are the following: DLC's 1.2, 2.4, 3.1, 4.1, and 6.4.

This report does not include selected time series plots of the design load basis analysis, although some of the conclusions presented within the the discussion section (see section 3.4) are based on the analysis of individual time series.

Appendix 5.1 include the comparison between the reference rotor and KB5. The following channels are considered:

- Electrical power [W], excluding losses.
- Rotor speed [rpm]
- Blade 1, 2 and 3 pitch angles [deg]
- Controller status flag [0-6], 0: normal operation, 1: shut down due to over speed
- Tower base for-aft bending moment [kNm]
- Tower base side-side bending moment [kNm]
- Yawing moment tower top [kNm]
- Shaft torsion moment [kNm]
- Blade root 1, 2 and 3 flap-wise bending moments [kNm] (pitching coordinates)
- Blade root 1, 2 and 3 edge-wise bending moments [kNm] (pitching coordinates)
- Blade root 1, 2 and 3 torsion bending moments [kNm] (pitching coordinates)
- Minimum tower to blade tip distance [m] (consider only the minima)

To accommodate the comparison the figures include two different rotors, but the wind speed or wind direction is slightly off-set from the actual value. For example, for each wind speed of 10 m/s, case 1 is plotted at a value slightly below 10 m/s, and case 2 at a value slightly above. Both cases have been run at the same wind speed of 10 m/s.

### **3.2 Stiff Tower**

The tower stiffness was first estimated based on a quantitative description and drawings provided by the turbine manufacturer. However, the stiffness and mass properties of the derived structural model ended up being very close to the 3P frequency at rated wind speed and above. This resulted in a sharp increase in tower side-side, blade-edge and shaft torsional loads. Considering that this platform has been produced and is being operated in the field, it is assumed that tower model initially derived from the given data was not sufficiently accurate. Until more detailed structural data becomes available, the tower is considered to be stiff. Once a sufficiently accurate description of the tower is known a flexible tower model can be introduced to re-assess the design load basis. Depending on the eigenfrequencies and damping of the tower, the introduction of tower flexibility is expected to affect the results.

### **3.3 Controller Tuning**

For this study the basic DTU Wind Energy controller is used [? ]. The controller is tuned based on the reference rotor using the pole placement technique as implemented for a 1 DOF model in HAWCStab2.

The controller tuning settings are assumed to be fixed for both the baseline and KB5 rotor since the controller tuning will not modifiable for the prototype with KB5 blades. Note that the design procedure did not include any additional constraints to mitigate the effects of a fixed controller tuning setup. Under normal circumstances, a re-designed rotor requires different controller tuning parameters compared to the reference case. The effect of not re-tuning the controller for KB5 is not considered within the scope of this report.

In addition to the considered design load cases, one extra load case is included: normal operating conditions with wind shear and tower shadow, but without any turbulence. Additionally, a 1 m/s wind step is added to the wind speed towards the end of the simulation. The purpose of this load case is to asses steady power curve performance. This test case is labelled as "test\_steadysteps".

### **3.4 Discussion and Conclusion**

The cases without turbulence (see section 5.1.1 show that there is indeed an increased power output for KB6 in below rated conditions while at the same time the loads are either similar or reduced compared to the baseline rotor. This trend is also visible for the other load cases (see sections 5.1.2-5.1.6). There is one outlier for KB6 that results in an increased tower base for-aft bending moment in DLC1.2 (see figure 5.17). The cause of this could be due to the sub-optimal controller tuning of KB5, but a more detailed follow-up investigation is required before a final conclusion can be rendered. Further, a load increase can be observed for the blade root torsional bending moment. This increase is a consequence of the swept blade geometry.

### **3.5 Future Work**

Considering that KB5 (or a rotor similar to KB5) is forecasted to be build and operated as a prototype, the following points are suggested for further analysis:

- Include time series analysis of certain indicative results.
- Determine an accurate model for the tower (eigenfrequencies, structural damping).
- Determine controller tuning parameters from the turbine platform.
- Sensitivity study regarding controller tuning parameters to account for the uncertainty caused by the unknown actual controller tuning parameters of the platform.
- Tabulated results showing the differences in load statistics.
- Tabulated extreme loads observed within each of the DLB's.
- Brake down of fatigue loads, and life time fatigue loads.

## 4 Design Load Basis Statistic Tables

### 4.1 Reference vs KB5

Table 4.1: Blades 1,2,3 root torsion moment [kNm]

	baseline	KB5		
DLC	max of max	min of min	max of max	min of min
dlc12_iec61400-1ed3	0.628669	-0.662794	1.6108	-0.6864
dlc24_iec61400-1ed3	0.813648	-0.681443	1.45	-0.654118
dlc31_iec61400-1ed3	0.0920486	-0.240909	0.191699	-0.0842973
dlc41_iec61400-1ed3	0.472522	-0.571366	0.422211	-0.572294
dlc64_iec61400-1ed3	1.30718	-0.959426	3.28982	-3.22197
No turbulence	4.21674	-3.46674	5.46346	-4.25006

Table 4.2: Blades 1,2,3 root flap bending moment [kNm]

	baseline	KB5		
DLC	max of max	min of min	max of max	min of min
dlc12_iec61400-1ed3	56.0374	-65.6522	38.8565	-62.5098
dlc24_iec61400-1ed3	64.9552	-62.0349	43.1082	-58.4736
dlc31_iec61400-1ed3	2.36137	-25.7876	-0.388214	-25.4932
dlc41_iec61400-1ed3	11.4245	-25.7876	8.20715	-25.4932
dlc64_iec61400-1ed3	88.2928	-74.6774	58.6416	-62.5334
No turbulence	68.5456	-82.7075	61.8267	-78.7645

Table 4.3: Rotor speed [RPM]

	baseline	KB5		
DLC	max of max	min of min	max of max	min of min
dlc12_iec61400-1ed3	88.7248	23.0137	96.9661	22.7157
dlc24_iec61400-1ed3	87.0058	23.0091	89.6173	22.6359
dlc31_iec61400-1ed3	70.257	26.4441	70.2166	27.1068
dlc41_iec61400-1ed3	70.2896	-0.250407	70.2294	0.100884
dlc64_iec61400-1ed3	95.3485	23.451	104.802	23.5627
No turbulence	124.681	26.5141	126.424	27.197

Table 4.4: Electrical power [kW]

	baseline	KB5		
DLC	max of max	min of min	max of max	min of min
dlc12_iec61400-1ed3	107886	-0.852399	108597	-1.02227
dlc24_iec61400-1ed3	107795	0	107964	-1.07443
dlc31_iec61400-1ed3	106425	5924.62	106419	6381.24
dlc41_iec61400-1ed3	106465	-3.32702	106423	-3.32572
dlc64_iec61400-1ed3	108461	0	109148	0
No turbulence	106467	0	106472	0

Table 4.5: Tower base side-side bending moment [kNm]

	baseline		KB5	
DLC	max of max	min of min	max of max	min of min
dlc12_iec61400-1ed3	272.28	-282.218	208.121	-138.295
dlc24_iec61400-1ed3	316.394	-285.66	259.793	-190.315
dlc31_iec61400-1ed3	39.8954	2.6097	29.9485	2.70772
dlc41_iec61400-1ed3	41.4493	-11.7353	31.2986	-16.0444
dlc64_iec61400-1ed3	467.712	-404.63	429.421	-332.685
No turbulence	24.7061	-47.4205	106.716	-167.752

Table 4.6: Tower top torsion moment [kNm]

	baseline		KB5	
DLC	max of max	min of min	max of max	min of min
dlc12_iec61400-1ed3	82.9936	-60.9924	62.4899	-56.7286
dlc24_iec61400-1ed3	77.8042	-74.5082	62.7568	-68.8538
dlc31_iec61400-1ed3	8.27699	-1.35085	4.81366	-1.25849
dlc41_iec61400-1ed3	11.5488	-1.35084	11.12	-2.33936
dlc64_iec61400-1ed3	117.973	-82.2051	87.8688	-74.6502
No turbulence	27.4214	-8.49293	53.0883	-16.6863

Table 4.7: Blades 1,2,3 root edge bending moment [kNm]

	baseline		KB5	
DLC	max of max	min of min	max of max	min of min
dlc12_iec61400-1ed3	23.5161	-15.5169	22.3388	-15.5964
dlc24_iec61400-1ed3	24.2799	-18.2302	25.7917	-15.1538
dlc31_iec61400-1ed3	8.81261	-5.61785	8.85792	-5.97004
dlc41_iec61400-1ed3	11.7049	-5.89136	11.2253	-6.31271
dlc64_iec61400-1ed3	31.3524	-22.4788	38.7984	-35.1974
No turbulence	29.7948	-21.2912	39.2525	-22.0636

Table 4.8: Shaft torsion moment [kNm]

	baseline		KB5	
DLC	max of max	min of min	max of max	min of min
dlc12_iec61400-1ed3	0.000226292	-17.8066	0.00038764	-17.7782
dlc24_iec61400-1ed3	0.000210307	-17.6319	0.000220318	-17.7153
dlc31_iec61400-1ed3	-2.18316	-14.8217	-2.29393	-14.8209
dlc41_iec61400-1ed3	0.00185272	-14.8218	0.00185261	-14.8209
dlc64_iec61400-1ed3	0	-19.1513	0.000315043	-19.0595
No turbulence	15.24	-14.8747	15.24	-14.9119

Table 4.9: Blades 1,2,3 pitch angle [deg]

	baseline	KB5		
DLC	max of max	min of min	max of max	min of min
dlc12_iec61400-1ed3	38.2781	-1.94404	38.6518	-1.19754
dlc24_iec61400-1ed3	37.36	-1.61851	37.3165	-0.735138
dlc31_iec61400-1ed3	25.4227	-8.6191e-07	25.3839	-1.117e-06
dlc41_iec61400-1ed3	90	0	90	0
dlc64_iec61400-1ed3	46.655	-1.76366	46.9222	-0.796416
No turbulence	31.4	-5.00045	33.0998	-5.00014

Table 4.10: tower-tip clearance [m]

	baseline	KB5		
DLC	max of max	min of min	max of max	min of min
dlc12_iec61400-1ed3	6.42614	2.79713	4.55133	2.13848
dlc24_iec61400-1ed3	6.42941	2.7386	4.55091	2.28183
dlc31_iec61400-1ed3	6.37136	3.17685	4.54739	3.07144
dlc41_iec61400-1ed3	6.38416	3.14661	4.54698	2.86313
dlc64_iec61400-1ed3	6.44064	2.82344	4.55014	2.26831
No turbulence	6.46298	2.54136	4.56557	1.60751

Table 4.11: Tower base for-aft moment [kNm]

	baseline	KB5		
DLC	max of max	min of min	max of max	min of min
dlc12_iec61400-1ed3	634.954	-186.028	659.024	-198.449
dlc24_iec61400-1ed3	584.512	-169.792	531.61	-127.64
dlc31_iec61400-1ed3	284.649	38.2072	272.934	38.0747
dlc41_iec61400-1ed3	284.649	-47.4723	272.934	-49.5325
dlc64_iec61400-1ed3	665.933	-281.063	707.891	-271.631
No turbulence	1262.35	-944.55	1487.62	-1019.11

## 5 Design Load Basis Statistic Plots

### 5.1 Reference vs KB5

#### 5.1.1 No turbulence with wind step

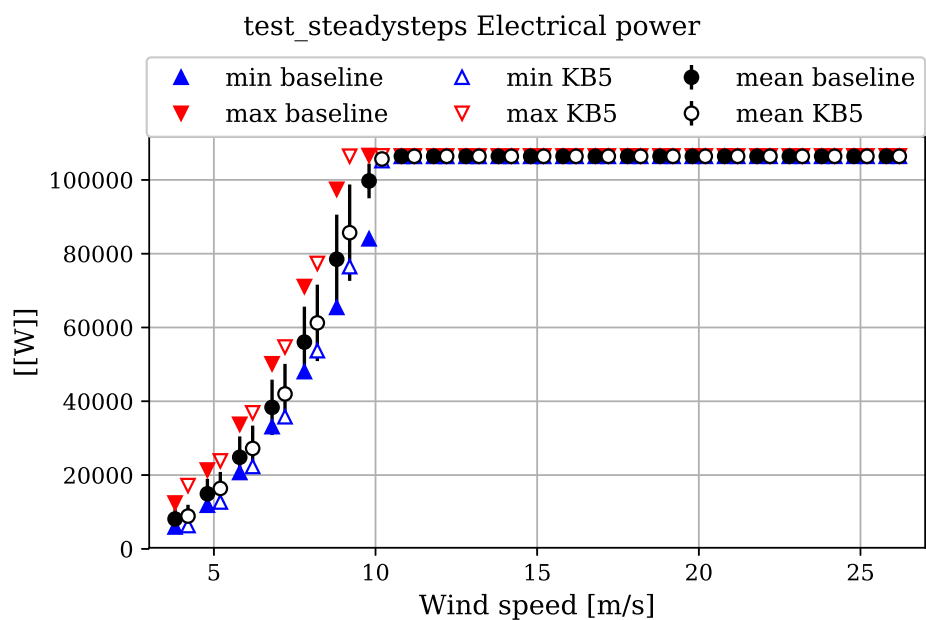


Figure 5.1: Electrical power [W], excluding losses.

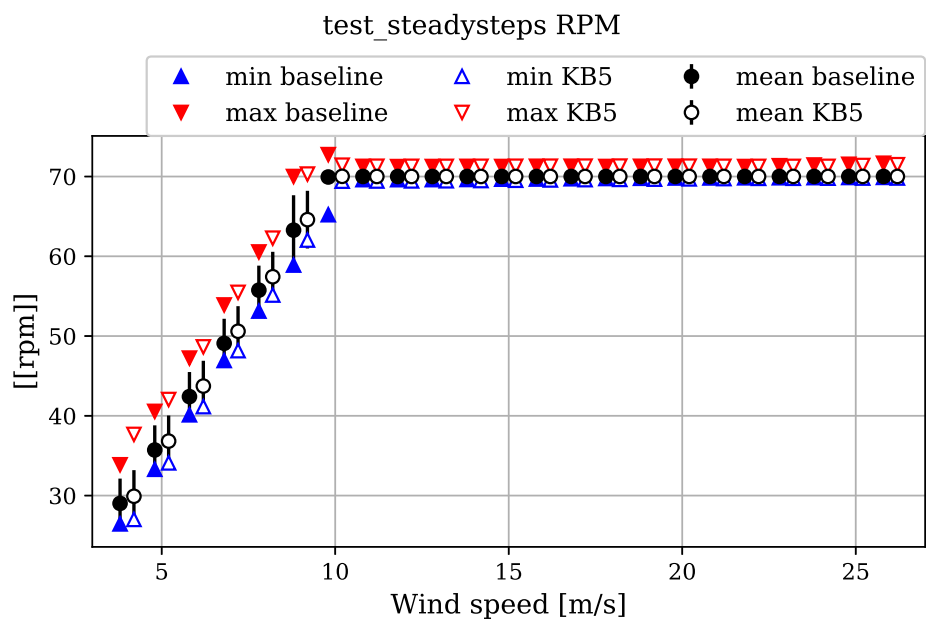


Figure 5.2: Rotor speed [RPM]

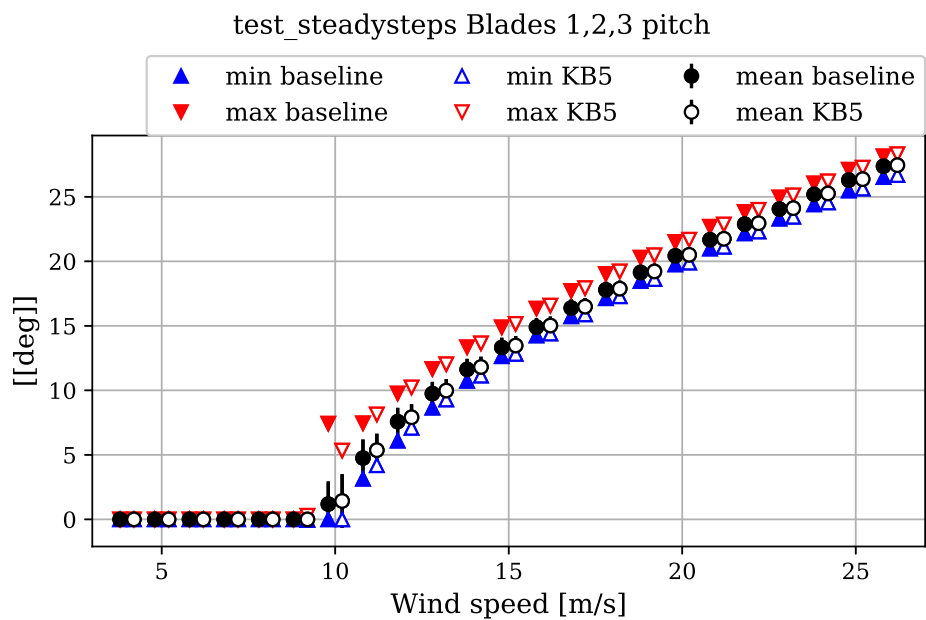


Figure 5.3: Blade 1, 2 and 3 pitch angles [deg]

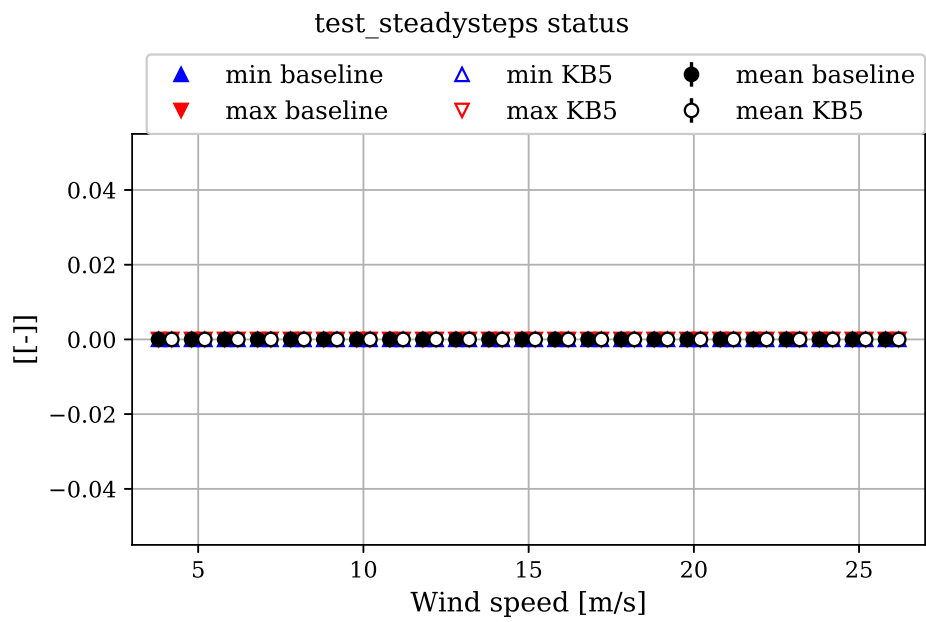


Figure 5.4: Controller status flag [0-6], 0: normal operation, 1: shut down due to overspeed

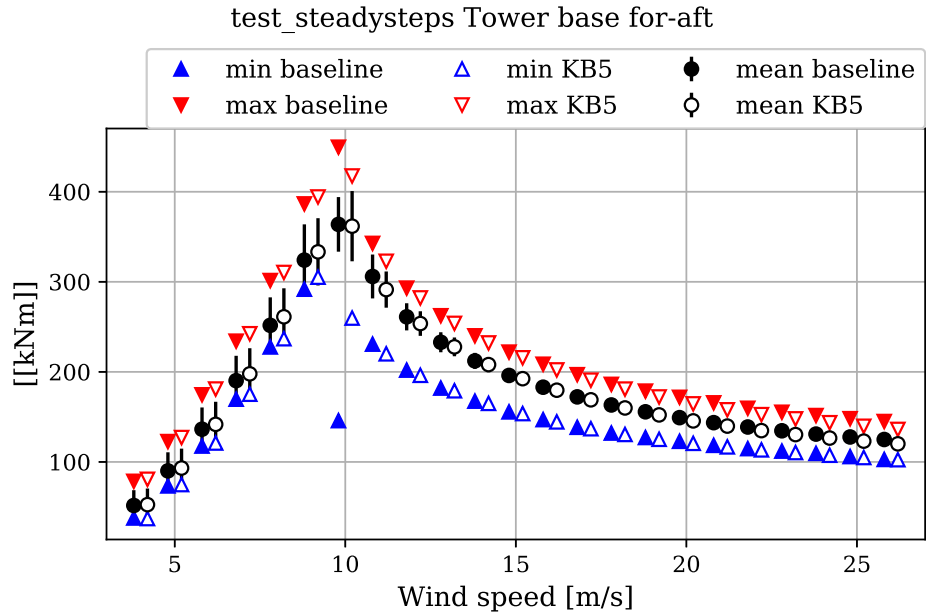


Figure 5.5: Tower base for-aft bending moment [kNm]

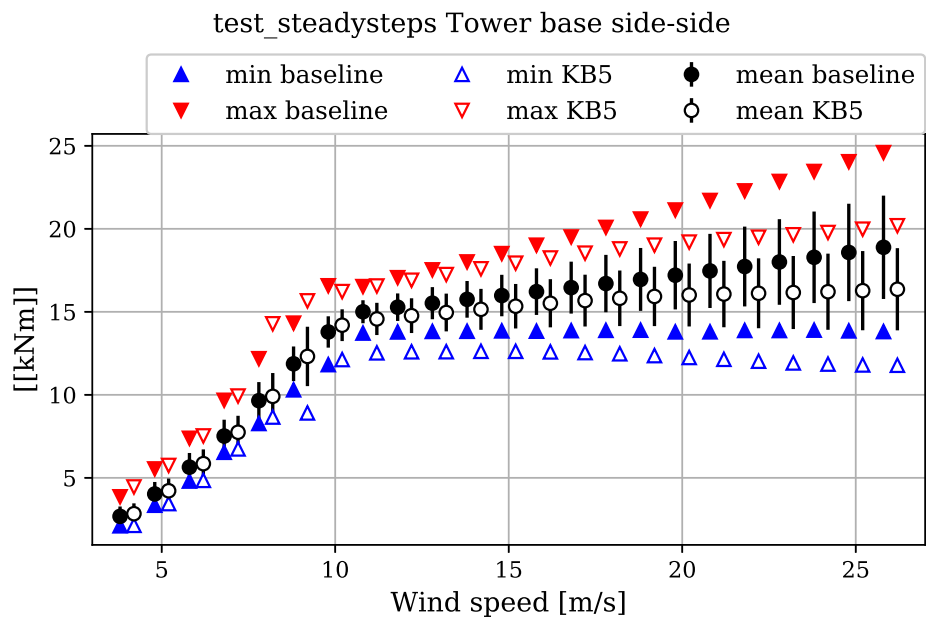


Figure 5.6: Tower base side-side bending moment [kNm]

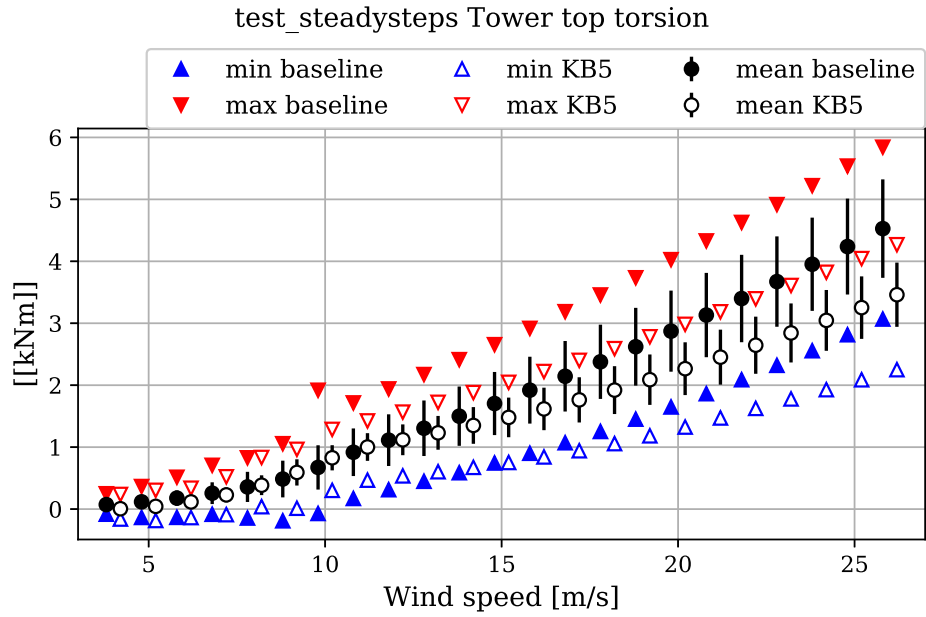


Figure 5.7: Yawing moment tower top [kNm]

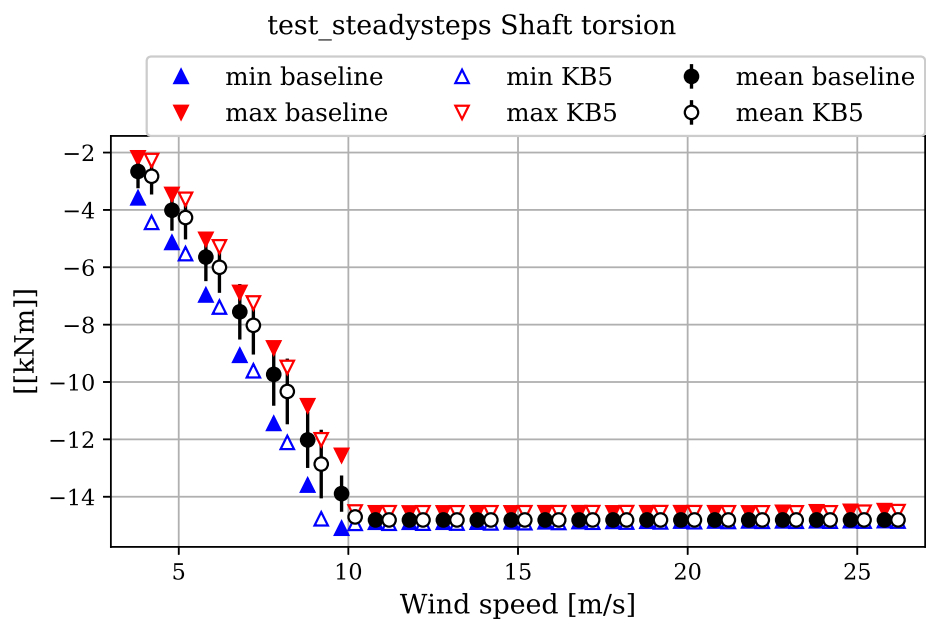


Figure 5.8: Shaft torsion moment [kNm]

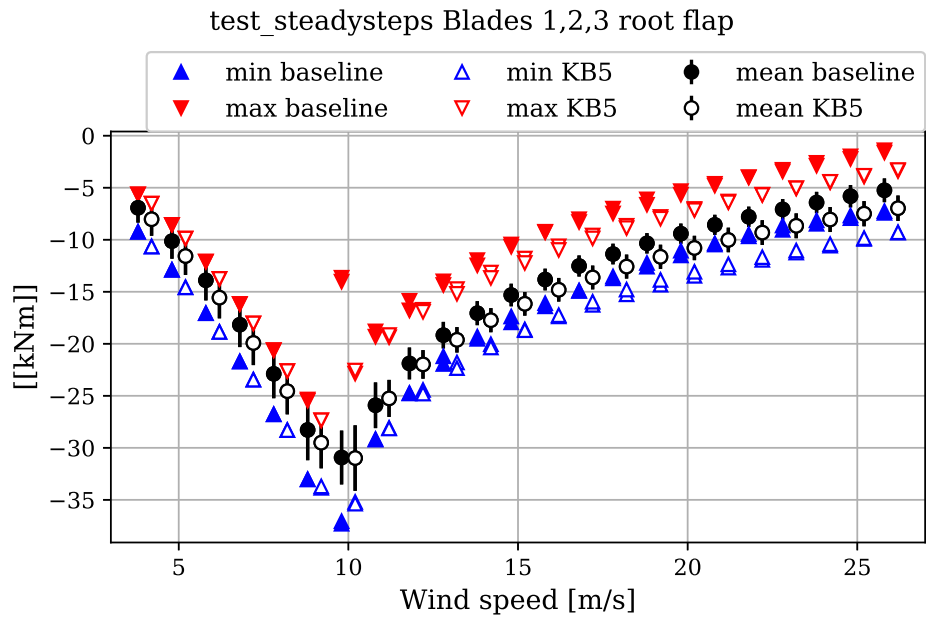


Figure 5.9: Blade root 1, 2 and 3 flap-wise bending moments [kNm] (pitching coordinates)

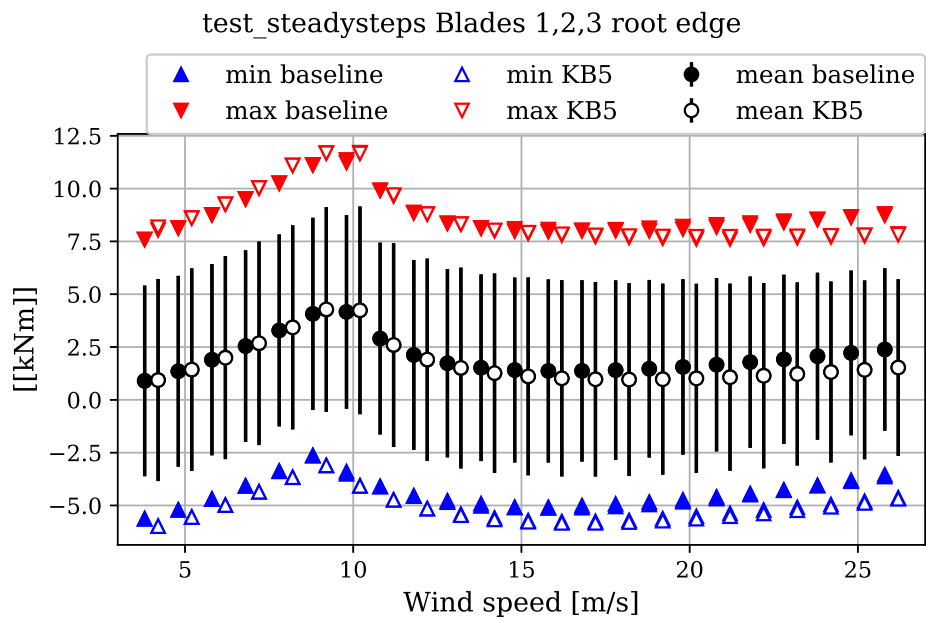


Figure 5.10: Blade root 1, 2 and 3 edge-wise bending moments [kNm] (pitching coordinates)

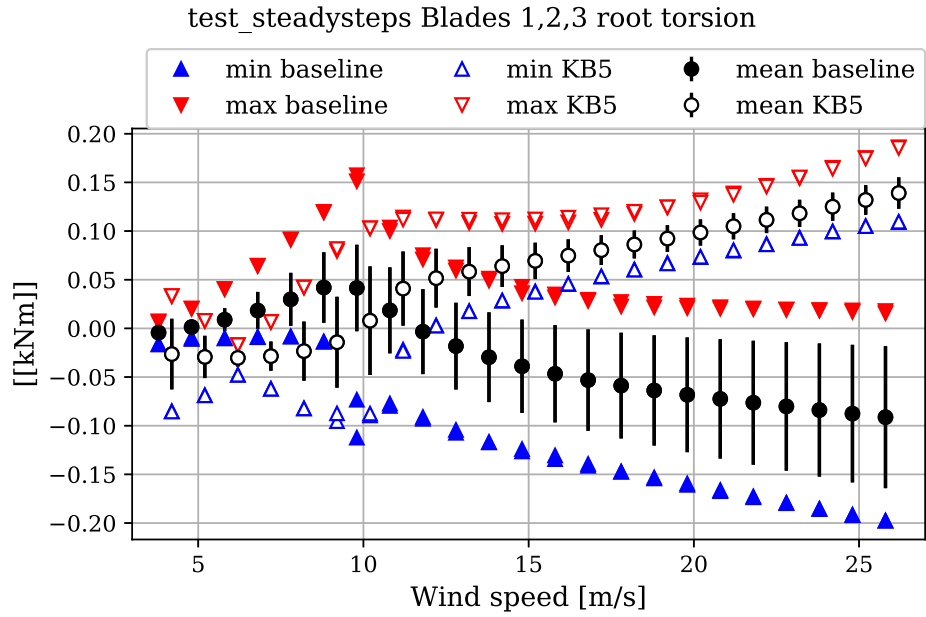


Figure 5.11: Blade root 1, 2 and 3 torsion bending moments [kNm] (pitching coordinates)

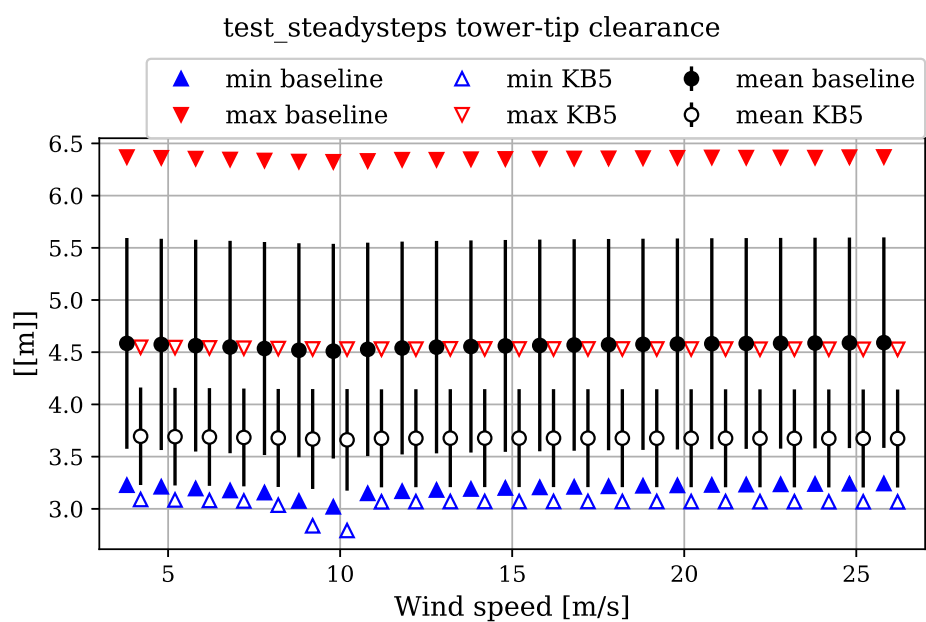


Figure 5.12: Minimum tower to blade tip distance [m] (consider only the minima)

### 5.1.2 DLC12

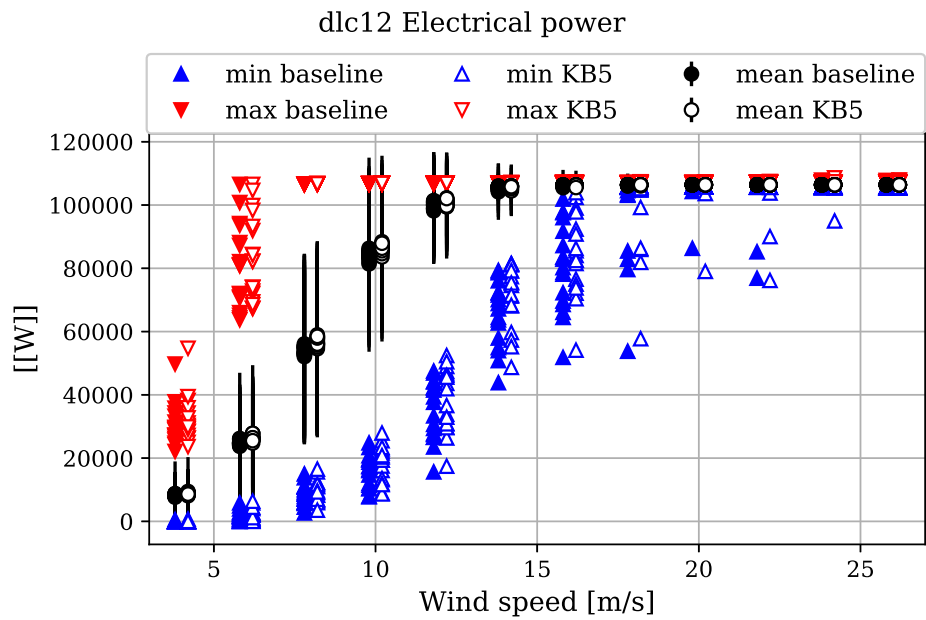


Figure 5.13: Electrical power [W], excluding losses.

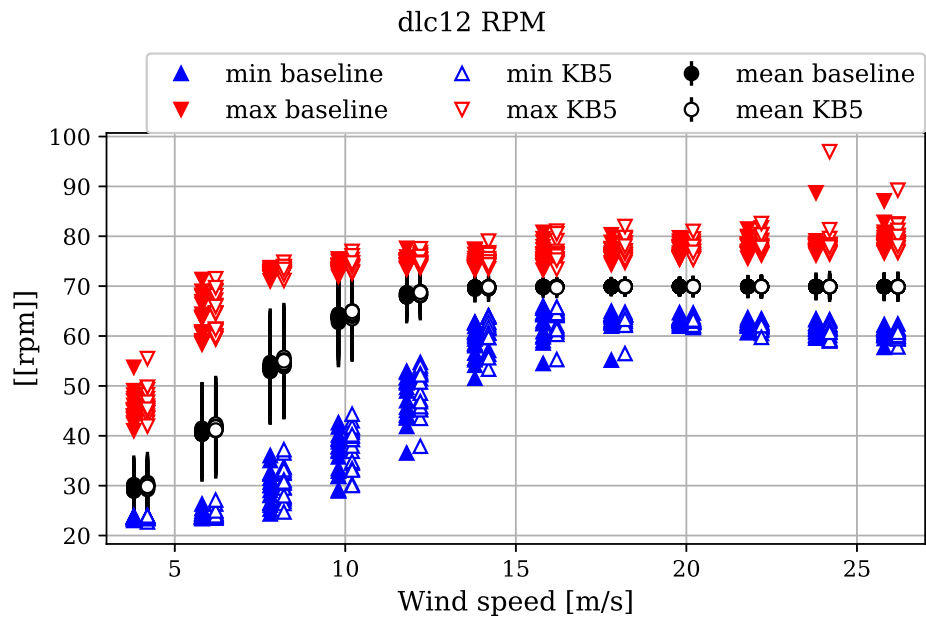


Figure 5.14: Rotor speed [RPM]

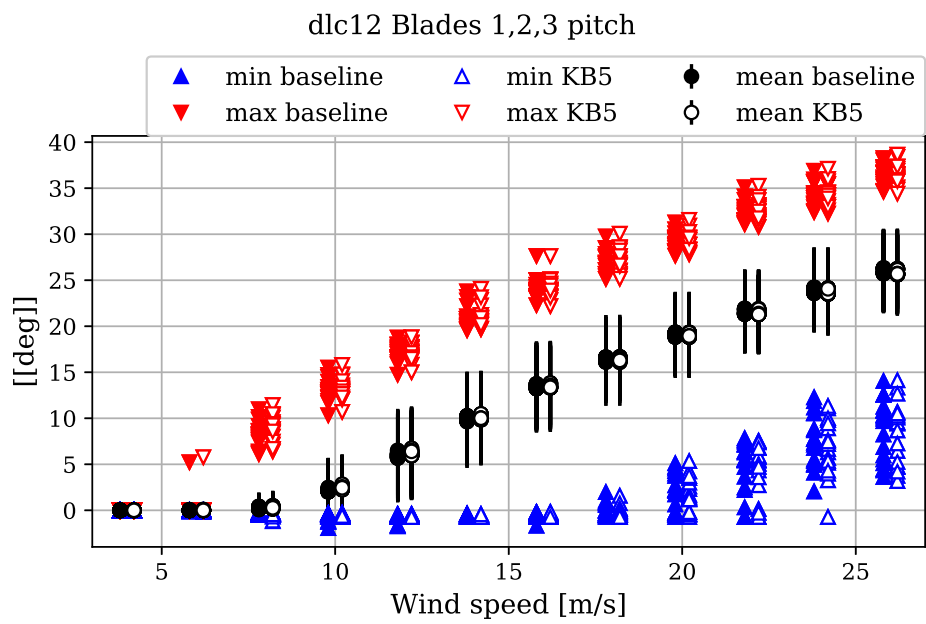


Figure 5.15: Blade 1, 2 and 3 pitch angles [deg]

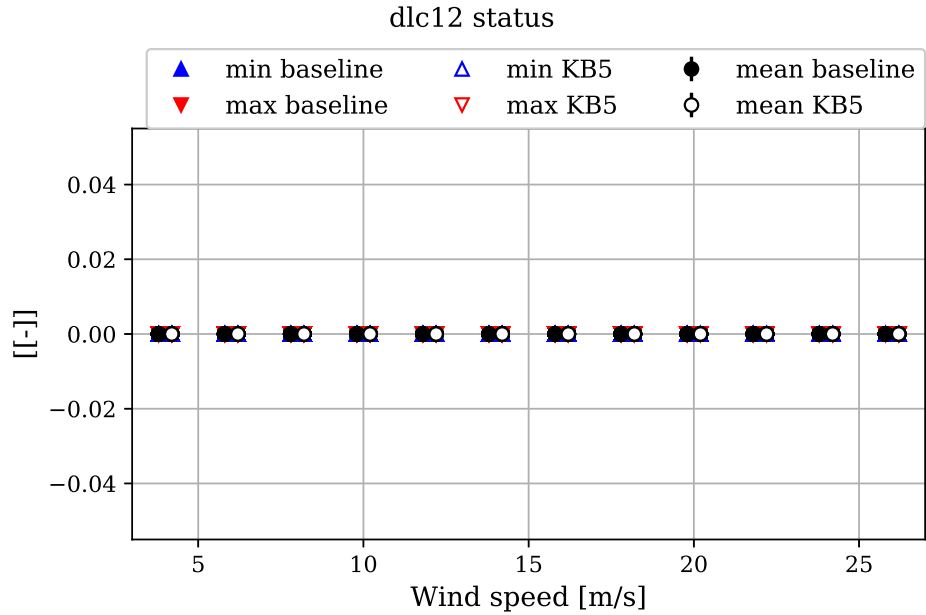


Figure 5.16: Controller status flag [0-6], 0: normal operation, 1: shut down due to overspeed

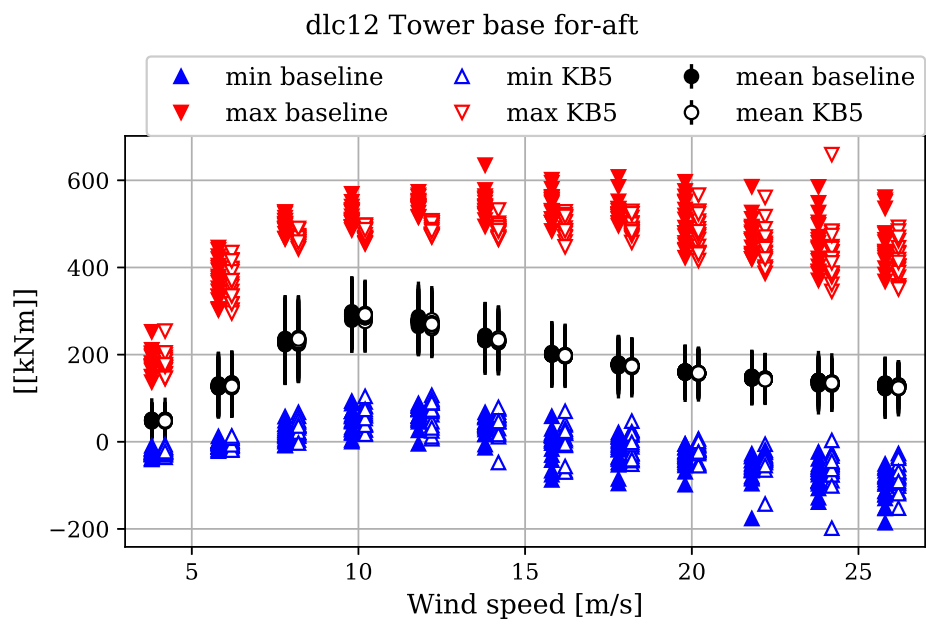


Figure 5.17: Tower base for-aft bending moment [kNm]

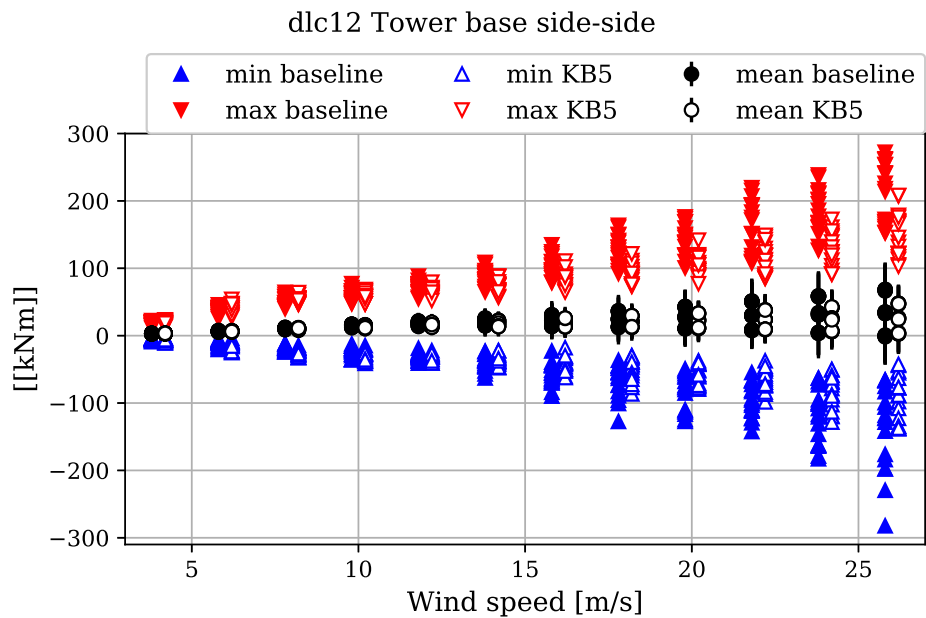


Figure 5.18: Tower base side-side bending moment [kNm]

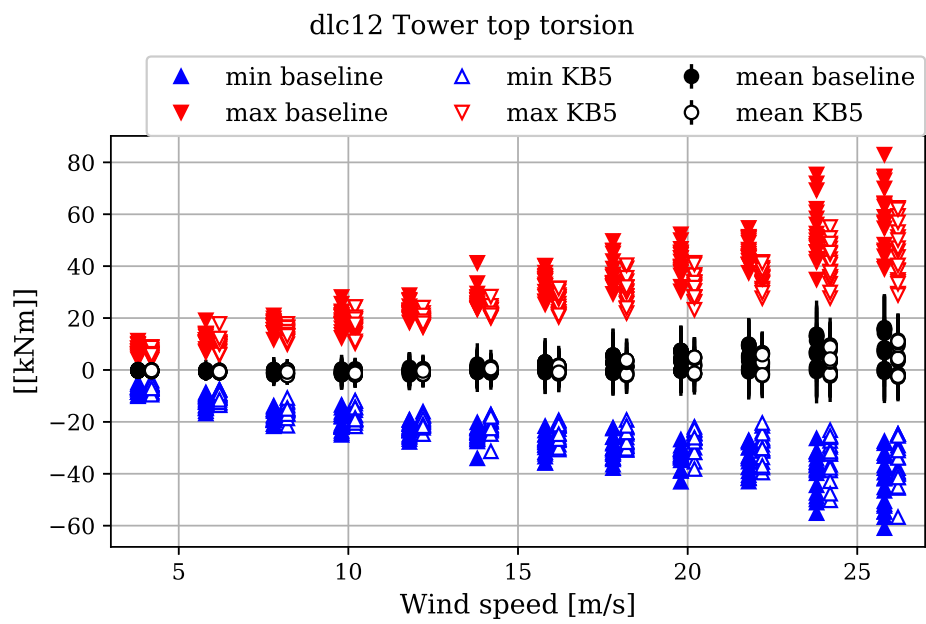


Figure 5.19: Yawing moment tower top [kNm]

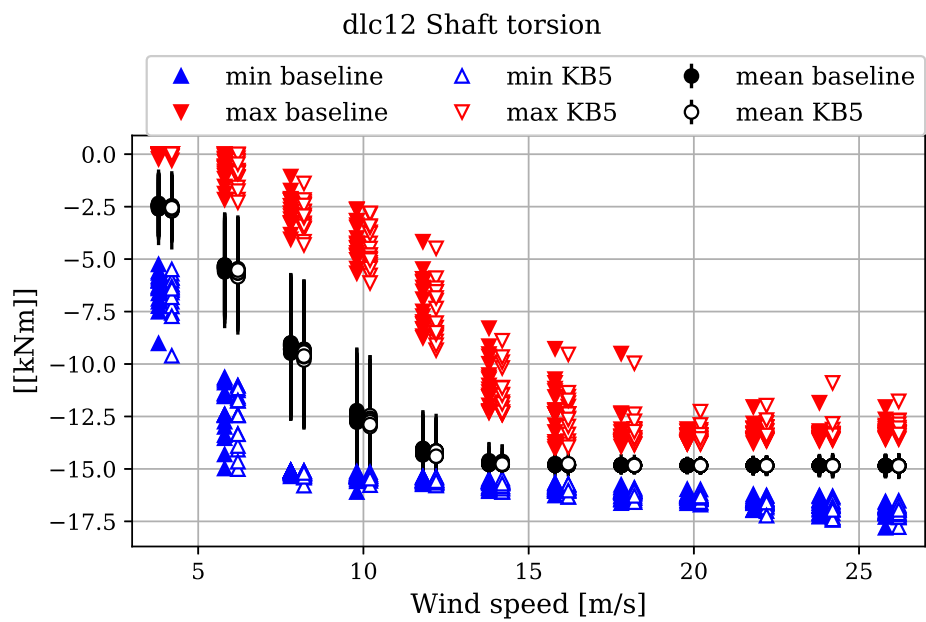


Figure 5.20: Shaft torsion moment [kNm]

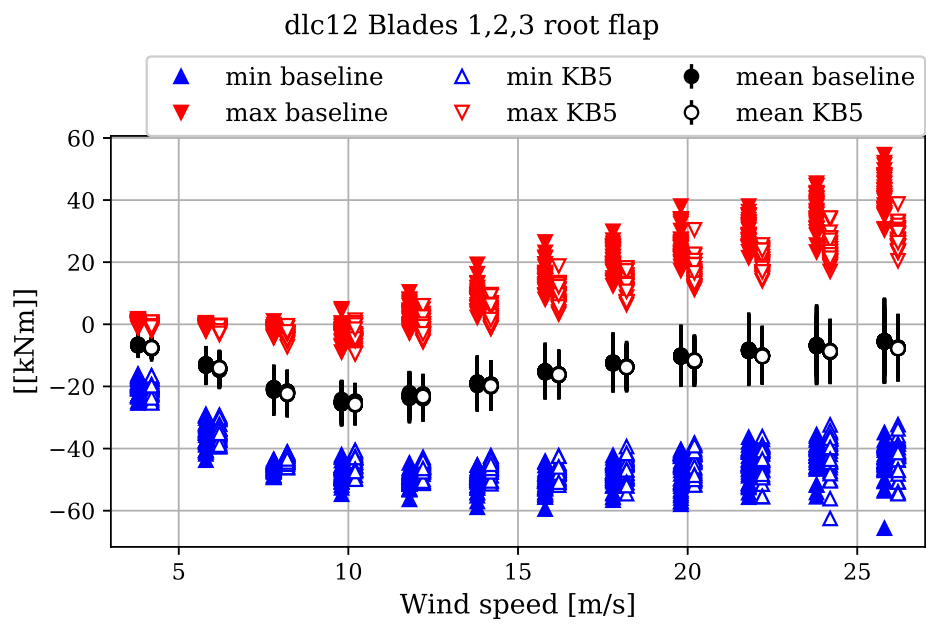


Figure 5.21: Blade root 1, 2 and 3 flap-wise bending moments [kNm] (pitching coordinates)

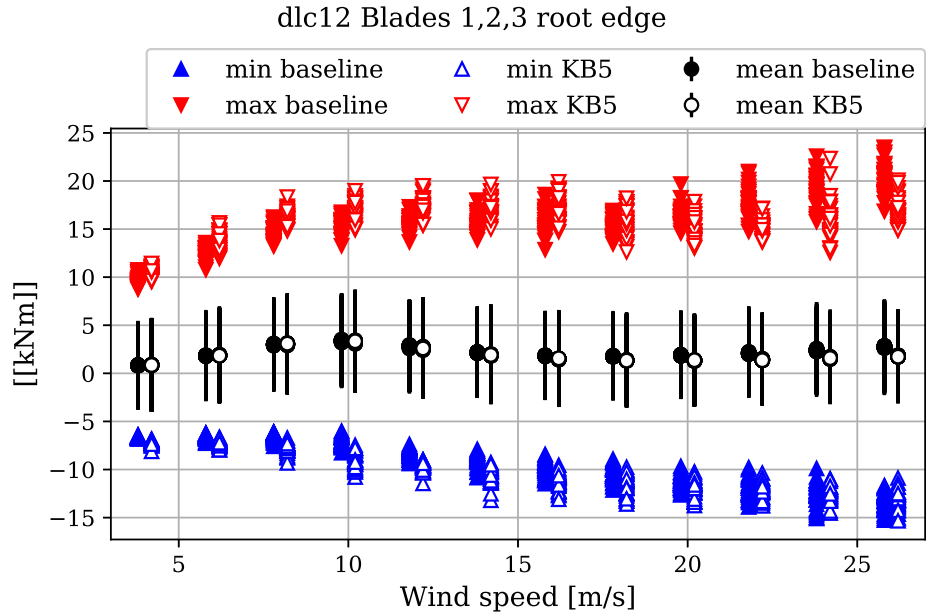


Figure 5.22: Blade root 1, 2 and 3 edge-wise bending moments [kNm] (pitching coordinates)

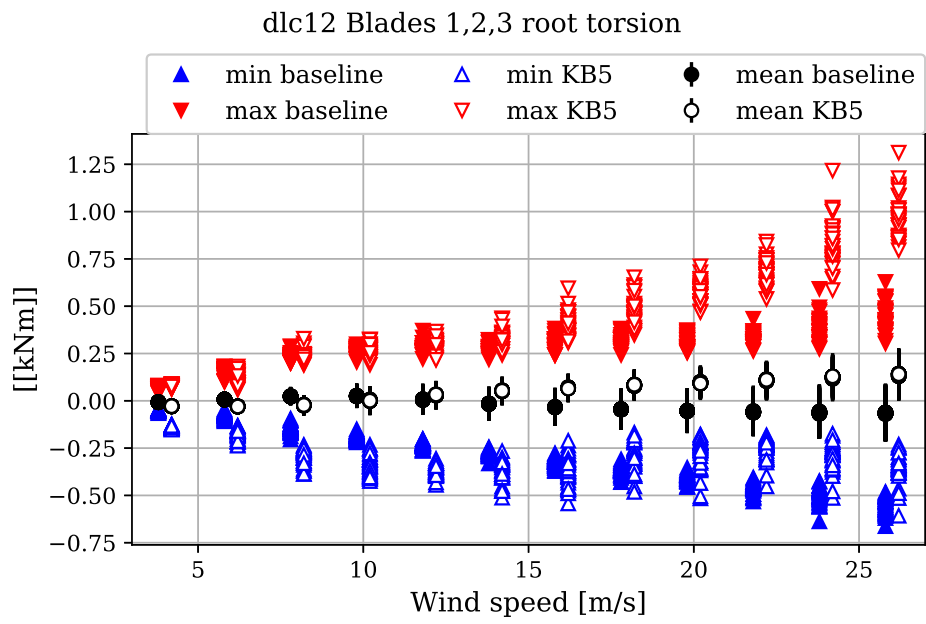


Figure 5.23: Blade root 1, 2 and 3 torsion bending moments [kNm] (pitching coordinates)

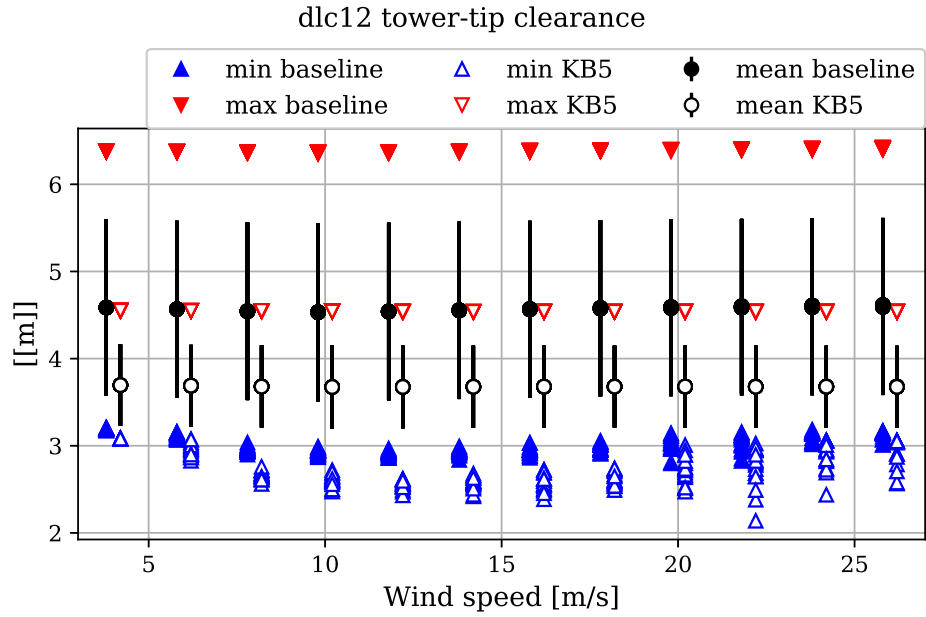


Figure 5.24: Minimum tower to blade tip distance [m] (consider only the minima)

### 5.1.3 DLC24

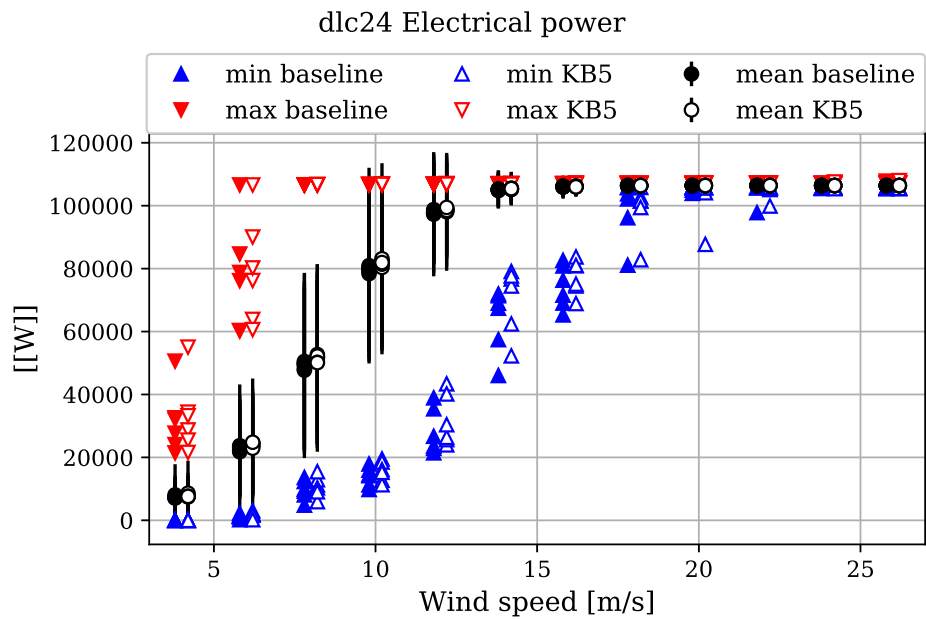


Figure 5.25: Electrical power [W], excluding losses.

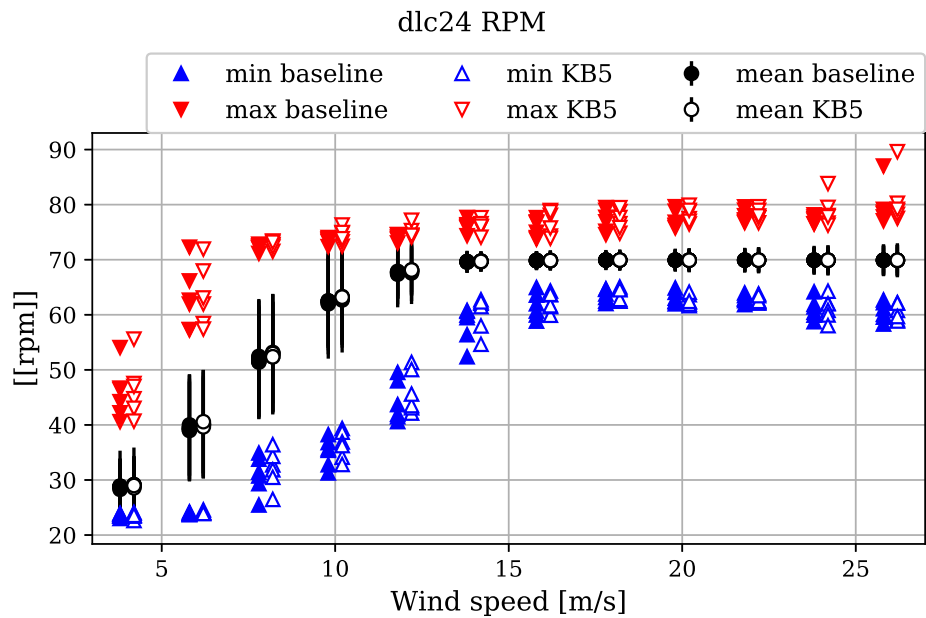


Figure 5.26: Rotor speed [RPM]

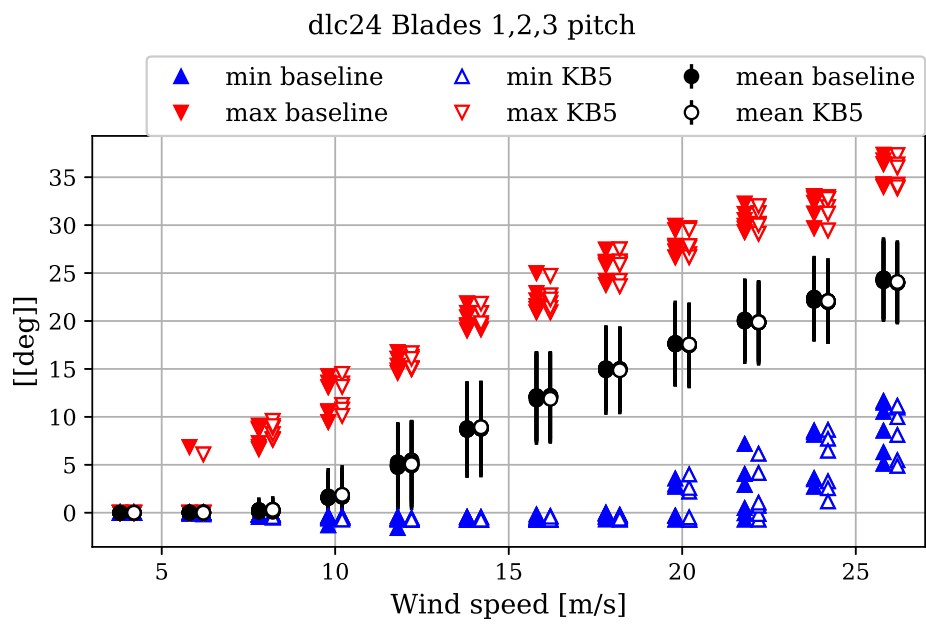


Figure 5.27: Blade 1, 2 and 3 pitch angles [deg]

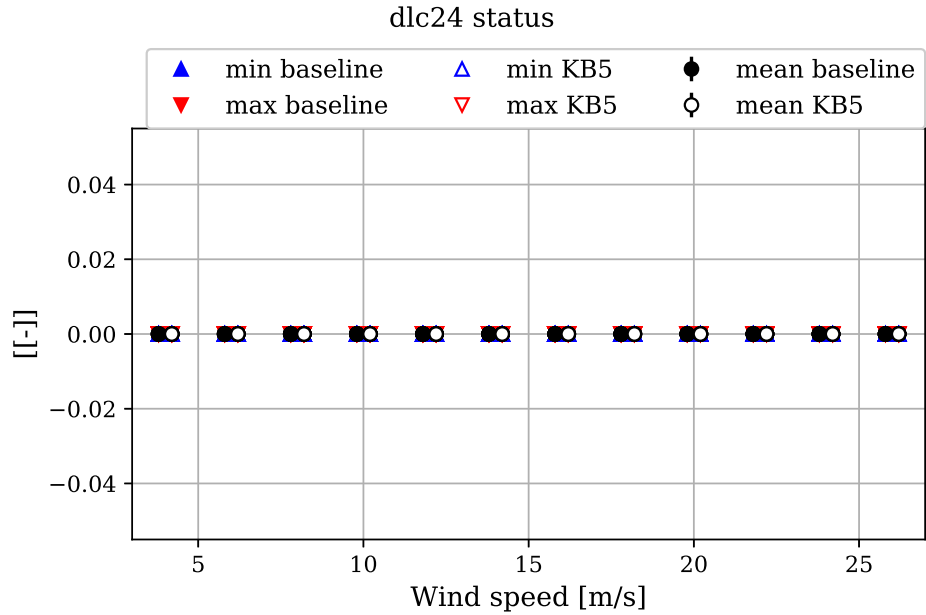


Figure 5.28: Controller status flag [0-6], 0: normal operation, 1: shut down due to overspeed

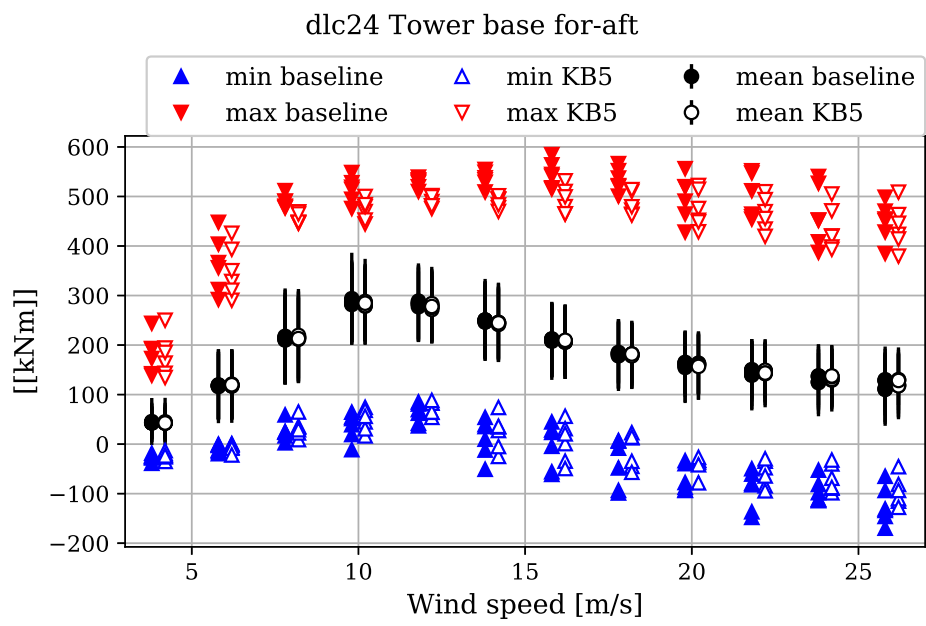


Figure 5.29: Tower base for-aft bending moment [kNm]

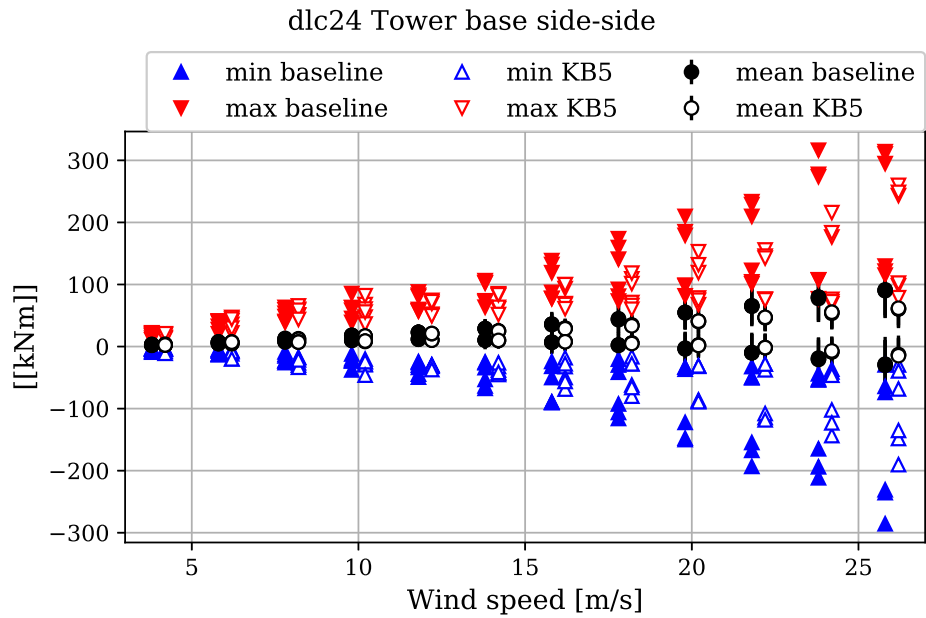


Figure 5.30: Tower base side-side bending moment [kNm]

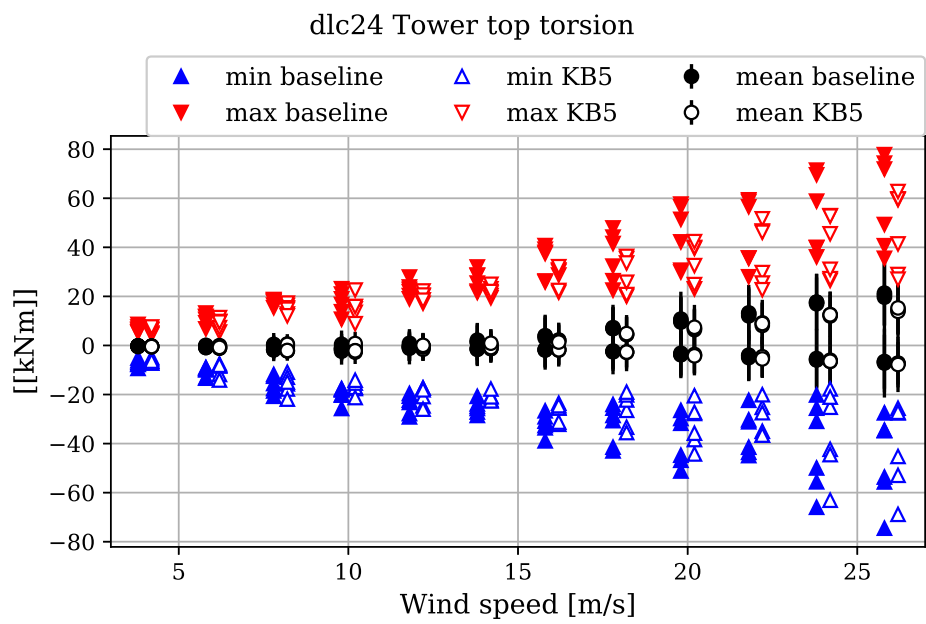


Figure 5.31: Yawing moment tower top [kNm]

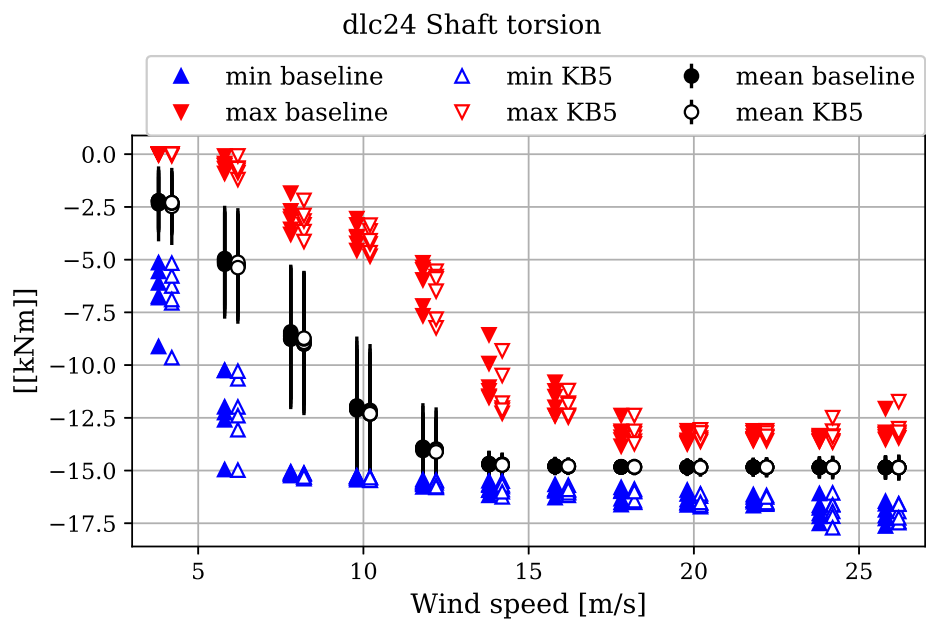


Figure 5.32: Shaft torsion moment [kNm]

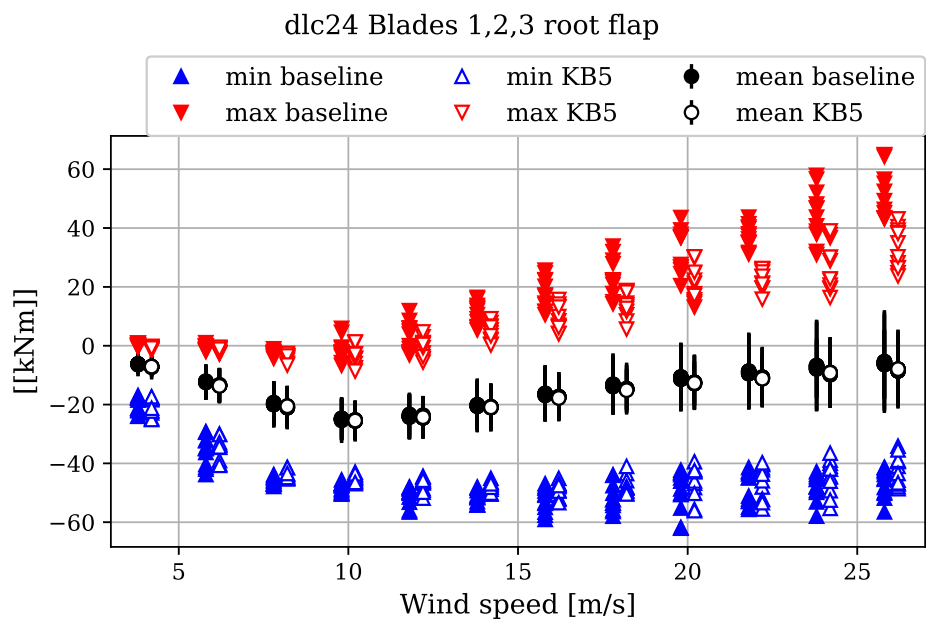


Figure 5.33: Blade root 1, 2 and 3 flap-wise bending moments [kNm] (pitching coordinates)

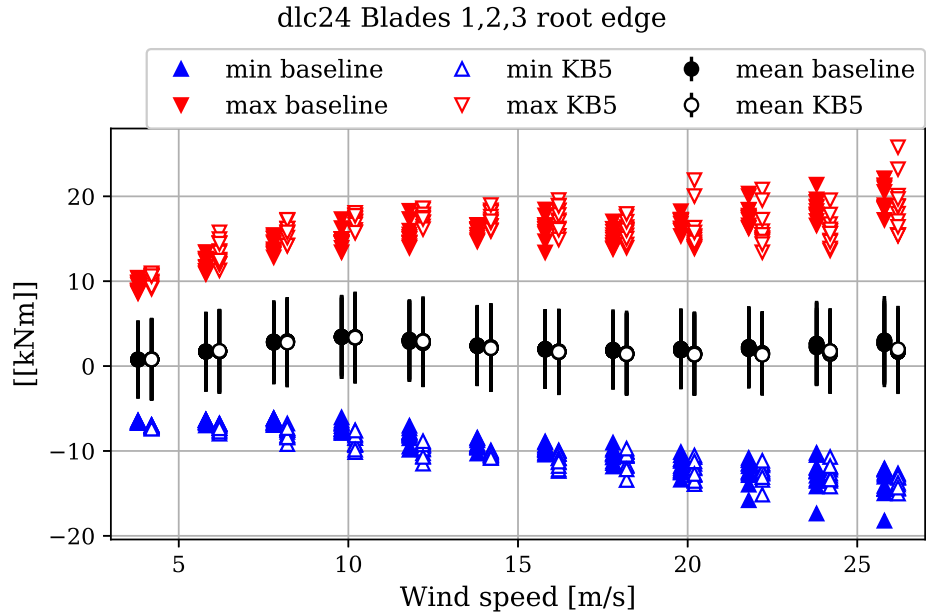


Figure 5.34: Blade root 1, 2 and 3 edge-wise bending moments [kNm] (pitching coordinates)

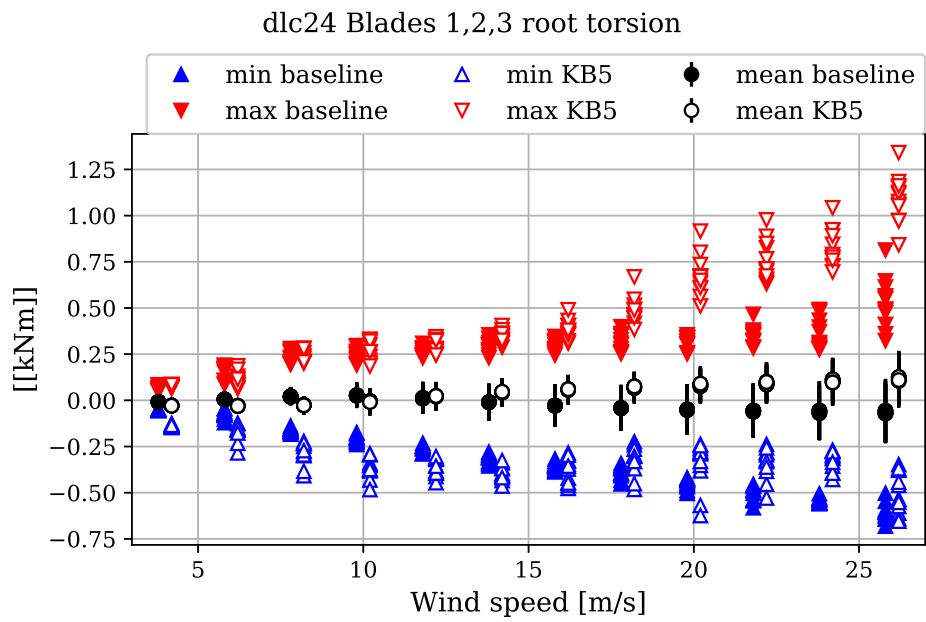


Figure 5.35: Blade root 1, 2 and 3 torsion bending moments [kNm] (pitching coordinates)

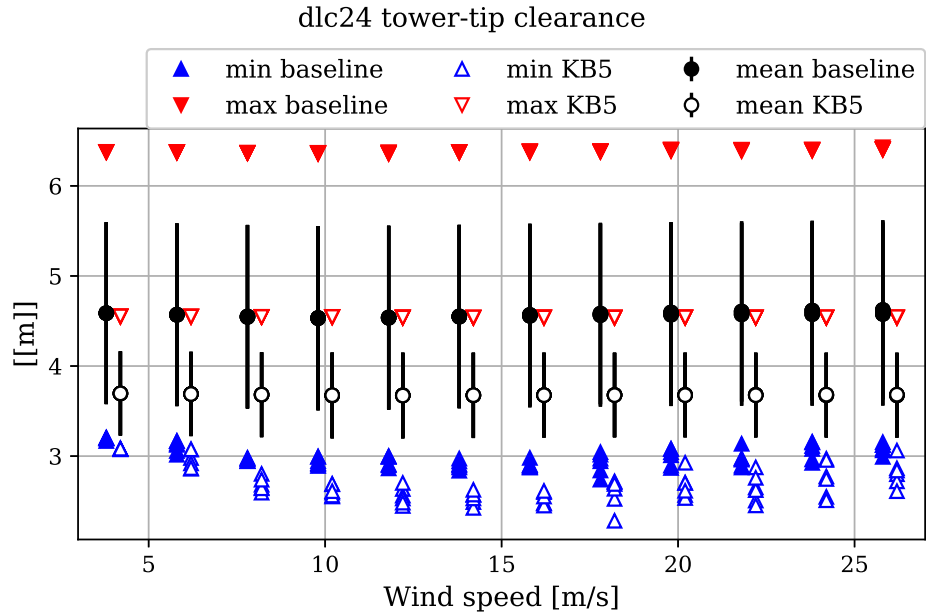


Figure 5.36: Minimum tower to blade tip distance [m] (consider only the minima)

#### 5.1.4 DLC31

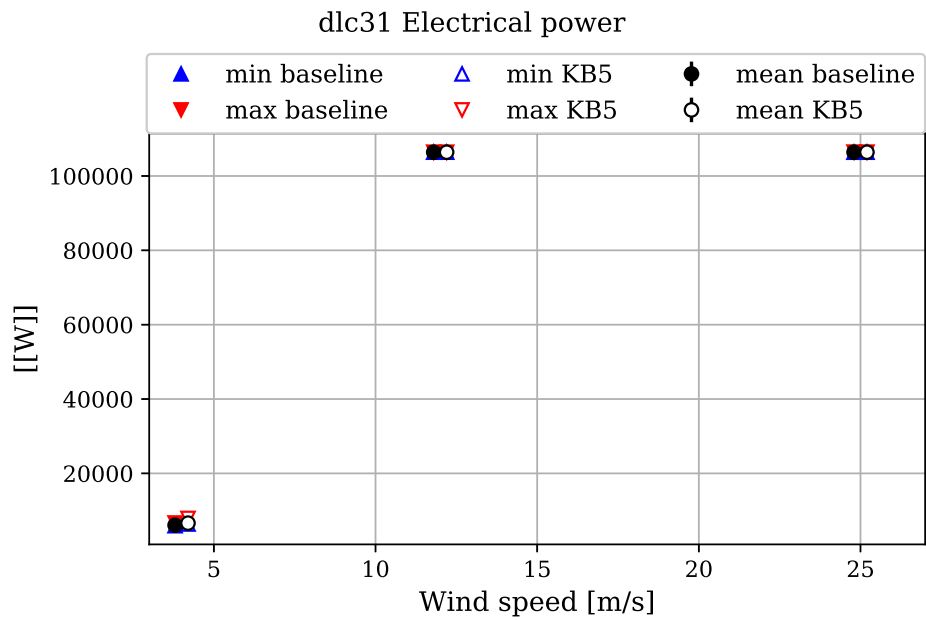


Figure 5.37: Electrical power [W], excluding losses.

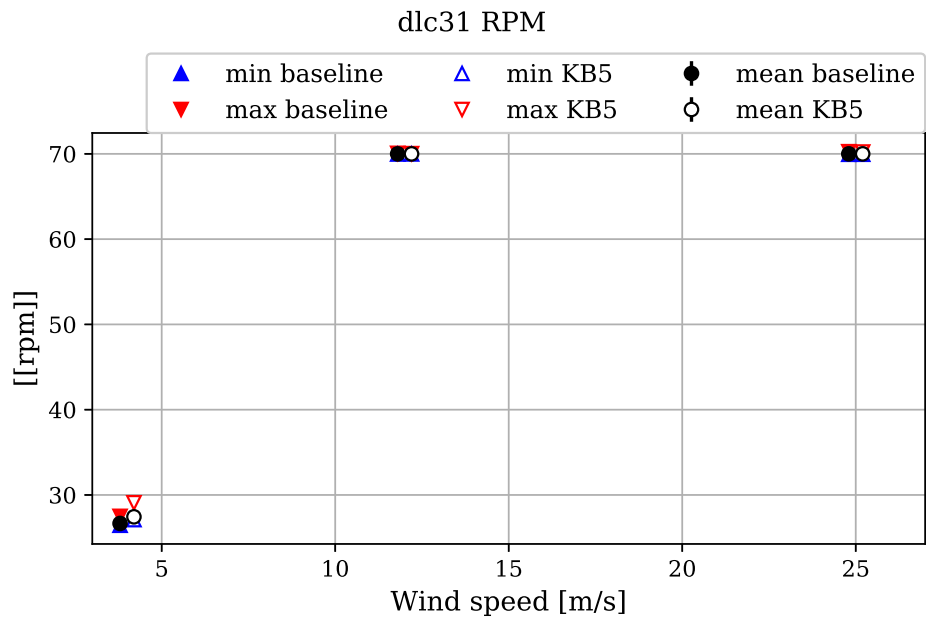


Figure 5.38: Rotor speed [RPM]

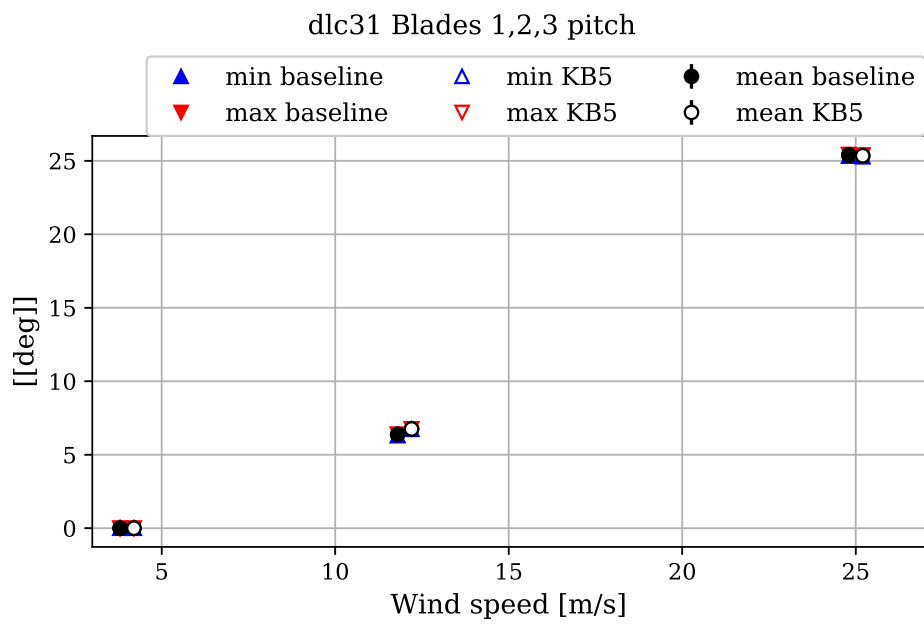


Figure 5.39: Blade 1, 2 and 3 pitch angles [deg]

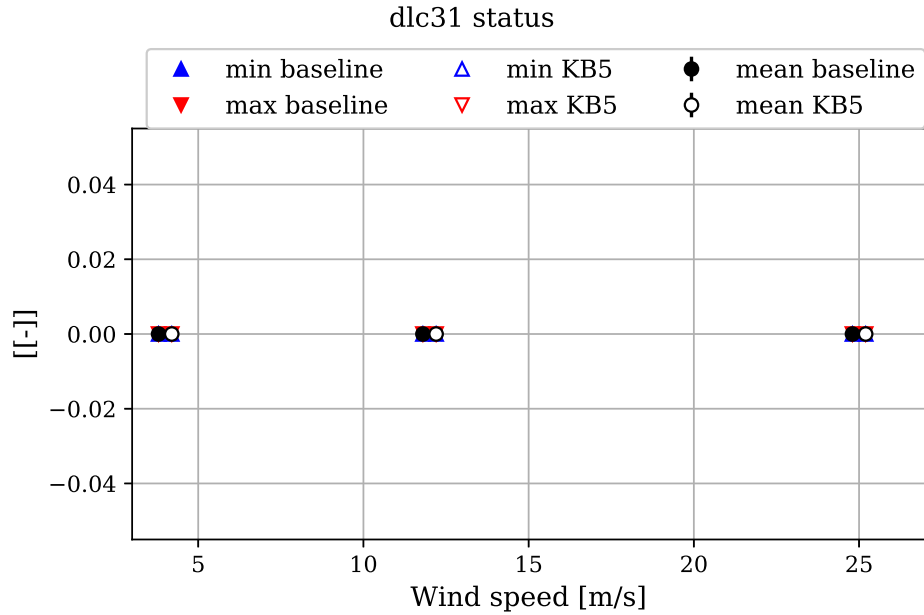


Figure 5.40: Controller status flag [0-6], 0: normal operation, 1: shut down due to overspeed

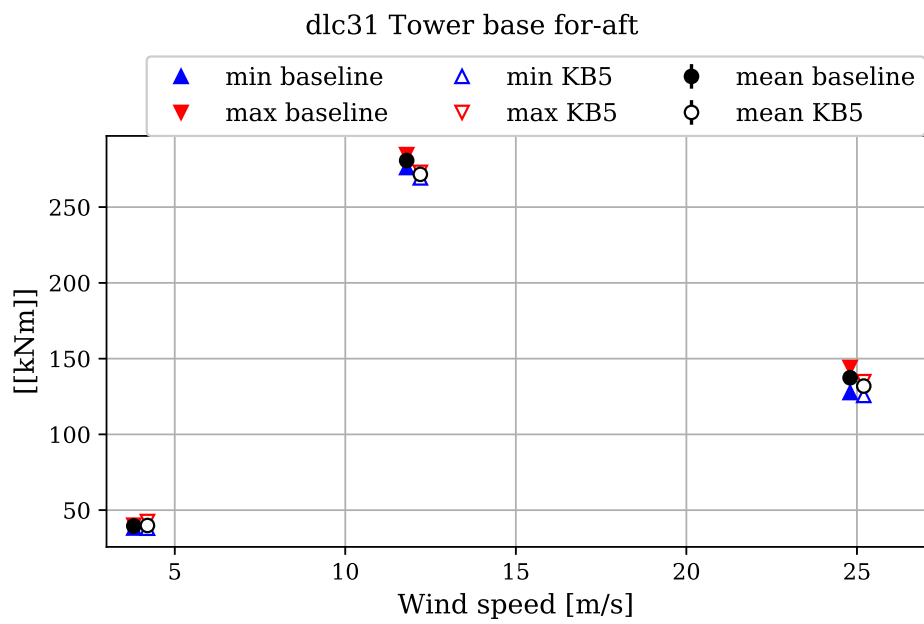


Figure 5.41: Tower base for-aft bending moment [kNm]

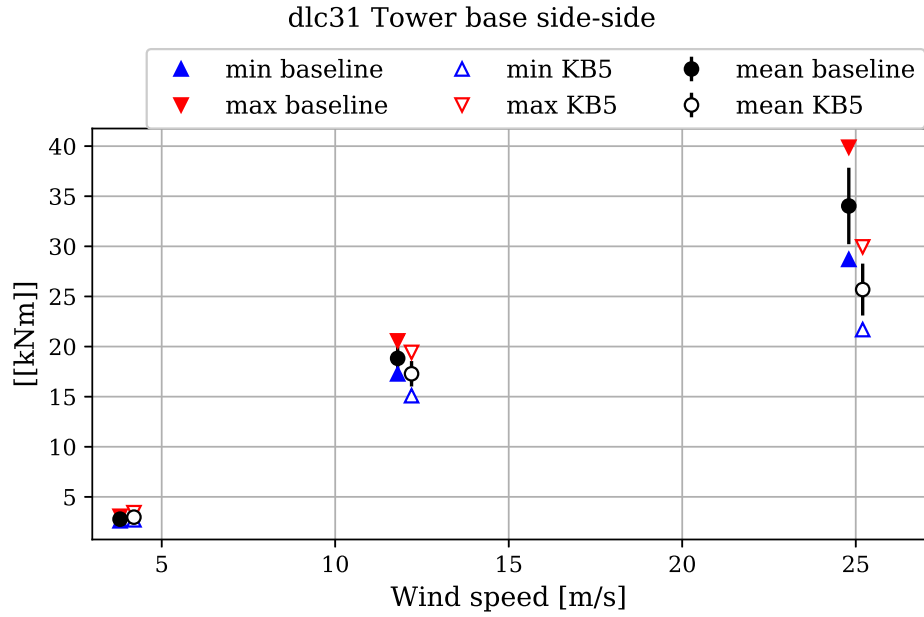


Figure 5.42: Tower base side-side bending moment [kNm]

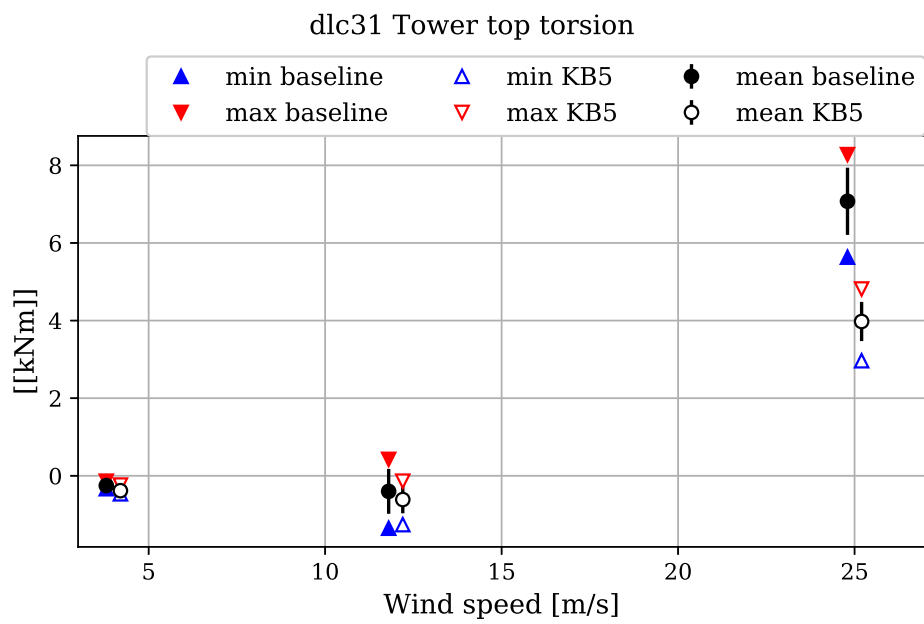


Figure 5.43: Yawing moment tower top [kNm]

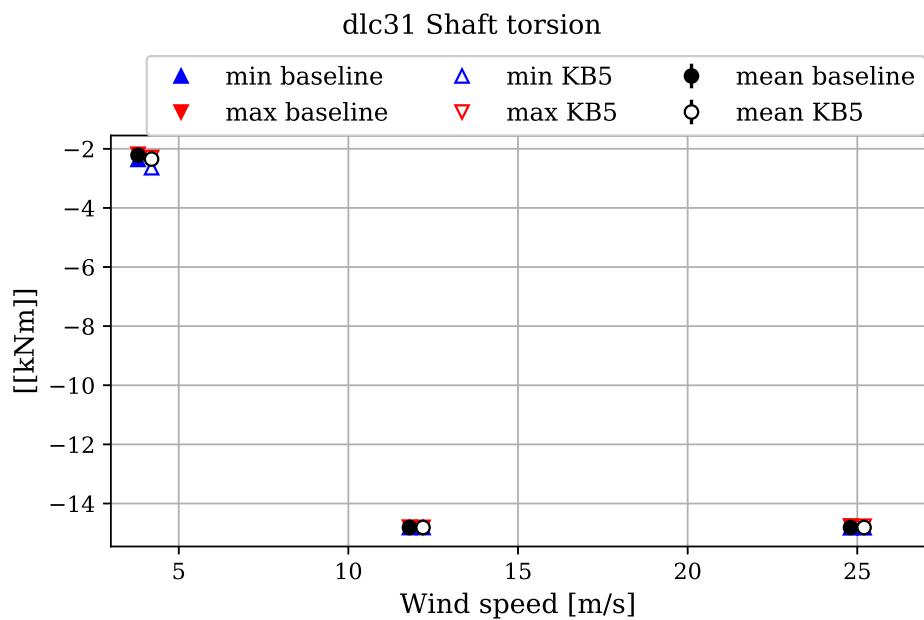


Figure 5.44: Shaft torsion moment [kNm]

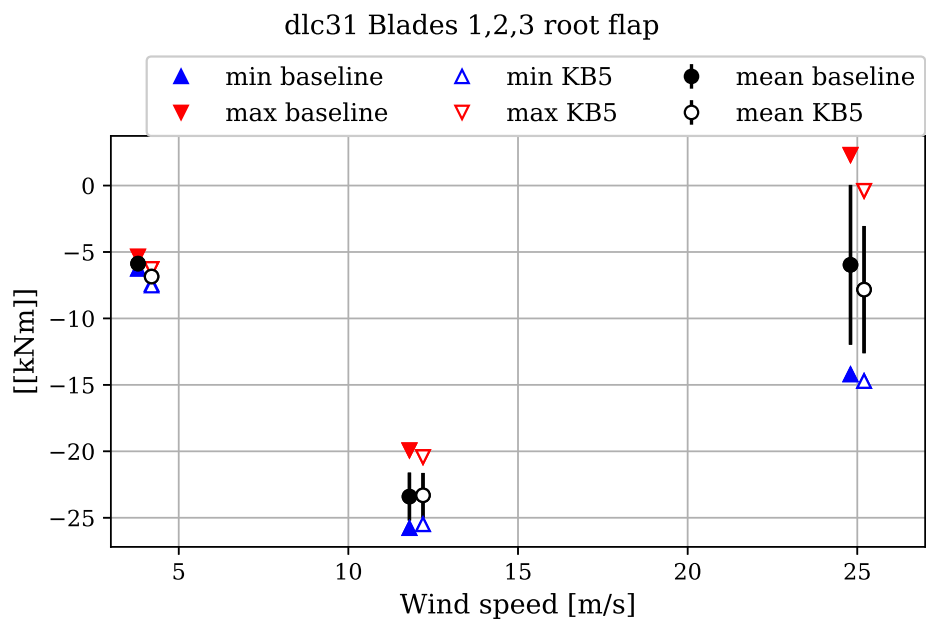


Figure 5.45: Blade root 1, 2 and 3 flap-wise bending moments [kNm] (pitching coordinates)

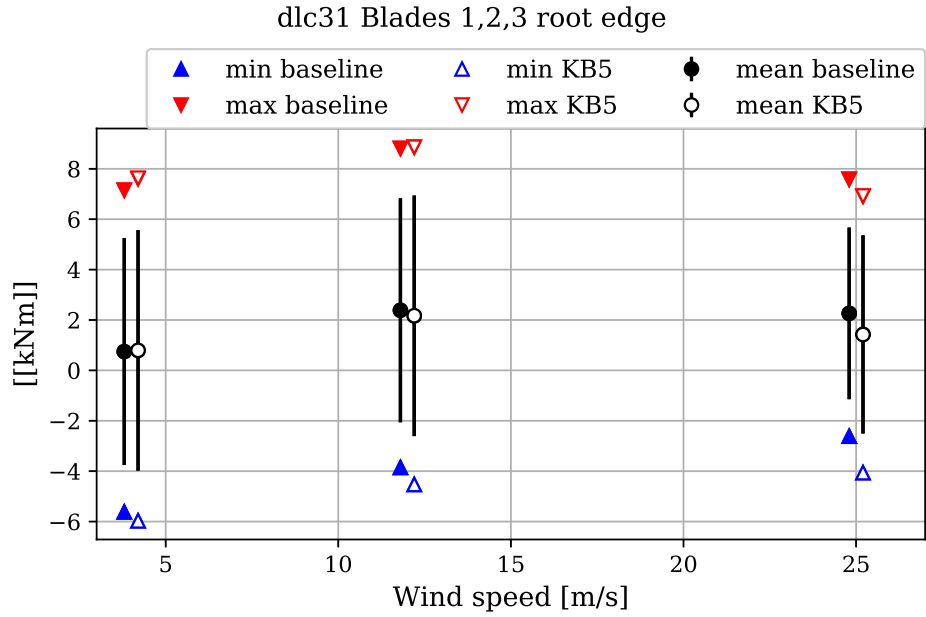


Figure 5.46: Blade root 1, 2 and 3 edge-wise bending moments [kNm] (pitching coordinates)

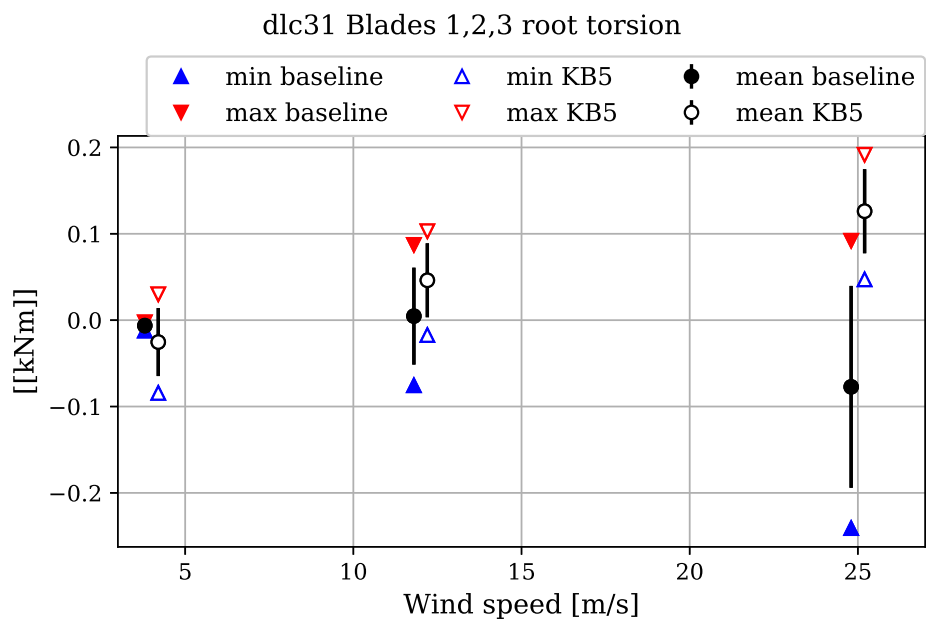


Figure 5.47: Blade root 1, 2 and 3 torsion bending moments [kNm] (pitching coordinates)

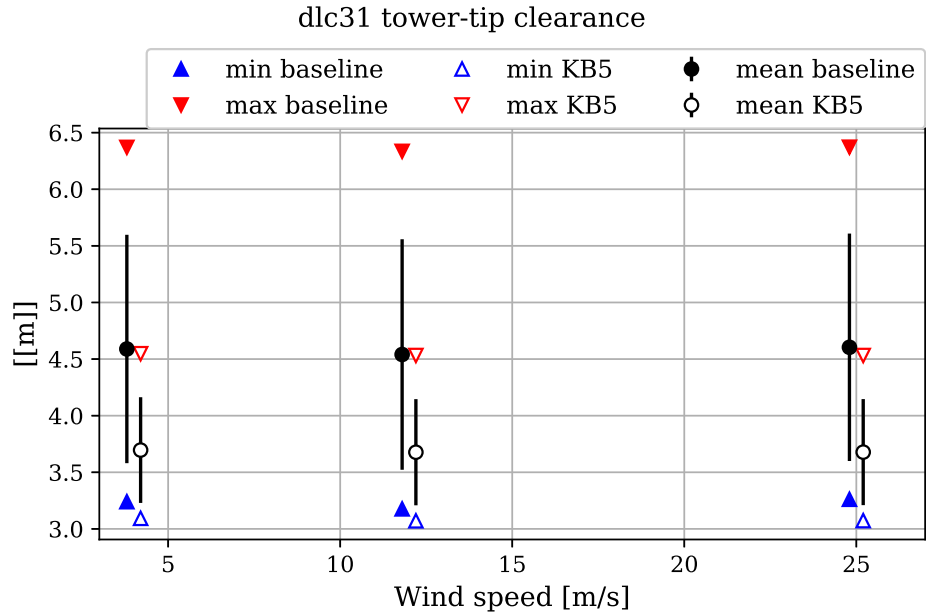


Figure 5.48: Minimum tower to blade tip distance [m] (consider only the minima)

### 5.1.5 DLC41

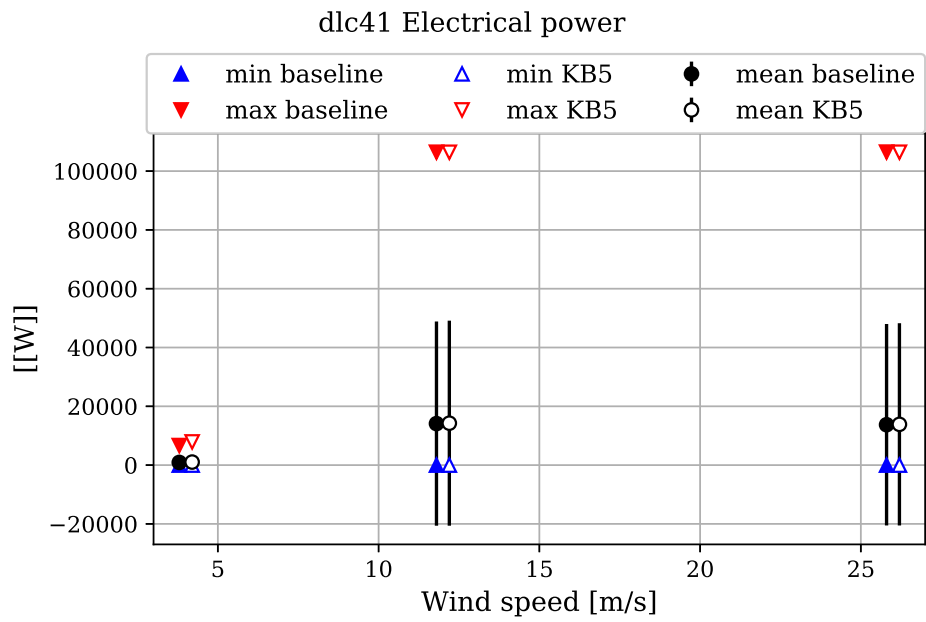


Figure 5.49: Electrical power [W], excluding losses.

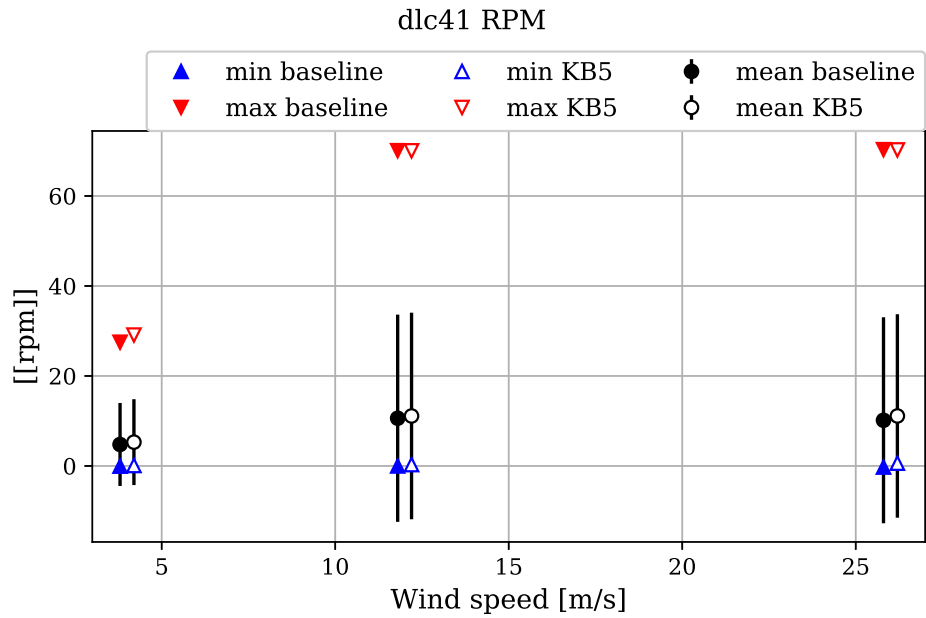


Figure 5.50: Rotor speed [RPM]

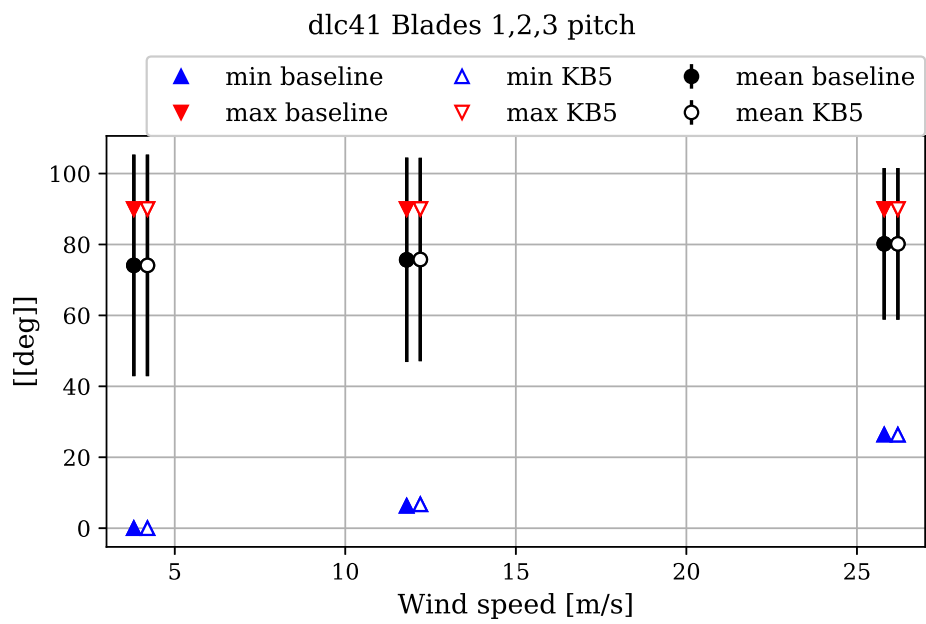


Figure 5.51: Blade 1, 2 and 3 pitch angles [deg]

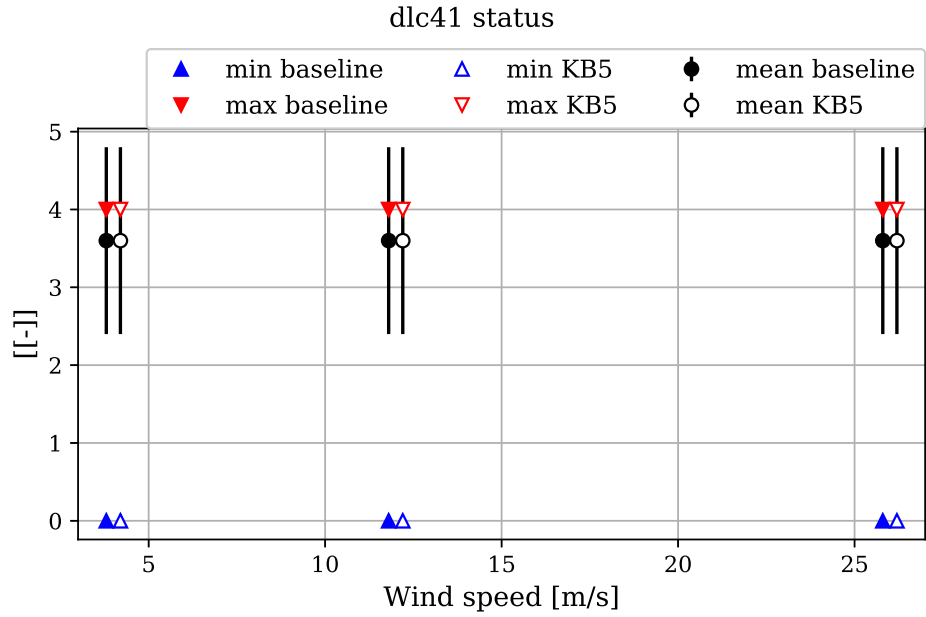


Figure 5.52: Controller status flag [0-6], 0: normal operation, 1: shut down due to overspeed

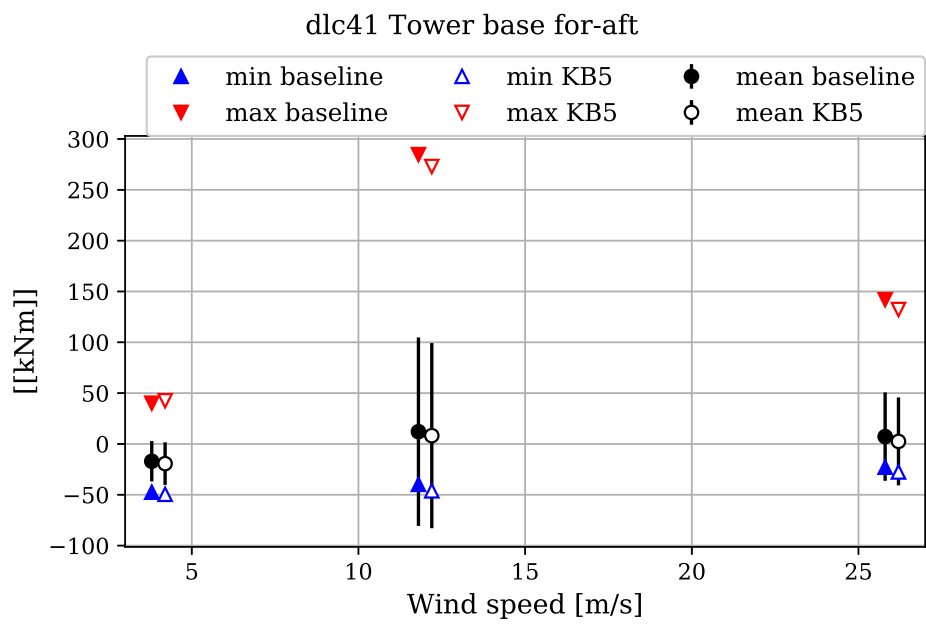


Figure 5.53: Tower base for-aft bending moment [kNm]

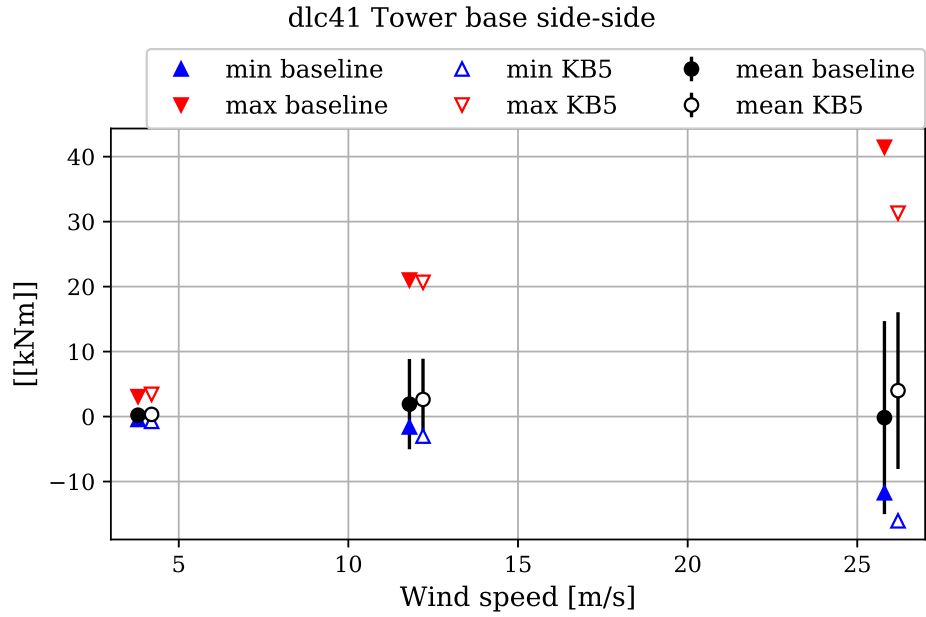


Figure 5.54: Tower base side-side bending moment [kNm]

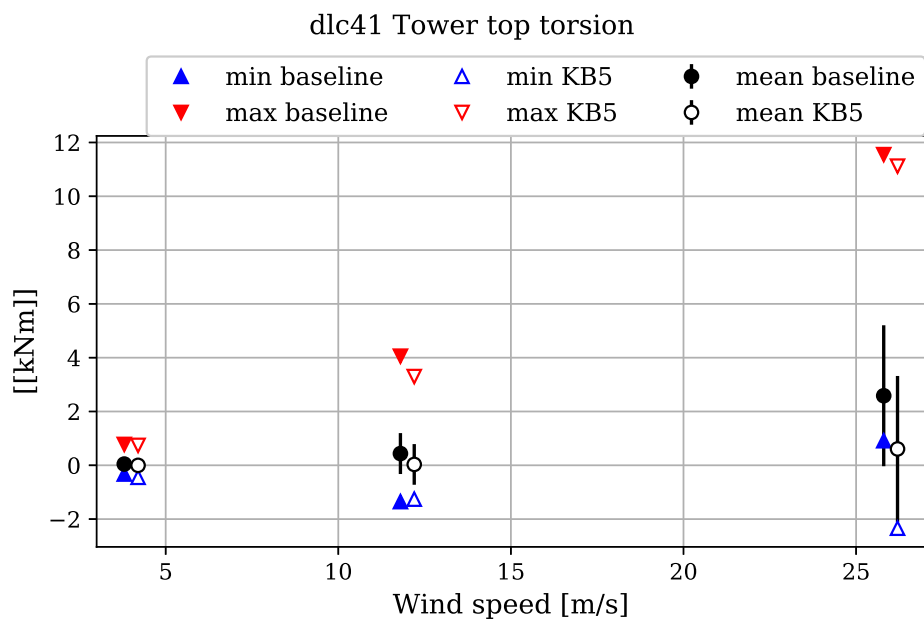


Figure 5.55: Yawing moment tower top [kNm]

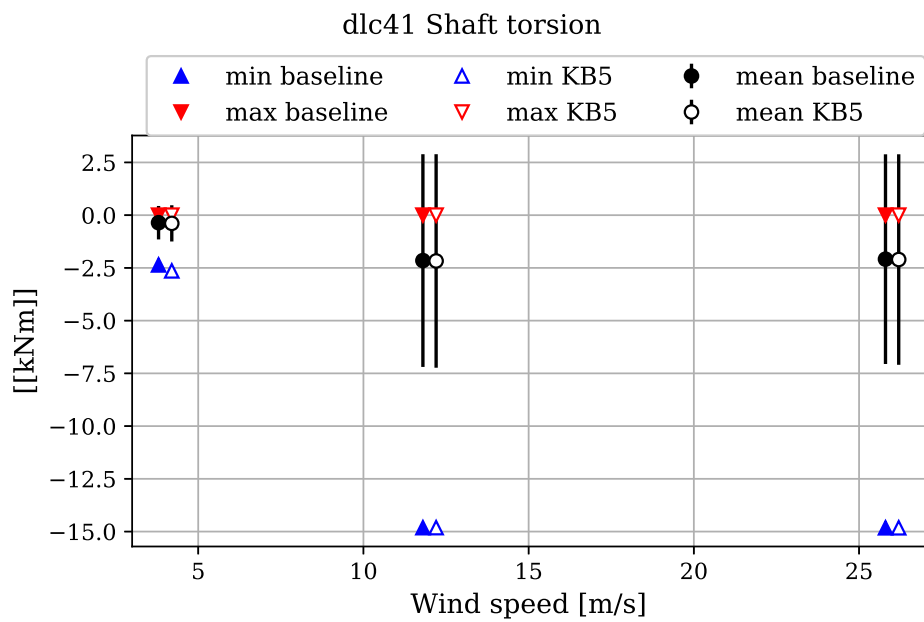


Figure 5.56: Shaft torsion moment [kNm]

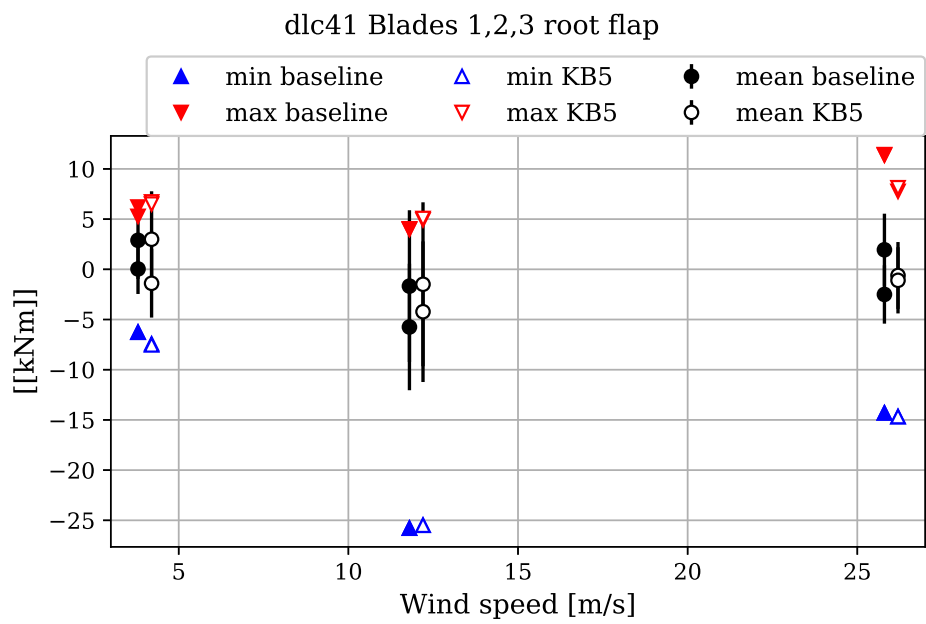


Figure 5.57: Blade root 1, 2 and 3 flap-wise bending moments [kNm] (pitching coordinates)

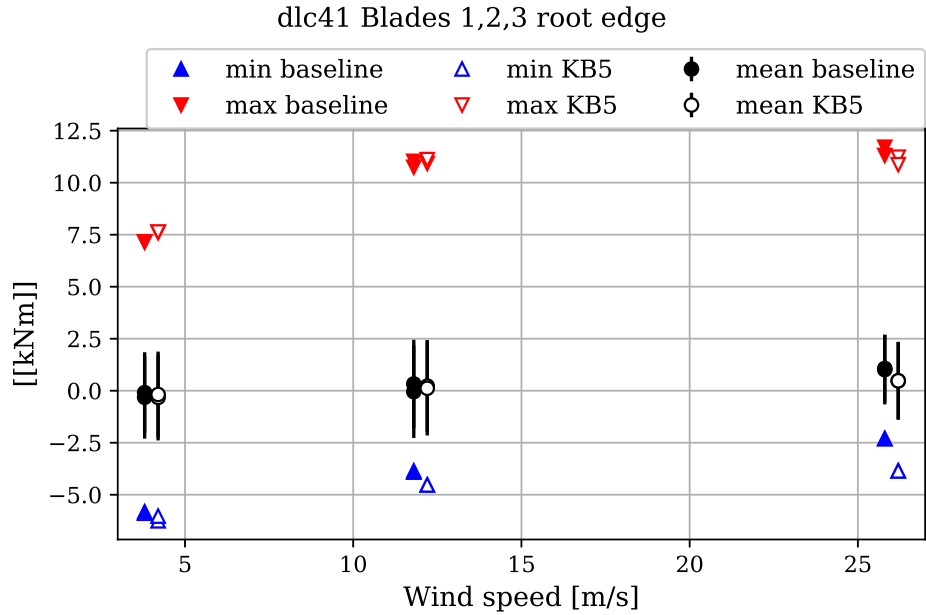


Figure 5.58: Blade root 1, 2 and 3 edge-wise bending moments [kNm] (pitching coordinates)

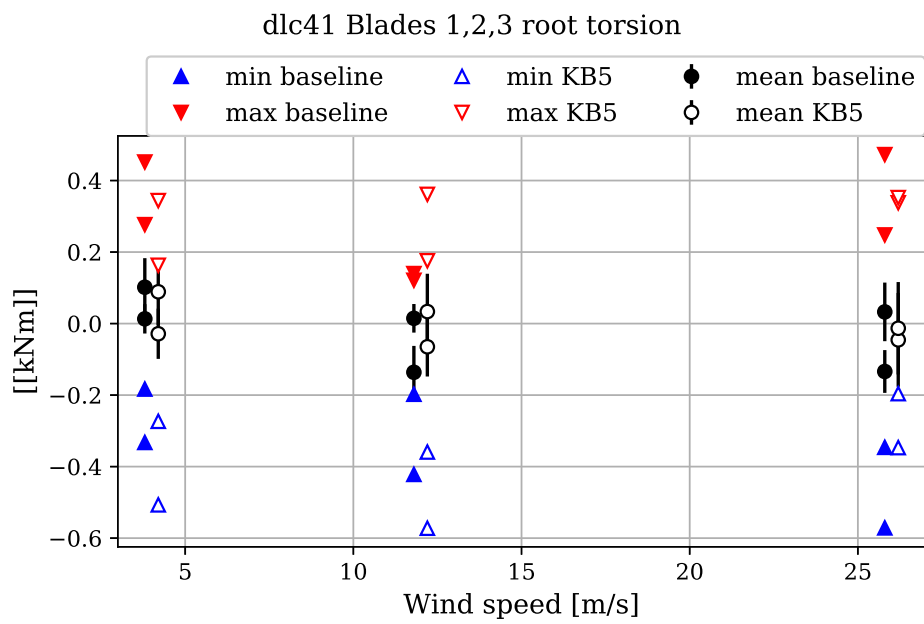


Figure 5.59: Blade root 1, 2 and 3 torsion bending moments [kNm] (pitching coordinates)

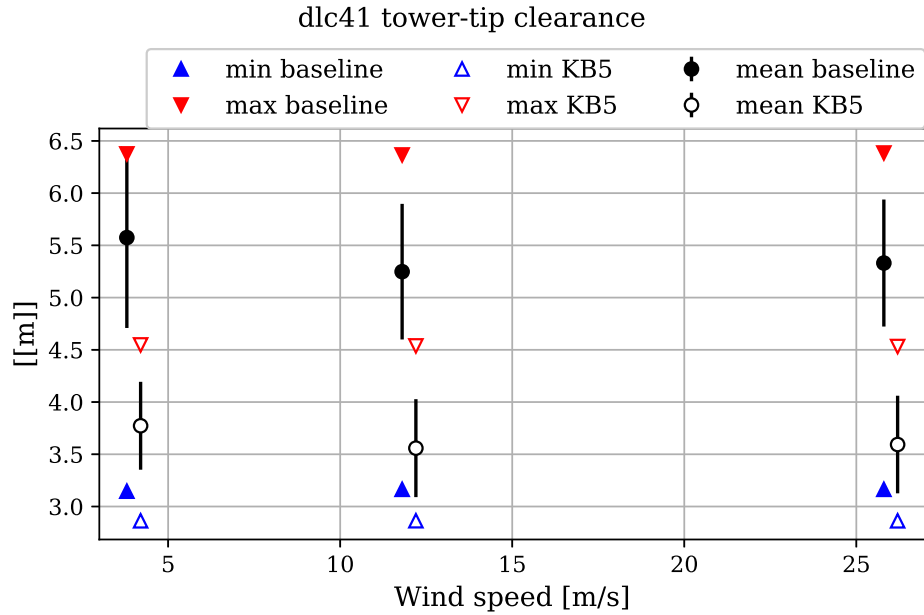


Figure 5.60: Minimum tower to blade tip distance [m] (consider only the minima)

### 5.1.6 DLC64

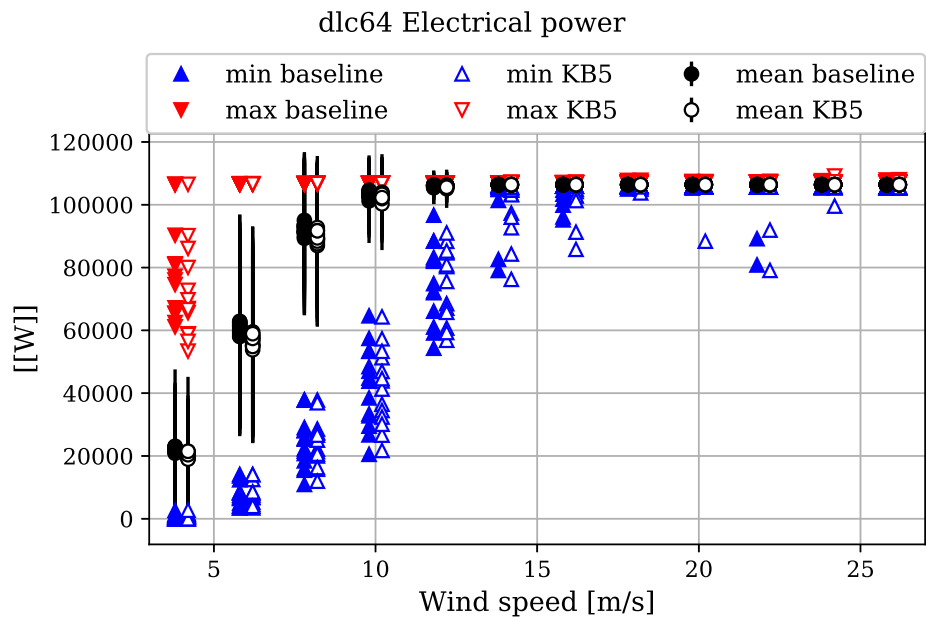


Figure 5.61: Electrical power [W], excluding losses.

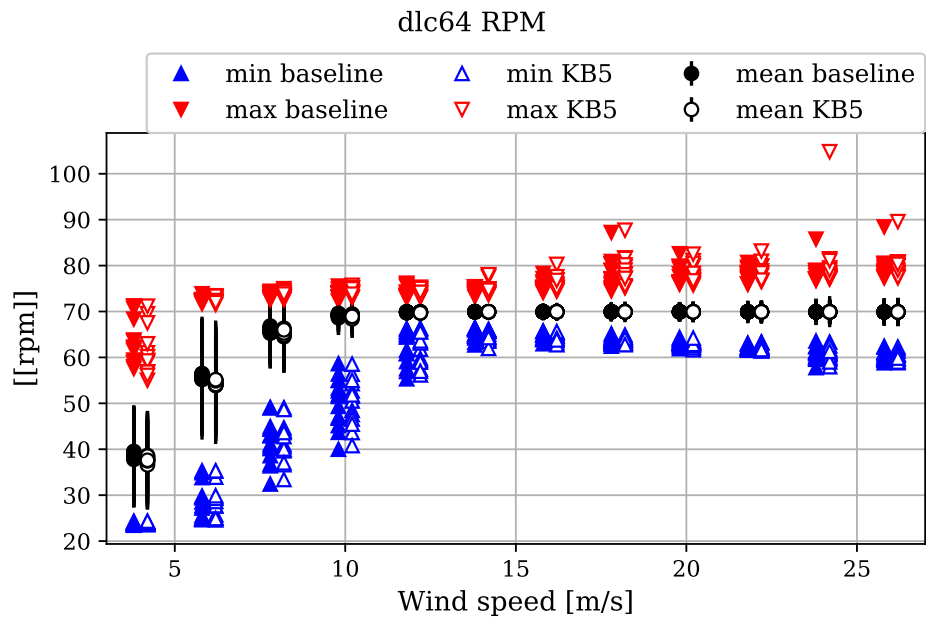


Figure 5.62: Rotor speed [RPM]

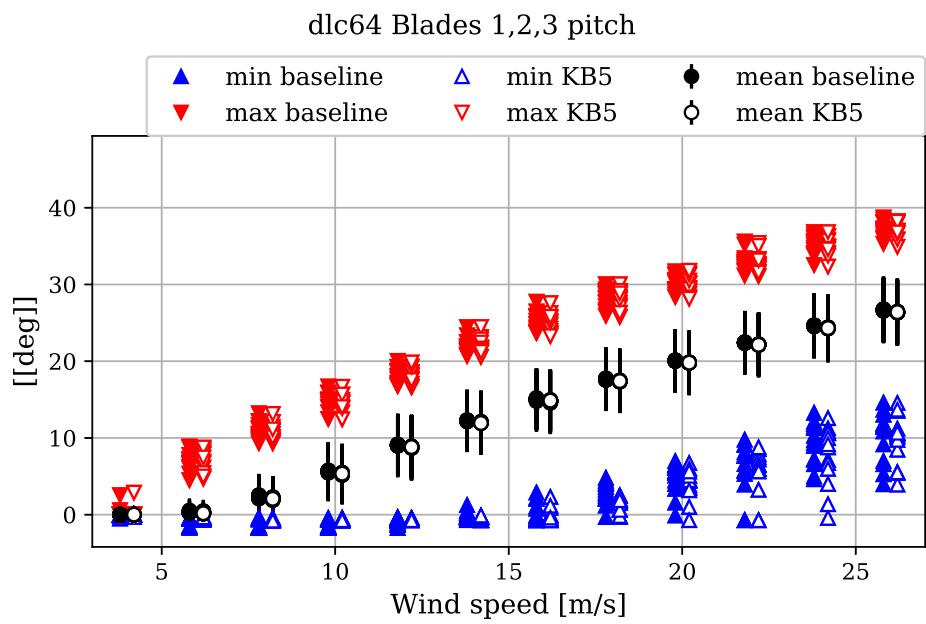


Figure 5.63: Blade 1, 2 and 3 pitch angles [deg]

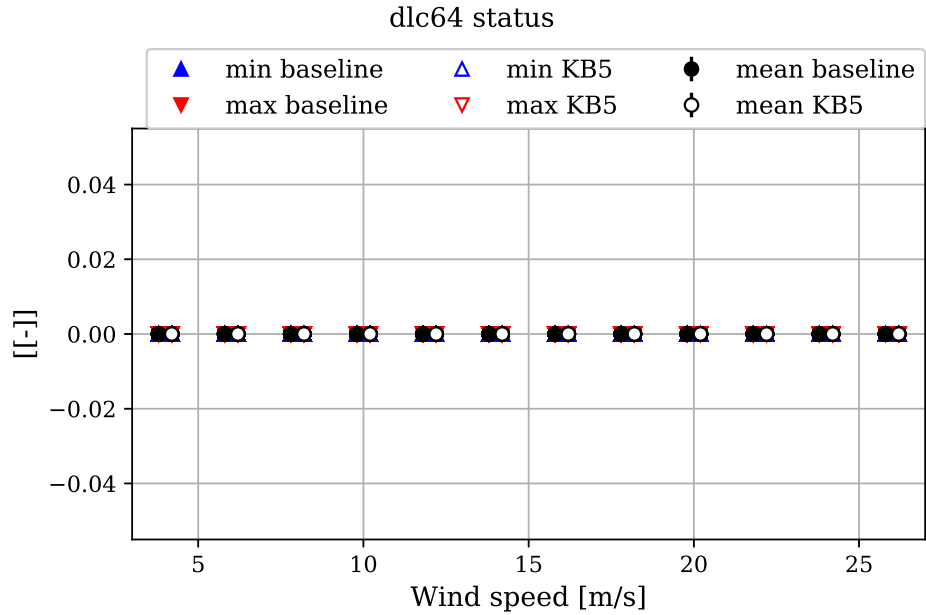


Figure 5.64: Controller status flag [0-6], 0: normal operation, 1: shut down due to overspeed

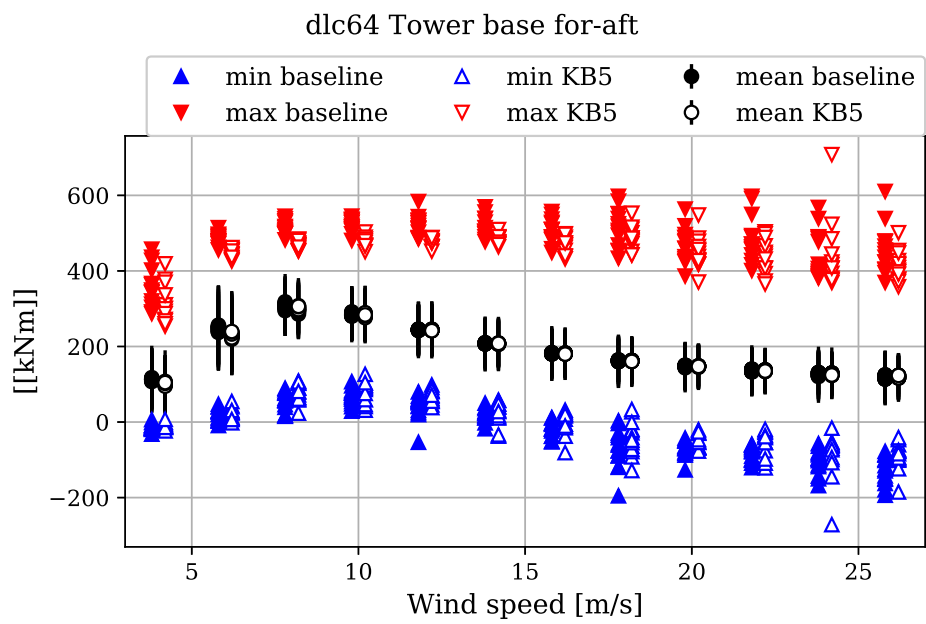


Figure 5.65: Tower base for-aft bending moment [kNm]

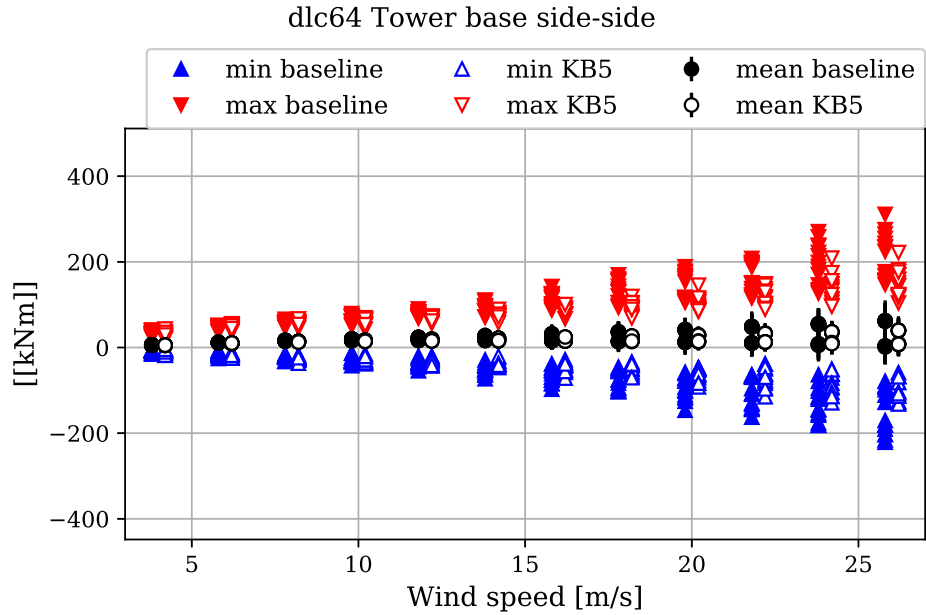


Figure 5.66: Tower base side-side bending moment [kNm]

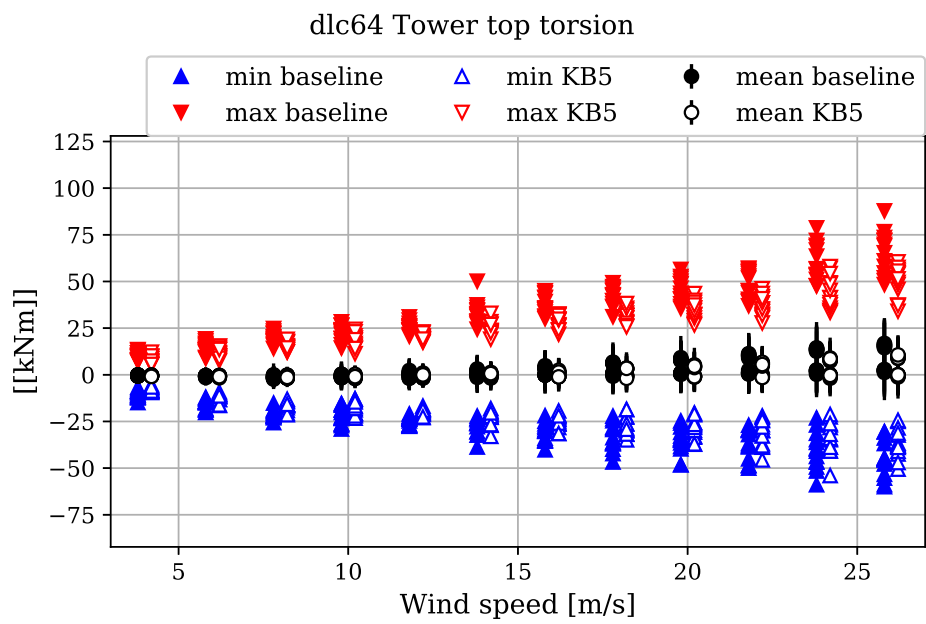


Figure 5.67: Yawing moment tower top [kNm]

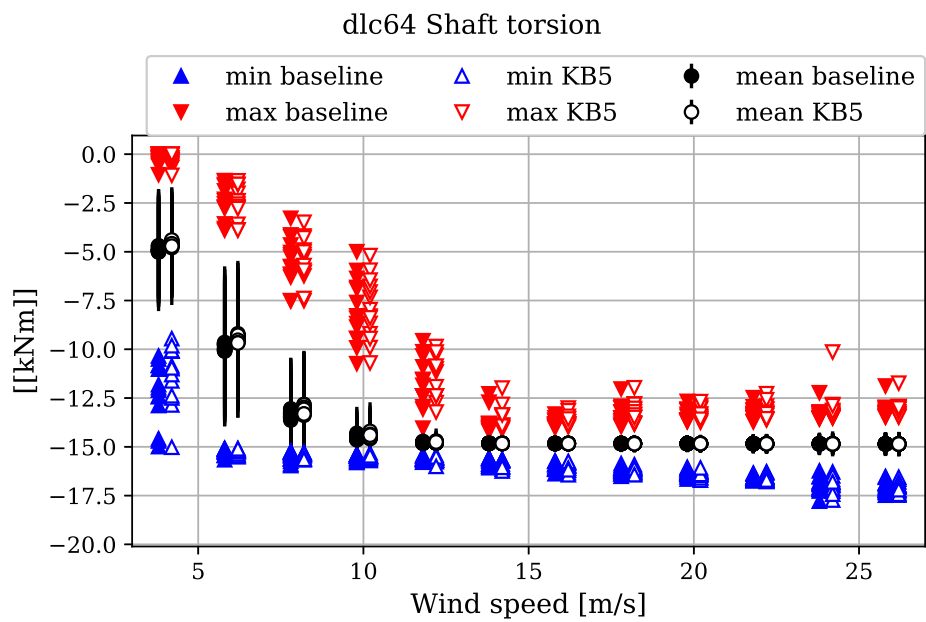


Figure 5.68: Shaft torsion moment [kNm]

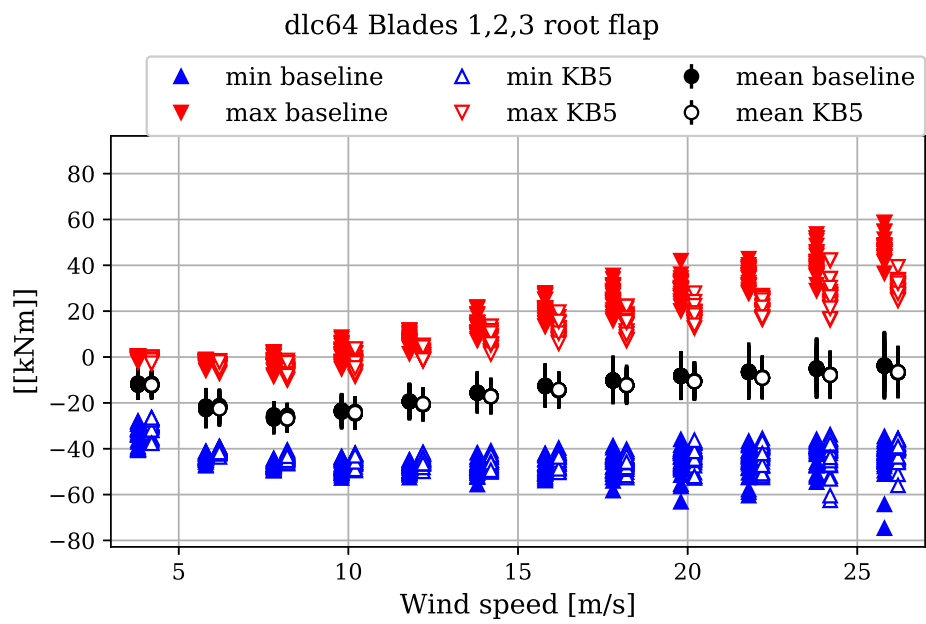


Figure 5.69: Blade root 1, 2 and 3 flap-wise bending moments [kNm] (pitching coordinates)

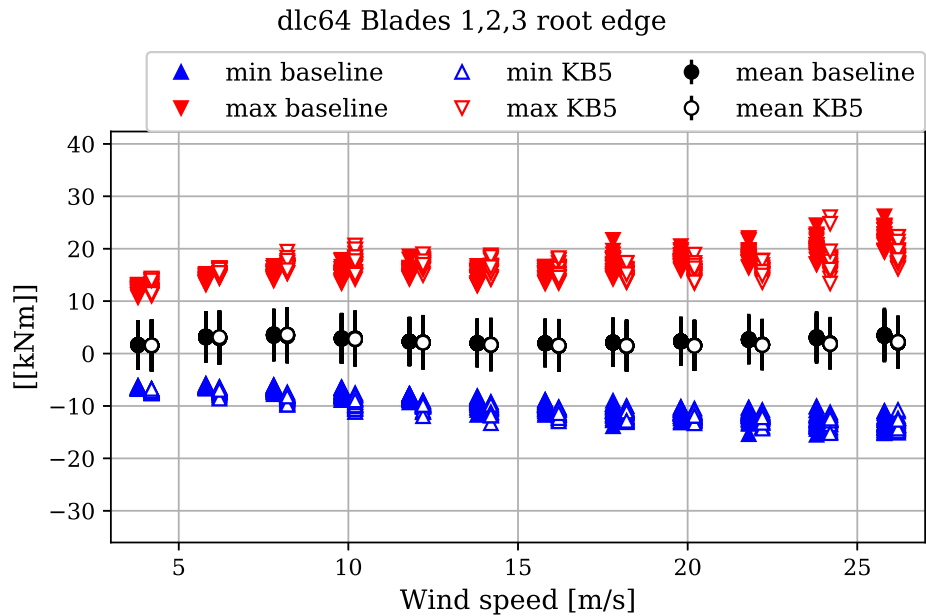


Figure 5.70: Blade root 1, 2 and 3 edge-wise bending moments [kNm] (pitching coordinates)

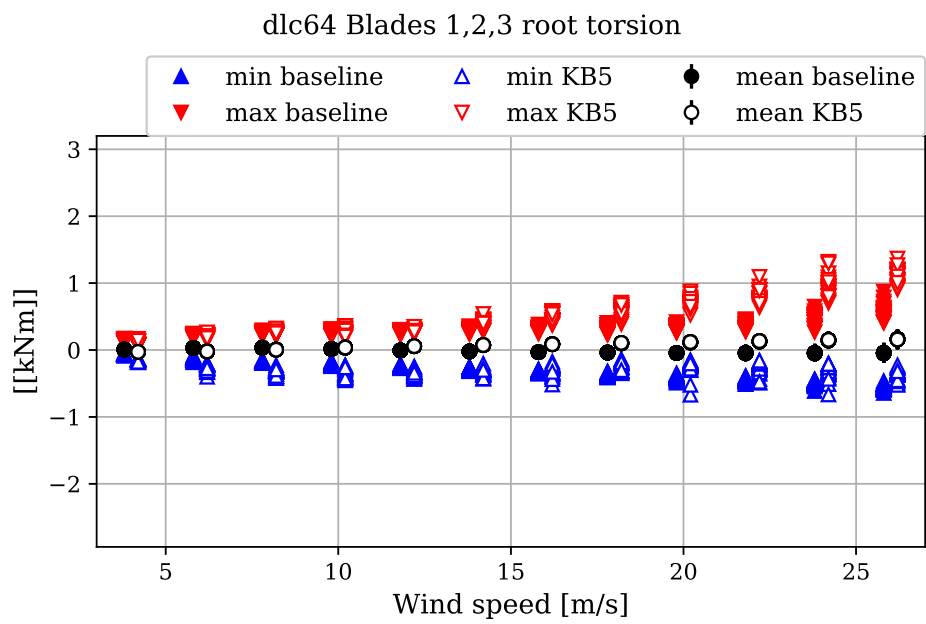


Figure 5.71: Blade root 1, 2 and 3 torsion bending moments [kNm] (pitching coordinates)

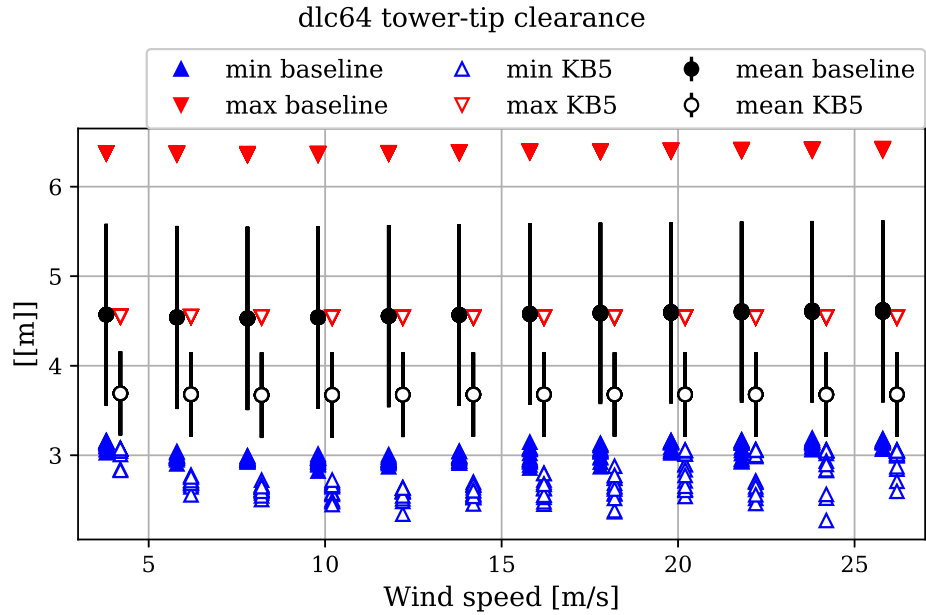


Figure 5.72: Minimum tower to blade tip distance [m] (consider only the minima)